

**FUNCTIONALIZED CVD GROWN
GRAPHENE FOR GAS SENSING
APPLICATIONS**

**A Thesis Submitted to
the Graduate School of Engineering and Sciences of
İzmir Institute of Technology
in Partial Fulfillment of the Requirements for the Degree of**

DOCTOR OF PHILOSOPHY

in Material Science and Engineering

**by
Nesli YAĞMURCUKARDEŞ**

**July 2017
İZMİR**

We approve the thesis of Nesli YAĞMURCUKARDEŞ

Examining Committee Members:

Assoc. Prof. Dr. Cem ÇELEBİ

Department of Physics, İzmir Institute of Technology

Assoc. Prof. Dr. Ekrem ÖZDEMİR

Department of Chemical Engineering, İzmir Institute of Technology

Assist. Prof. Dr. Gökhan UTLU

Department of Physics, Ege University

Prof. Dr. Canan VARLIKLI

Department of Photonics, İzmir Institute of Technology

Assist. Prof. Dr. Serkan BÜYÜKKÖSE

Department of Physics, Gebze Technical University

20 July 2017

Assoc. Prof. Dr. Cem ÇELEBİ

Supervisor, Department of Physics
İzmir Institute of Technology

Assist. Prof. Dr. Özhan ÜNVERDİ

Co-Supervisor, Department of
Electrical and Electronics Engineering
Yaşar University

Prof. Dr. Mustafa M. DEMİR

Head of the Department of
Material Science and Engineering

Prof. Dr. Aysun SOFUOĞLU

Dean of the Graduate School of
Engineering and Sciences

ACKNOWLEDGMENTS

First of all, I would like to express my deeply thanks to my adviser Assoc. Prof. Dr. Cem Çelebi for his intensive guidance, patient instruction, generous help and support in my studies and this thesis work.

I thankfully commemorate my former adviser Assoc. Prof. Dr. Yusuf Selamet for his great contributions and unique assistance.

I would also like to thank my lab mate Hasan Aydın, my best friends Atike İnce Yardımcı and Duygu Özaydın for their unique friendship and special motivation at difficult times.

In addition, I would like to thank my committee members Assoc. Prof. Dr. Ekrem Özdemir and Assist. Prof. Dr. Gökhan Utlu for their contributions during my whole Ph.D. studies.

Most importantly, none of this would have been possible without the love and patience of my family. I would like to express my heart-felt gratitude to my parents Nesil Tekgüzel and Memiş Tekgüzel, my husband Mehmet Yağmurcukardeş for everything they have done for me.

Finally, I would like to take the opportunity to thank all persons in IYTE who have ever helped me before.

This research was supported by TUBITAK with 112T946 project number.

ABSTRACT

FUNCTIONALIZED CVD GROWN GRAPHENE FOR GAS SENSING APPLICATIONS

Graphene is a two dimensional one-atom thick sheet of sp^2 bonded carbon atoms arranged in a honeycomb lattice structure. It has high electron mobility and it is the material with the lowest resistivity at room temperature. By changing the edge properties with chemical modification, few-layer graphene may gain new magnetic properties. Besides having unusual electronic properties, single-layer graphene has important gas sensing capability. With the adsorption of the gas molecules, the local carrier concentration of graphene is modified and its resistance is altered. The high mobility, large area ohmic contact and metallic conductivity of graphene help to reduce the background noise and thus make it highly sensitive device even small molecular changes at atomic ranges.

In this dissertation, Chemical Vapor Deposition (CVD) grown graphene layers were functionalized by self-assembled monolayers (SAMs) and etched anisotropically by H_2 for the first time to improve sensor characteristics for toxic gas sensing. CO , CO_2 , NH_3 gases were used as target molecules. Characterization techniques such as Optical Microscopy, Scanning Electron Microscopy (SEM), Atomic Force Microscopy (AFM), Kelvin Probe Force Microscopy (KPFM), Raman Spectroscopy, Quartz Crystal Microbalance (QCM) and amperometric measurements were used for the investigation of the metal thin film, graphene layers and gas adsorbed film structures.

Results indicate that the SAM modification enhanced CO and NH_3 absorbing capability of graphene films and also improved their periodic reversible response characteristics. The resistivity results are consistent with frequency change results. Humidity sensitivity of sensors are also decreased significantly due to the applied etching process.

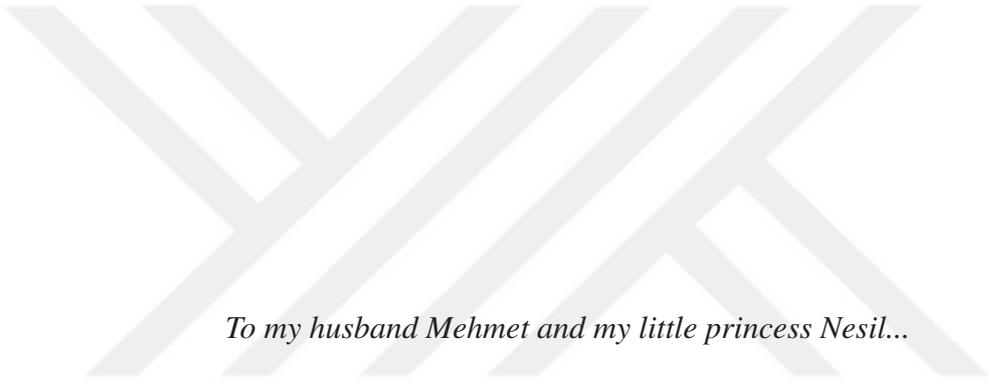
ÖZET

KBB YÖNTEMİ İLE BÜYÜTÜLEN FONKSİYONELLEŞTİRİLMİŞ GRAFENİN GAZ ALGILAMA UYGULAMALARI

Grafen, bir atom kalınlığında sp^2 bağı karbon atomlarının petek yapı örgüsünde dizildiği iki boyutlu bir malzemedir. Eşsiz mekanik mukavemete sahip, sıfır boşluklu bir yarı iletkenidir. Yüksek elektron mobilitesine ve oda sıcaklığında en düşük özdirençe sahip malzemedir. Kenar özelliklerini kimyasal modifikasyon ile değiştirerek az tabakalı grafene yeni manyetik özellikler kazandırılabilir. Olağandışı elektronik özelliklere sahip olmasının yanı sıra, tek katmanlı grafen önemli gaz algılama kabiliyetine sahiptir. Gaz moleküllerinin adsorpsiyonu ile yerel taşıyıcı konsantrasyonu modifiye edilir ve direnci değişir. Grafenin yüksek elektron hareket kabiliyeti, geniş alan omik teması ve metal iletkenliği, arka plandaki gürültüyü azaltmaya yardımcı olur ve böylece milyarda bir seviyedeki parçaları ve hatta atomik aralıktaki küçük moleküler değişiklikleri tespit etmek için son derece hassas bir cihaz yapar.

Bu tezde, Kimyasal Buhar Briktirme (KBB) yöntemi ile büyütülen grafen filmler, sensör özelliklerinin zehirli gazların algılanmasında iyileştirilmesi adına ilk defa kendiliğinden organize tek katmanlarla fonksiyonelleştirildi ve anizotropik H_2 aşındırma yöntemleri uygulandı. Karakterizasyon teknikleri; Optik Mikroskop, Taramalı Elektron Mikroskobu (SEM), Atomik Kuvvet Mikroskobu (AFM), Kelvin Uç Kuvvet Mikroskobu (KPFM), Raman Spektroskopisi, Kuvars Kristal Mikroterazi (QCM) ve amperometrik ölçüm teknikleri, metal ince filmlerin, grafen katmanlarının ve gaz emilen film yapılarının araştırılmasında kullanılmıştır.

Sonuçların gösterdiğine göre grafen filmlerin KBB modifikasyonu ile CO ve NH_3 emilim kapasitesi artırılmış ve periyodik tersinir tepki özellikleri iyileştirilmiştir. Direnç ölçümleri frekans değişim sonuçları ile uyumludur. Uygulanan aşındırma işlemi ile sensörlerin neme hassasiyetleri de önemli ölçüde azaltılmıştır.



To my husband Mehmet and my little princess Nesil...

TABLE OF CONTENTS

LIST OF FIGURES	ix
LIST OF TABLES	xix
LIST OF SYMBOLS	xx
CHAPTER 1. INTRODUCTION	1
CHAPTER 2. LITERATURE REVIEW	3
2.1. History of Graphene.....	3
2.2. Crystal Structure of Graphene	3
2.3. Electronic Properties	4
2.4. Vibrational Properties	6
2.5. Optical Properties	9
2.6. Graphene Production Methods	9
2.6.1. Mechanical Exfoliation	10
2.6.2. Thermal Decomposition of SiC	11
2.6.3. Unzipping CNTs	13
2.6.4. Chemical Vapor Deposition (CVD)	13
2.7. Graphene Characterization Techniques	17
2.7.1. Optical Microscopy	17
2.7.2. Atomic Force Microscopy (AFM).....	19
2.7.3. Kelvin Probe Force Microscopy (KPFM).....	23
2.7.4. Scanning Electron Microscopy (SEM).....	25
2.7.5. Raman Spectroscopy	26
2.8. Sensing Applications of Graphene	28
2.8.1. Gas Sensors Based on Pristine Graphene	29
2.8.2. Gas Sensors Based on Defective and Functionalized Graphene	32
2.8.2.1. Chemically Modified Graphene Based Sensors	33
2.8.2.2. Graphene/nanoparticle Hybrid Based Sensors	33
2.8.2.3. Graphene/polymer Hybrid Based Sensors	35

2.8.2.4. Self-Assembled Monolayer Modified Graphene Based Sensors	36
CHAPTER 3. MATERIALS AND METHODS	38
3.1. Materials	38
3.2. Silicon Wafer Oxidation	38
3.3. Cu Foil Annealing	38
3.4. Graphene Growth by CVD Technique	39
3.5. Anisotropic Hydrogen Etching of Graphene with CVD.....	40
3.6. Graphene Transfer onto Substrates	42
3.7. Self-Assembled Monolayer (SAM) Functionalization	44
3.8. Gold Electrode Deposition.....	44
CHAPTER 4. RESULTS AND DISCUSSIONS	47
4.1. Superficial Characterization	47
4.1.1. Optical Characterization	47
4.1.2. Scanning Electron Microscopy (SEM) Characterization.....	54
4.1.3. Atomic Force Microscopy (AFM) Characterization.....	60
4.2. Structural Characterization	64
4.2.1. Raman Spectroscopy Results	65
4.2.2. Kelvin Probe Force Microscopy (KPFM) Results	95
4.3. Sensorial Characterization	96
4.3.1. Quartz Crystal Microbalance (QCM) Results	96
4.3.1.1. CO and CO ₂ Sensing	96
4.3.1.2. NH ₃ and Humidity Sensing	102
4.3.2. Amperometric Characterization	113
CHAPTER 5. CONCLUSIONS	116
REFERENCES	118

LIST OF FIGURES

<u>Figure</u>	<u>Page</u>
Figure 2.1. σ and Π bonding in graphene cell for carbon atoms. Reprinted from (Source: Vaziri (2011)).	4
Figure 2.2. (a) Real lattice structure and (b) First Brillouin zone lattice of graphene. Reprinted with permission from (Source: Neto et al. (2009)). Copyright 2009 American Chemical Society.	5
Figure 2.3. Dispersion relation of graphene in the first Brillouin zone. Reprinted with permission from (Source: Neto et al. (2009)). Copyright 2009 American Chemical Society.	6
Figure 2.4. Phonon branches in graphene (Lazzeri et al., 2008). Reprinted with permission from (Source: Malard et al. (2009)). Copyright 2009 American Chemical Society.	7
Figure 2.5. Rayleigh, Stokes and anti-Stokes scattering processes.	7
Figure 2.6. Raman spectrum of a graphene edge, showing the main Raman features, the D, G and G' bands. Reprinted with permission from (Source: Malard et al. (2009)). Copyright 2009 American Chemical Society.	8
Figure 2.7. Transmittance for an increasing number of layers. Reprinted with permission from (Source: Nair et al. (2008)). Copyright 2008 American Chemical Society.	10
Figure 2.8. Optical microscope image of single-layer, multi-layer and graphite flakes. Reprinted from (Source: Yi (2013)).	11
Figure 2.9. Graphene growth by thermal decomposition of SiC, together with the structural model of bilayer graphene on SiC. Shown as the blue broken line is the buffer layer. Reprinted with permission from (Source: Norimatsu and Kusunoki (2014)). Copyright 2014 American Chemical Society.	12
Figure 2.10. Graphene growth on Cu by CVD:(a) First stage; native oxide on Cu, (b) Second stage; graphene nucleation by CH_4/H_2 exposure, (c) Third stage; enlargement of graphene flakes. Reprinted with permission from (Source: Mattevi et al. (2011)). Copyright 2011 American Chemical Society.	16

Figure 2.11. (a) Optical micrograph of MC flake, consisting of regions of different thickness, (b) Evolution of Raman spectra with the number of graphene layers. Reprinted with permission from (Ferrari et al., 2006). Copyright 2006 American Chemical Society. The spectra are normalized to have the same G peak intensity. Reprinted with permission from (Source: Bonaccorso et al. (2012)). Copyright 2012 American Chemical Society.	18
Figure 2.12. Force distance curve of AFM.	19
Figure 2.13. (a) AFM image and (b) AFM height profile of transferred graphene film. Reprinted with permission from (Source: Zhang et al. (2010)). Copyright 2010 American Chemical Society.	21
Figure 2.14. AFM topography images of annealed polycrystalline Ni thin film (a) before and (b) after the graphene growth Reprinted with permission from (Source: Reina et al. (2008)). Copyright 2008 American Chemical Society.	21
Figure 2.15. (a) AFM topography and (b) height profile of transferred graphene film Reprinted with permission from (Source: Reina et al. (2008)). Copyright 2008 American Chemical Society.	22
Figure 2.16. (a) AFM image of single layered graphene on SiO ₂ /Si. Reprinted with permission from (Source:(Srivastava et al., 2010)). Copyright 2010 American Chemical Society. (b) AFM image and height profile of transferred graphene film. Reprinted with permission from (Source: Bae et al. (2010)). Copyright 2010 American Chemical Society	22
Figure 2.17. A schematic diagram of the gated graphene-device structure with KPFM. Reprinted from(Lee et al., 2009).	24
Figure 2.18. Kelvin voltage maps with external bias (a) 0 V, (b) +1.0 V, and (c) -1.0 V. The left contact was connected to the ground for all the measurements. The voltages represent the work function difference between the AFM tip and the scanned object. Reprinted with permission from (Source: Yan et al. (2011)). Copyright 2011 American Chemical Society.	24
Figure 2.19. Schematic diagram of SEM.	25

Figure 2.20. (Left) First-order G-band process and (Center) one-phonon second-order DR process for the D-band (intervalley process) (top) and for the D' -band (intravalley process) (bottom) and (Right) two-phonon second-order resonance Raman spectral processes (top) for the double resonance G' process, and (bottom) for the triple resonance G' band process (TR) for monolayer graphene (Dresselhaus et al., 2005). For one-phonon, second-order transitions, one of the two scattering events is an elastic scattering event. Resonance points are shown as open circles near the K point (left) and the K' point (right). Reprinted with permission from (Source: Malard et al. (2009)). Copyright 2009 American Chemical Society.	27
Figure 2.21. Schematic view of the electron dispersion of bilayer (2-LG) graphene and its measured G' band. Reprinted with permission from (Source: Malard et al. (2009)). Copyright 2009 American Chemical Society.	27
Figure 2.22. The measured G' Raman band. Reprinted with permission from (Source: Malard et al. (2009)). Copyright 2009 American Chemical Society.	28
Figure 2.23. (a) Chemically induced charge carrier concentration in SLG versus NO_2 concentration; Upper inset: SEM of the sensor device; hall bar width is $1 \mu\text{m}$; Lower inset: Graphene device characteristics under applied electric field. (b) Resistivity (ρ) change under various gas exposures with 1 ppm flow amount. Region I: the sensor response in vacuum; II: exposure to a 5-L volume of a diluted chemical,; III: evacuation; and IV: annealing at 150° . Reprinted with permission from (Source: Schedin et al. (2007)). Copyright 2007 American Chemical Society.	30
Figure 2.24. (a) Graphene based NO_2 gas sensor diagram. Upper and Bottom insets: Optical images. (b) Sensor response under periodic Air - NO_2 gas alteration. Reprinted with permission from (Source: Ko et al. (2010)). Copyright 2010 American Chemical Society.	31
Figure 2.25. (a) Response of NH_3 sensor under in situ UV light illumination. The inset shows the reproducibility of sensor response at 200 ppt of NH_3 exposure. (b) Response of NH_3 sensor without UV light illumination. Reprinted from (Chen et al., 2012).	32

Figure 2.26. (a) P-GNSs based NH ₃ sensor structure, (b) the response of P-GNS-400 at 100 ppm NH ₃ exposure, (c) response and recovery time plot, (d) and (e) are the response values of P-GNS-400 under various NH ₃ concentrations. Reprinted with permission from (Source: Niu et al. (2014)). Copyright 2014 American Chemical Society.	34
Figure 2.27. (a) Structure of flexible gas sensor; (b) Photograph of bent gas sensor based on RGO film anchored on a PET substrate. Reprinted with permission from (Source: Su and Shieh (2014)). Copyright 2014 American Chemical Society.	34
Figure 3.1. SiO ₂ /Si substrates.	38
Figure 3.2. Cu foil annealed at 1080 °C.	39
Figure 3.3. Cu foils annealed at different temperatures.	39
Figure 3.4. Standard Graphene Growth Process	41
Figure 3.5. Graphene Growth and Etching process of CVD graphene.	42
Figure 3.6. Graphene Growth and Etching process of CVD graphene at lower temperature.	42
Figure 3.7. Graphene transfer from Cu foil on to SiO ₂ /Si substrate.	44
Figure 3.8. Chemical structures of (a) MePIFA and (b) DPIFA SAM molecules.	45
Figure 3.9. Gold electrode scheme that was patterned by photolithography process.	46
Figure 4.1. Optical microscopy images of bare and annealed commercial Cu foils. .	47
Figure 4.2. Optical images taken from melted sides of Cu foils annealed at 1075 °C and 1080 °C.	48
Figure 4.3. Optical microscopy image of GRP323 sample.	48
Figure 4.4. Optical microscopy images of GRP402 sample with three different magnifications.	49
Figure 4.5. Optical Microscopy images of GRP345 and GRP356 samaples.	50
Figure 4.6. Optical Microscopy images of etched GRP372 and GRP373 samples. ..	50
Figure 4.7. Optical Microscopy images of GRP379 and GRP380 samples.	51
Figure 4.8. Optical Microscopy images of GRP381 sample.	51
Figure 4.9. Optical Microscopy images of GRP414 and GRP462 samples.	52
Figure 4.10. Optical Microscopy images of GRP429 and GRP438 samples.	52
Figure 4.11. Optical Microscopy images of GRP485 and GRP486 samples.	53
Figure 4.12. Optical Microscopy images of GRP463 with four different magnifications.	54

Figure 4.13. SEM images of GRP394 sample on Cu foil with (a) 1000x, (b) 10000x, (c) 50000x and (d) 100000x magnifications.	55
Figure 4.14. SEM images of GRP393 sample on Cu Foil with (a) 500x, (b) 5000x, (c) 10000x and (d) 50000x magnifications.	55
Figure 4.15. SEM images of (a) GRP345, (b) GRP372, (c) GRP373 and (d) GRP381 samples with (a)-(c) 30 μm and (b)-(c) 20 μm scale bars.	56
Figure 4.16. SEM images of (a) GRP345, (b) GRP372, (c) GRP373 and (d) GRP381 samples with (a)-(c) 5 μm and (b)-(c) 2 μm scale bars.	57
Figure 4.17. SEM images of (a) GRP379 sample with 30 μm , (b) GRP380 sample with 20 μm , (c) GRP379 and (d) GRP380 samples with 5 μm scale bars.	58
Figure 4.18. SEM images of etched GRP429 sample with (a) 50 μm , (b) 10 μm and (c) 1 μm scale bars.	58
Figure 4.19. SEM images of etched GRP485 sample on SiO_2/Si with a)1000x, b) 2500x, c) 5000x and d) 10000x magnifications.	59
Figure 4.20. SEM images of etched GRP486 sample on SiO_2/Si with a)1000x, b) 2500x, c) 5000x and d) 10000x magnifications.	59
Figure 4.21. SEM images of GRP428 sample on gold coated QCM with a)35x, b) 200x and c) 2000x magnifications.	60
Figure 4.22. Surface topography (a, c, and e) and phase contrast (b, d and f) images of bare Cu Foil with 10 μm^2 , 3 μm^2 and 1 μm^2 areas.	61
Figure 4.23. (a) Surface topography and (b) phase contrast images of Cu foils annealed at 1070 $^\circ\text{C}$ taken from 3 μm^2 area.	62
Figure 4.24. (a) Surface topography and (b) phase contrast images of Cu foils annealed at 1073 $^\circ\text{C}$ taken from 1 μm^2 area.	62
Figure 4.25. (a) Surface topography and (b) phase contrast images of Cu foils annealed at 1075 $^\circ\text{C}$ taken from 3 μm^2 area.	63
Figure 4.26. (a) Surface topography and (b) phase contrast images of Cu foils annealed at 1080 $^\circ\text{C}$ taken from 3 μm^2 area.	63
Figure 4.27. Surface topography images of Cu foils annealed at 1080 $^\circ\text{C}$ taken from (a) 10, (b) 5 and (c) 3 μm^2 areas.	64
Figure 4.28. Surface topography and phase contrast images of GRP323 sample from (a) 10 μm^2 , (b) 5 μm^2 and (c) 3 μm^2 area.	64
Figure 4.29. Optical Microscopy images and Raman Spectrum of GRP312 sample. .	65
Figure 4.30. G' band Raman spectrum of GRP312 sample that is fitted with four Lorentzian.	66

Figure 4.31. Optical Microscopy images and Raman Spectrum of GRP318 sample. .	67
Figure 4.32. G' band Raman spectrum of GRP318 sample that is fitted with four Lorentzian.	67
Figure 4.33. Optical Microscopy images and Raman Spectrum of GRP320 sample. .	68
Figure 4.34. G' band Raman spectrum of GRP320 sample that is fitted with four Lorentzian.	69
Figure 4.35. Optical Microscopy images with/without laser reflection and Raman Spectrum of GRP345 sample from etched area.	69
Figure 4.36. Optical Microscopy images with/without laser reflection and Raman Spectrum of GRP345 sample from non-etched area.	70
Figure 4.37. G' band Raman spectrum of GRP345 sample that was fitted with two Lorentzian.	71
Figure 4.38. Optical Microscopy images with/without laser reflection and Raman Spectrum of GRP356 sample from etched area.	71
Figure 4.39. G' band Raman spectrum of GRP356 sample that was fitted with four Lorentzian.	72
Figure 4.40. Optical Microscopy images with/without laser reflection and Raman Spectrum of GRP356 sample from non-etched area.	73
Figure 4.41. G' band Raman spectrum of GRP356 sample that was fitted with two Lorentzian.	73
Figure 4.42. Optical Microscopy images with/without laser reflection and Raman Spectrum of GRP372 sample from non-etched area.	74
Figure 4.43. G' band Raman spectrum of GRP372 sample that was fitted with four Lorentzian.	75
Figure 4.44. Optical Microscopy images with/without laser reflection and Raman Spectrum of GRP373 sample from non-etched area.	75
Figure 4.45. G' band Raman spectrum of GRP373 sample that was fitted with four Lorentzian.	76
Figure 4.46. Optical Microscopy images with/without laser reflection and Raman Spectrum of GRP373 sample from etched area.	77
Figure 4.47. Optical Microscopy images with/without laser reflection and Raman Spectrum of GRP379 sample from etched area.	77
Figure 4.48. Optical Microscopy images with/without laser reflection and Raman Spectrum of GRP379 sample from non-etched area.	78

Figure 4.49. G' band Raman spectrum of GRP379 sample that was fitted with four Lorentzian.	79
Figure 4.50. Optical Microscopy images with/without laser reflection and Raman Spectrum of GRP380 sample from non-etched area.	79
Figure 4.51. G' band Raman spectrum of GRP380 sample that was fitted with two Lorentzian.	80
Figure 4.52. Optical Microscopy images with/without laser reflection and Raman Spectrum of GRP380 sample from etched area.	81
Figure 4.53. G' band Raman spectrum of GRP380 sample that was fitted with four Lorentzian.	81
Figure 4.54. Optical Microscopy images with/without laser reflection and Raman Spectrum of GRP381 sample from etched area.	82
Figure 4.55. Optical Microscopy images with/without laser reflection and Raman Spectrum of GRP381 sample from non-etched area.	82
Figure 4.56. G' band Raman spectrum of GRP381 sample that was fitted with four Lorentzian.	83
Figure 4.57. Optical Microscopy images with/without laser reflection and Raman Spectrum of empty gold quartz crystal.	84
Figure 4.58. Optical Microscopy images with/without laser reflection and Raman Spectrum of GRP353 sample on gold quartz crystal.	84
Figure 4.59. Optical Microscopy images with/without laser reflection and Raman Spectrum of GRP403 sample on gold quartz crystal.	85
Figure 4.60. Optical Microscopy images with/without laser reflection and Raman Spectrum of GRP352 sample on gold quartz crystal.	86
Figure 4.61. Optical Microscopy images with/without laser reflection and Raman Spectrum of GRP414 sample from non-etched area.	86
Figure 4.62. Optical Microscopy images with/without laser reflection and Raman Spectrum of GRP429 sample from etched area.	87
Figure 4.63. Optical Microscopy images with/without laser reflection and Raman Spectrum of GRP429 sample from non-etched area.	87
Figure 4.64. Optical Microscopy images with/without laser reflection and Raman Spectrum of GRP438 sample from non-etched area.	88
Figure 4.65. Optical Microscopy images with/without laser reflection and Raman Spectrum of GRP438 sample from etched area.	88

Figure 4.66. Optical Microscopy images with/without laser reflection and Raman Spectrum of GRP441 sample from non-etched area.	89
Figure 4.67. Optical Microscopy images with/without laser reflection and Raman Spectrum of GRP441 sample from etched area.	90
Figure 4.68. Optical Microscopy images with/without laser reflection and Raman Spectrum of GRP428 sample on quartz crystal.	90
Figure 4.69. Optical Microscopy images with/without laser reflection and Raman Spectrum of GRP439 sample on quartz crystal.	91
Figure 4.70. Optical Microscopy images with/without laser reflection and Raman Spectrum of GRP485 sample from etched region.	91
Figure 4.71. Optical Microscopy images with/without laser reflection and Raman Spectrum of GRP485 sample from non-etched region.	92
Figure 4.72. Optical Microscopy images with/without laser reflection and Raman Spectrum of GRP486 sample from etched region.	92
Figure 4.73. Optical Microscopy images with/without laser reflection and Raman Spectrum of GRP486 sample from middle-lightened region.	93
Figure 4.74. Optical Microscopy images with/without laser reflection and Raman Spectrum of GRP486 sample from darkest region.	94
Figure 4.75. Optical Microscopy images with/without laser reflection and Raman Spectrum of GRP463 sample taken from the gap between two electrodes. Laser can be seen as bright spot in between the two electrodes. ...	94
Figure 4.76. Contact potential differences of bare GRP, modified GRP with MePIFA - DPIFA SAMs and HOPG.	95
Figure 4.77. Frequency change vs. time plot of GRP353 under periodic DA - CO gas flows.	97
Figure 4.78. Frequency change vs. time plot of GRP353 under periodic DA - CO ₂ gas flows.	97
Figure 4.79. Frequency change vs. time plot of GRP403 under periodic DA - CO and DA - CO ₂ gas flows.	98
Figure 4.80. Frequency change vs. time plot of GRP352 under periodic DA - CO gas flows.	99
Figure 4.81. Frequency change vs. time plot of GRP352 under periodic DA - CO ₂ gas flows.	99
Figure 4.82. Frequency change of pristine and Me-PIFA modified graphene under periodic N ₂ - CO gas flows.	100

Figure 4.83. Frequency change of pristine and D-PIFA modified graphene under periodic N ₂ - CO gas flows.	101
Figure 4.84. Frequency change of pristine, Me-PIFA and D-PIFA modified graphene under periodic N ₂ - CO ₂ gas flows.	101
Figure 4.85. Frequency change of pristine, CVD etched GRP429 and GRP438 modified graphene under periodic N ₂ - CO ₂ gas flows.	102
Figure 4.86. Frequency change of GRP456 sample under periodic N ₂ - NH ₃ (red circles), Air - NH ₃ (blue squares) and N ₂ - humidity (green quadrangles) gas flows.	103
Figure 4.87. Frequency change of GRP456 sample (red circles), MePIFA modified GRP439 sample (blue squares) and DPIFA modified GRP439 sample (green quadrangles) under periodic N ₂ - NH ₃ gas flows.	104
Figure 4.88. Least squares fit (dashed lines) using the Langmuir adsorption isotherm model for bare GRP456, MePIFA and DPIFA modified graphene samples against NH ₃	105
Figure 4.89. Frequency change of GRP456 sample (red circles), MePIFA modified GRP439 sample (blue squares) and DPIFA modified GRP439 sample (green quadrangles) under periodic Air - NH ₃ gas flows.	107
Figure 4.90. Frequency change of GRP456 sample (red circles), MePIFA modified GRP439 sample (blue squares) and DPIFA modified GRP439 sample (green quadrangles) under periodic N ₂ - Humidity flows.	107
Figure 4.91. Least squares fit (dashed lines) using the Langmuir adsorption isotherm model for bare GRP456, MePIFA and DPIFA modified graphene samples against Humidity.	108
Figure 4.92. Frequency change of GRP456 sample (red circles), etched GRP485 sample (blue squares) and etched GRP486 sample (green quadrangles) under periodic N ₂ - NH ₃ flows.	109
Figure 4.93. Frequency change of GRP456 sample (red circles), etched GRP485 sample (blue squares) and etched GRP486 sample (green quadrangles) under periodic Air - NH ₃ flows.	110
Figure 4.94. Least squares fit (dashed lines) using the Langmuir adsorption isotherm model for GRP456, EGRP485 and GRP486 against NH ₃	110
Figure 4.95. Frequency change of GRP456 sample (red circles), etched GRP485 sample (blue squares) and etched GRP486 sample (green quadrangles) under periodic N ₂ - Humidity flows.	111

Figure 4.96. Least squares fit (dashed lines) using the Langmuir adsorption isotherm model for GRP456, EGRP485 and GRP486 against humidity. 112

Figure 4.97. Resistance changes of GRP463 in periodic N₂ - NH₃ (red circles) and periodic Air - NH₃ (blue squares) ambient. 113

Figure 4.98. Resistance response of GRP463 in periodic N₂ - humidity ambient. 114

Figure 4.99. Resistance comparison of pristine graphene GRP (red circles), MePIFA modified GRP (blue squares) and DPIFA modified GRP (green quadrangles) in periodic DA - NH₃ and N₂ - Humidity ambient. 115



LIST OF TABLES

<u>Table</u>	<u>Page</u>
Table 2.1. Graphene Detection Limit (DL) of NO, NO ₂ , NH ₃ , N ₂ O, O ₂ , SO ₂ , CO ₂ and H ₂ O. Reprinted from (Chen et al., 2012).	31
Table 3.1. Annealing, Growth and Gas Flow Parameters of Graphene Samples.	40
Table 3.2. CVD Grown and Etched Graphene Samples.	43
Table 4.1. Langmuir adsorption isotherm constants have been derived for NH ₃	106
Table 4.2. Langmuir adsorption isotherm constants have been derived for humidity.	108
Table 4.3. Langmuir adsorption isotherm constants have been derived for NH ₃	111
Table 4.4. Langmuir adsorption isotherm constants have been derived for humidity.	112

LIST OF SYMBOLS

p_x, p_y, p_z	$3p$ state electrons
π	Pi Bond
σ	Sigma Bond
Γ	Center point in the first Brillouin zone
κ	Corner point in the first Brillouin zone
κ'	Other corner point in the first Brillouin zone
M	Center of the corner points in the first Brillouin zone
π^*	Anti-bonding
G_0	Optical conductance
Ω	Ohm unit
α	fine structure constant
$^{\circ}\text{C}$	Degree of Celcius
α	thermal expansion coefficient

CHAPTER 1

INTRODUCTION

In modern age, potential technology replaces the existing limitations that based on the laws of physics with current nano-sized devices that obey quantum mechanical effects. In that manner, current conventional computer hardware lithography capabilities are used to design and create the smaller circuit components for modern electronic devices which also use less power, take up less space and are more reliable (Sze and Ng, 2006), (James, 2010).

Silicon is the widely used semiconducting material in the semiconducting industry. It is easy to tune electronic properties of silicon and also production processes with silicon are not complicated, however; its use limits the improvement of technology due to its inability in covering large areas, nonconformity in flexible platform and inadequate physical properties (Novoselov et al., 2004). Therefore, research needed for something that can be adjunct to silicon. Graphene, with unique physical and electronic properties, is a promising candidate that cannot replace the silicon dynasty alone, but support it in fabrication of certain devices (Gautam and Jayatissa, 2011).

Graphene is a one-atomic layer thick material that carbon atoms are sp^2 bonded and densely packed into two-dimensional (2D) honeycomb lattice. The separation of carbon atoms is 0.142 nm in graphene and when graphene sheet is wrapped up; fullerenes and when it rolled into spherical and cylindrical shape carbon nanotubes are formed. In graphite, individual graphene layers are bounded weakly from one another with separation of 0.335 nm.

Graphene has honeycomb lattice structure that can be thought of two equivalents triangular sublattices A and B with inversion symmetry and corresponding energy bands of them coincide at zero energy at Dirac points; K points of reciprocal lattice. The velocity of the electrons near K point is 106 m/s and the dispersion relation near Dirac points is linear which is similar to a system of relativistic particles with zero effective mass. Thus, due to the zero band-gap, graphene is called as zero band gap semiconductor or semimetal. When the number of the graphene layers increase, the energy bands start to overlap. For bilayer graphene, the overlap is 1.6 meV.

Graphene was first discovered by Geim and Novoselov by isolating it experimentally in 2004 (Geim and Novoselov, 2007). Since that time, graphene has been attracted great attention due to its unique electronic (Novoselov et al., 2004), (Neto et al., 2009)),

optical (Wang et al., 2008), thermal (Balandin et al., 2008) and mechanical (Stankovich et al., 2006) properties. Graphene has ambipolar field effect (Novoselov et al., 2004), anomalous quantum Hall effect at room temperature, extremely high charge carrier mobility ($\sim 230,000 \text{ cm}^2/\text{V s}$) (Novoselov et al., 2004), (Dean et al., 2010), (Bolotin et al., 2008), (Morozov et al., 2008)), and high elasticity (Kim et al., 2009). It also exhibit optical transparency of $\sim 97.7\%$ (Blake et al., 2008) and high thermal conductivity at room temperature (Balandin et al., 2008).

Despite of the promising properties mentioned above, graphene is very suitable for field-effect transistor, capacitor, energy storage, sensor and photovoltaic applications. Especially, due to the sensitivity of various gas species or bio-molecules, graphene based sensors have promising responses. Additionally, graphene can also be used as transparent and flexible anode material instead of indium tin oxide (ITO) in photovoltaic, liquid crystal displays (LCDs) and organic light emitting diodes (OLEDs) (Blake et al., 2008), (Li et al., 2009), (Gomez De Arco et al., 2010).

CHAPTER 2

LITERATURE REVIEW

2.1. History of Graphene

Graphene was first cited by Canadian physicist Philip Russel Wallace in 1946 (Wallace, 1947). He constructed three-dimensional honeycomb structured carbon atoms and thus invented the two-dimensional graphene analog. He showed that graphite was composed of graphene layers that are stack on top of each other. Then, he used the graphene calculations to get information about graphite.

In 1984 it was shown that in graphene the electric current was induced by effectively massless charge carriers and the name of ' graphene ' was first used to describe the layers of graphite in 1987 (Semenoff (1984), Boehm et al. (1986)). The growth of graphene has been studied since 1970s however; strong surface interactions suppressed the exact properties during experimental measurements. Graphene was first discovered experimentally by Andre Geim and Konstantin Novoselov in 2004 (Novoselov et al., 2004). They stacked a piece of scotch tape to a piece of graphite cube and then pilled of it with graphite flakes on it. They repeated this process for many times separating graphite into thinner and thinner flakes, until they got only one atom thick flake. Geim and Novoselov showed that two-dimensional case is possible physically and Wallace's graphene was invented in this way.

2.2. Crystal Structure of Graphene

Graphene is composed of sp^2 -bonded carbon atoms that are densely packed in a honeycomb crystal lattice. Each carbon atoms in this lattice contains six electrons. Two of them are located in the innermost $1s^2$ orbital and the other four electrons are located in the outer valence shell. Valence electrons are filling the s electrons and $3p$ states where $3p$ electrons can be signified as p_x , p_y and p_z . According to hybridization theory (Jorio et al., 2011), in graphene to form the sp^2 bonding, s electron hybridize with two p_x and p_y electrons. Bonding between the p_x and p_y electrons is called σ bonding

and p_z electrons form π bonding. The angle between σ bonds is 120° which forms a hexagonal structure. Due to the strong covalent bonding of σ bonds, graphene has excellent mechanical stiffness.

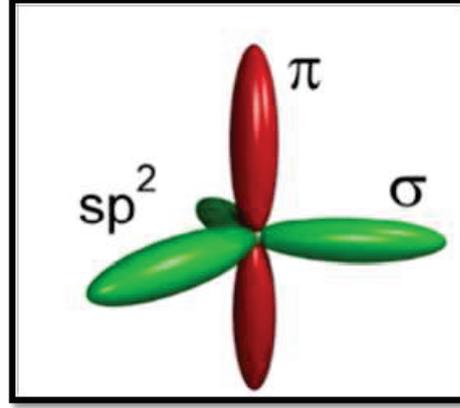


Figure 2.1. σ and π bonding in graphene cell for carbon atoms. Reprinted from (Source: Vaziri (2011)).

The unit cell of the graphene hexagonal layer contains two carbon atoms: A and B . As shown in Figure (a), (a_1) and (a_2) are the basis vectors of the real space crystal structure where $(a_1) = (1, \sqrt{3})a_0$ and $(a_2) = (-1, \sqrt{3})a_0$ in which a_0 is the lattice constant of 2.46 \AA . Reciprocal space also has hexagonal structure with the vectors of (b_1) and (b_2) . Due to the relation of $a_i b_i = 2\pi$

$$b_1 = \frac{2\pi}{a_1} = \frac{2\pi}{a_0} \left(1, \frac{1}{\sqrt{3}}\right) = \frac{2\pi}{\sqrt{3}a_0} (\sqrt{3}, 1) \quad (2.1)$$

and

$$b_2 = \frac{2\pi}{a_2} = \frac{2\pi}{a_0} \left(-1, \frac{1}{\sqrt{3}}\right) = \frac{2\pi}{\sqrt{3}a_0} (-\sqrt{3}, 1) \quad (2.2)$$

2.3. Electronic Properties

The first Brillouin zone is shown in Figure 2. 2 (b), where center point represented with Γ , corner points with κ and κ' and center of κ and κ' with M . According to tight binding theory, only the nearest neighbor atoms in primitive cell can contribute to the energy band. Therefore, electron hopping is directed from A to B and also from B to A .

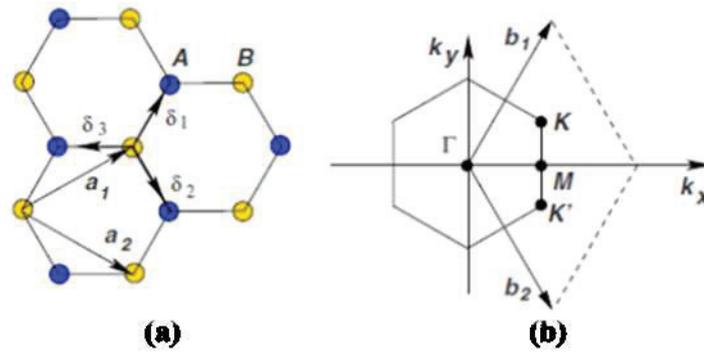


Figure 2.2. (a) Real lattice structure and (b) First Brillouin zone lattice of graphene. Reprinted with permission from (Source: Neto et al. (2009)). Copyright 2009 American Chemical Society.

From the $E-k$ relation (Figure 2.3), we can see that the valence band touch conduction band at κ and κ' positions. At κ point, the energy of graphene is equal to the overlapping integral and bonding π and antibonding π^* states touch at κ pointing forming a zero-gap semiconductor or zero-Density of States (DOS) metal (Tománek et al., 2007). Pauli Exclusion Principle states that two electrons that have opposite spin can fill each energy state. thus, while π bond is filled with two electrons, π^* bond is empty (Jorio, Dresselhaus, Saito, and Dresselhaus, Jorio et al.).

This linear relation leads to zero effective mass for charge carriers. Thus, they are relativistic particles like photons and obey Dirac equation. Energy band gap can be produced with some perturbation or symmetry break such as inducing inequivalent atoms of A and B in the unit cell. Interlayer interactions between the layers of multilayer graphene or between the substrate and graphene layer can induce symmetry break. In bilayer graphene, applied external electric field will also open a gap (Zhang et al., 2009).

At room temperature, graphene shows high electron mobility that exceeds 2000 $\text{cm}^2/\text{V s}$ (Zhang et al., 2005), (Novoselov et al., 2005). For field effect transistors, this high mobility, sensitivity to field effect and large lateral extension properties make graphene important alternative. Between the temperatures of 1-100 K, mobility is independent of temperature and scattering is related to graphene defects (Morozov et al., 2008), (Novoselov et al., 2005). Mobilities exceeding 25,000 $\text{cm}^2/\text{V s}$ by improved sample preparation such as annealing during the post-fabrication and in oxide supported graphene devices 40,000 $\text{cm}^2/\text{V s}$ achieved due to the optical phonons of the substrate at room temperature (Chen et al., 2008). Higher mobilities ($\sim 200,000 \text{ cm}^2/\text{V s}$) can be achieved with the isolation

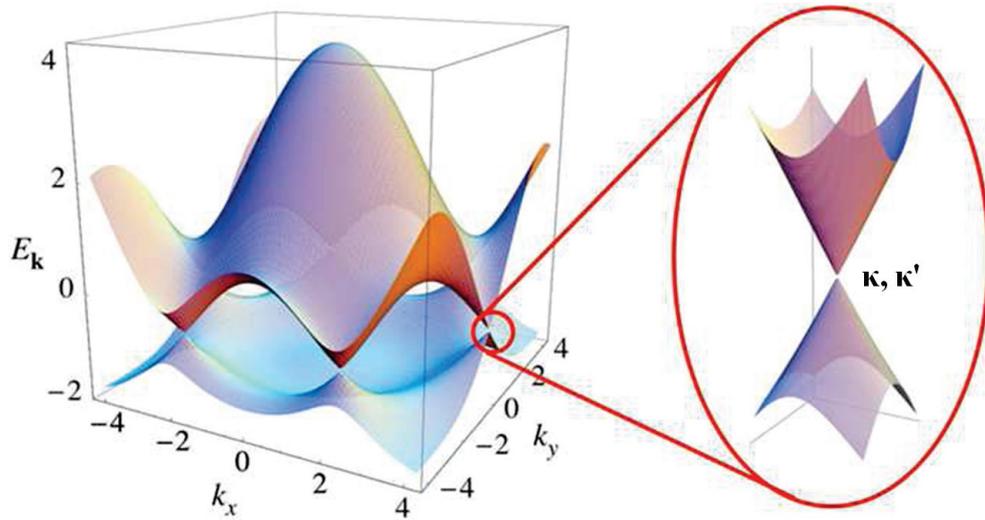


Figure 2.3. Dispersion relation of graphene in the first Brillouin zone. Reprinted with permission from (Source: Neto et al. (2009)). Copyright 2009 American Chemical Society.

of the graphene from its substrate and annealing (Bolotin et al., 2008), (Du et al., 2008), (Bolotin et al., 2008)). In gas sensing applications, device mobility is modified with the adsorption of gas molecules therefore it is very important for investigation.

2.4. Vibrational Properties

Since each unit cell of graphene contains two atoms, total of six branches of phonons exist: three of them are acoustic and the other three are optical phonon branches (Lazzeri et al., 2008). Both acoustic phonon modes and optical phonon modes have one longitudinal mode (LA and LO) and two transverse modes (TA and TO). Longitudinal modes are in-plane but transverse modes are including both in-plane (iTA and iTTO) and out-of-plane (oTA and oTO) vibrations as shown in Figure 2.4.

There are three scattering process in a material when the light radiation incidence. Stokes scattering process occurs when the frequency of the scattered photon is less than the frequency of the incident photon and the energy is added to the sample. In anti-Stokes, the frequency of the scattered photon is greater than the frequency of the incident photon and a phonon is annihilated from the sample. If the scattered photon and the incident photon frequencies are the same, Rayleigh scattering occurs. These scattering processes are shown in Figure 2.5.

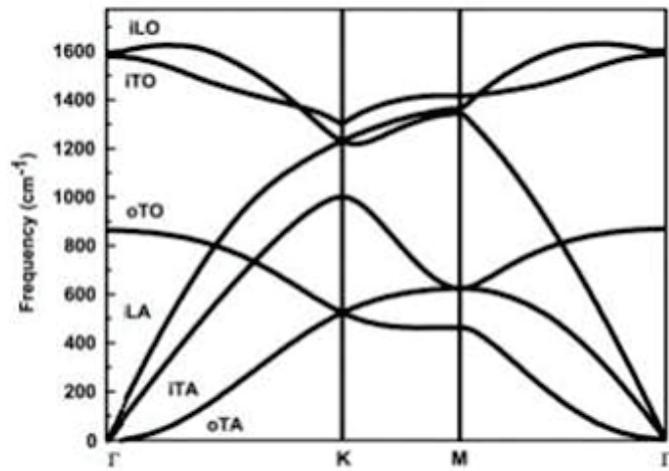


Figure 2.4. Phonon branches in graphene (Lazzeri et al., 2008). Reprinted with permission from (Source: Malard et al. (2009)). Copyright 2009 American Chemical Society.

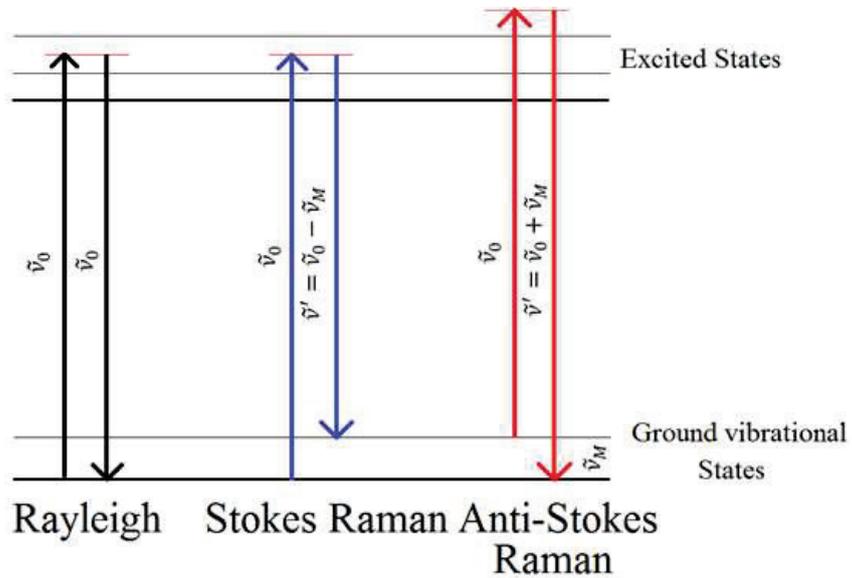


Figure 2.5. Rayleigh, Stokes and anti-Stokes scattering processes.

In another way, Stokes process is the photon shifting to a longer wavelength and lower energy while anti-Stokes process is the shifting to a shorter wavelength with higher energy. After electron excitation into higher energy level due to the incident photon, electron decays back down to a lower energy level (Stokes) or to the ground state (anti-Stokes) with emitting a photon.

A Raman spectrum consists of a plot of intensity which represents the count of photons versus Raman shift (cm^{-1}). Raman shift represents the frequency or energy difference between the incident and scattered photon. Raman spectra peaks arise from the inelastic scattering of photons and gives us information of the vibrational modes of the atoms in the unit cell.

Typical Raman spectrum of graphene exhibits two distinct modes; the G peak and the 2D band. The G peak is located around 1580 cm^{-1} and represents an in-plane vibration mode. 2D (some authors prefer G') band arises due to a double resonant Raman process and located around 2660 cm^{-1} . The presence of strong 2D band confirms the occurrence of monolayer graphene. And for multilayer graphene, 2D becomes less Raman active. The peak located around 1350 cm^{-1} is called D band and it illustrates the presence of some the structural defects in the graphene layer. G' band located around 2700 cm^{-1} (Ferrari et al., 2006). Raman spectrum of graphene edge taken with laser excitation energy of 2.41 eV is shown in Figure 2.6.

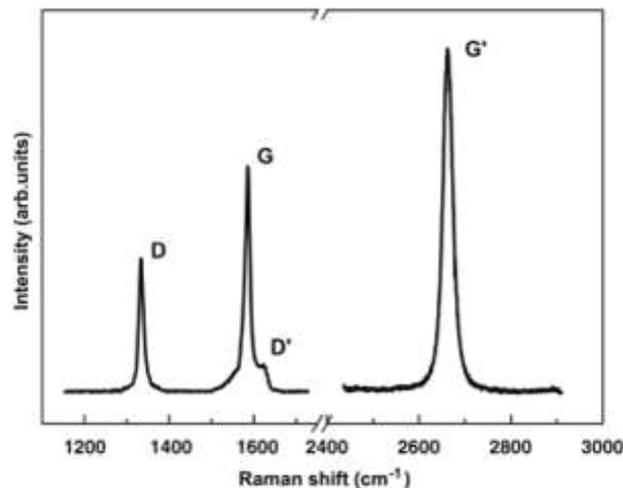


Figure 2.6. Raman spectrum of a graphene edge, showing the main Raman features, the D, G and G' bands. Reprinted with permission from (Source: Malard et al. (2009)). Copyright 2009 American Chemical Society.

In the study of Ferrari *et al.*, 2D band Raman signals are evaluated with the addi-

tion of each extra layer of graphene (Ferrari et al., 2006). Double-resonance model is used to explain this behavior and as a result obtained Raman spectrum is used for the identification of the exact number of graphene layers using G and 2D bands. G band may splitted into two peaks, G and D' peaks if surface charges or random impurities are presented in graphene and interact with the extended phonon modes. Additionally, Gupta *et al.* have shown that G peak position is related with the number of layers therefore such an ability is essential for material characterization and graphene structure optimization for device applications (Gupta et al., 2006).

2.5. Optical Properties

Besides having extraordinary electrical properties, graphene has unique optical properties. Due to its electronic properties, high opacity for an atomic monolayer of graphene is produced. It absorbs 2.5% of white light (Nair et al., 2008), (Kuzmenko et al., 2008), and it also exhibit optical transparency of $\sim 97.7\%$ (Blake et al., 2008). This transparency and conductance values makes it comparable alternative of ITO in solar cells. LCDs and LEDs. For biosensing applications, it also exhibit strong fluorescence quenching.

A freestanding single-layer graphene's transmittance can be calculated using Fresnel equations with a fixed universal optical conductance $G_0 = e^2/(4\hbar) \approx 6.08 \times 10^{-5} \Omega^{-1}$ (Kuzmenko et al., 2008);

$$T = (1 + 0.5\pi\alpha)^{-2} \approx 1 - \pi\alpha \approx 97.7\% \quad (2.3)$$

where α is the fine structure constant and $\alpha = e^2/(4\pi\epsilon_0\hbar c) = G_0/(\pi\epsilon_0 c) \approx 1/137$ (Nair et al., 2008). Single layer graphene reflects only $\langle 0.1\%$ of the incident light in the visible region and this ratio rises to $\sim 2\%$ for ten layers. Therefore, each layer absorb $A \approx 1 - T \approx \pi\alpha \approx 2.3\%$ over the visible spectrum (Figure 2.7).

In a few-layer graphene (FLG), with little perturbation from the adjacent layers, each graphene sheet can be seen as a 2D electron gas. This situation makes FLG act as non-interacting SLG optically (Bonaccorso et al., 2010). Single-layer graphene has nearly flat absorption spectrum between 300 to 2,500 nm with an appeared peak in the UV region at ~ 270 nm arises from the exciton-shift of graphene DOS. In the spectrum of FLG, at lower energies some absorption features due to the interband transitions (Wang et al., 2008).

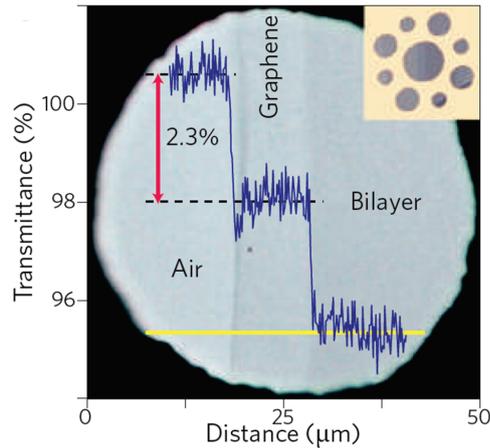


Figure 2.7. Transmittance for an increasing number of layers. Reprinted with permission from (Source: Nair et al. (2008)). Copyright 2008 American Chemical Society.

2.6. Graphene Production Methods

For graphene based-electronics it is very important to produce controllable, cost-effective and uniform graphene films. Numerous methods are used to synthesize graphene but mostly used four are; mechanical exfoliation of atomic layers from highly oriented pyrolytic graphite, HOPG, epitaxial growth on different substrates, chemical vapor deposition (CVD) growth of graphene on metals and chemical reduction from graphite oxide (GO).

High quality graphene based on crystallite size and mobility can be achieved by mechanical exfoliation method, however, sample size is limited. Largest areas are possible with reduction from GO method but this time film quality decreases. Due to the quality and size, CVD synthesized graphene falls in between these methods.

2.6.1. Mechanical Exfoliation

Graphene was first discovered by Novoselov *et al.* using mechanical exfoliation of graphene layers from graphite in 2004 (Novoselov et al., 2004). Graphite consists of sheets of graphene that are kept together by van der Waals (vdW). Therefore, graphite can be exfoliated easily with a scotch tape by applying normal force. This peeling process can lead to multilayer and even single layer graphene.

Graphene flakes are then transferred onto a suitable substrate such as silicon dioxide (SiO_2) with the oxide thickness of 90 nm or 300 nm (Lemme, 2010). In visible range, graphene flakes can be distinguished under an optical microscope. While thick graphene or graphite flakes appear more bluish, few and single layer graphene are seen dark and light purple, respectively, as shown in Figure 2.8.

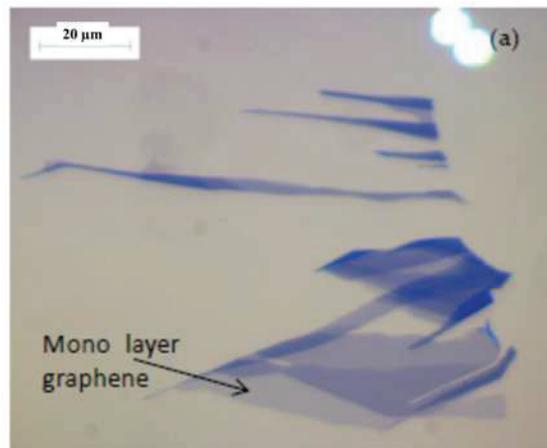


Figure 2.8. Optical microscope image of single-layer, multi-layer and graphite flakes. Reprinted from (Source: Yi (2013)).

Many outstanding properties of high-quality and large-area graphene flakes have been obtained by using this method. However, this method is not appropriate in laboratory researches as it is time consuming to get single layer. Additionally, in industrial production it is impossible to scale up graphene by exfoliation.

2.6.2. Thermal Decomposition of SiC

One of the most frequently used techniques of graphene growth is the thermal decomposition of Si on the (0001) surface of single crystal of 6H-SiC (Wu et al., 2009). Graphitization of single crystal SiC surface was first studied by Badami in 1965 (Badami, 1965). By heated up to 2180 °C using X-ray diffraction, SiC was decomposed and he found that the c-axis of graphite is also along the c-axis of the hexagonal SiC crystal (Norimatsu and Kusunoki, 2014). In 1975 van Bommel *et al.* demonstrated the crystallographic orientation relation between graphite and SiC by using a low-energy electron diffraction (LEED) experiment (Van Bommel et al., 1975). In this study it is shown that

$(11\bar{2}0)_{\text{graphite}}$ and $(0002)_{\text{graphite}}$ planes are parallel to the $(1\bar{1}00)_{\text{SiC}}$ and $(0001)_{\text{SiC}}$ planes, respectively. The graphitization is proceeded by the $6\sqrt{3} \times 6\sqrt{3}R30$ surface reconstruction phase. Forbeaux *et al.* studied the electronic states of graphite on SiC(0001) by using angle-resolved inverse photoemission spectroscopy (Forbeaux *et al.*, 1998).

In 2000, Kusunoki *et al.* was observed FLG on SiC(0001) using Transmission Electron Microscope (TEM). After that observation many studies were carried using inhomogeneous graphene layers that were obtained by thermal annealing of SiC under ultra high vacuum (UHV) (Berger *et al.*, 2004), (Berger *et al.*, 2006), (Ohta *et al.*, 2006). Homogeneous graphene growth was first achieved by annealing SiC in an argon atmosphere to suppress decomposition rate and improve the quality of graphene (Virojanadara *et al.*, 2008), (Emtsev *et al.*, 2009).

In thermal decomposition process, H_2 etched surface of 6H-SiC is heated to temperatures of 1250-1450 °C for 1 to 20 min, graphene sheets are formed. Depending on the decomposition temperature, formed graphene has one to three layers. Large area production of graphene looks attractive by this method. However, issues like thickness control of layers, reproducibility of large area graphene and increasing the graphene quality have to be solved before adopting at an industry. Basic graphene growth by thermal decomposition process is shown in Figure 2.9 by structural model illustration and TEM micrograph.

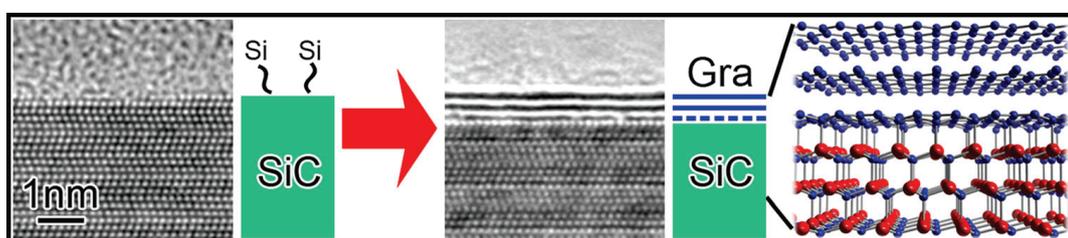


Figure 2.9. Graphene growth by thermal decomposition of SiC, together with the structural model of bilayer graphene on SiC. Shown as the blue broken line is the buffer layer. Reprinted with permission from (Source: Norimatsu and Kusunoki (2014)). Copyright 2014 American Chemical Society.

2.6.3. Unzipping CNTs

A carbon nanotube (CNT), as the name indicates, made of carbon atoms with a tube-shaped structure. The bonding between the carbon atoms is very strong and tubes have high aspect ratios. CNTs may have different properties in length, thickness and number of layers. The metallic or semiconductor characteristics of CNTs depend on how the graphene sheet has rolled up to form tube. When the graphene has rolled up, it forms CNTs. Thus, if a CNT is unzipped, graphene nanoribbon is obtained.

There are two different approaches for unzipping CNTs; chemical treatment and plasma etching. In chemical treatment method, Kosynkin *et al.* suspended CNTs in concentrated sulfuric acid solution for 1-12 h and dilute potassium permanganate is added (Kosynkin *et al.*, 2009). Then solution was stirred at room temperature and heated to 55-70 °C for an hour. After the quenching and filtering, the remaining solid was rinsed in acidic water and ethanol. This treatment unzips the CNTs however; obtained graphene sheet is highly oxidized. Therefore, additional reduction processes are needed to get pristine graphene. In plasma etching method, Jiao *et al.* dispersed multi-wall CNTs (MWCNTs) in 1% Tween 20 aqueous solution and centrifuged to remove aggregates (Jiao *et al.*, 2009). Then MWCNT suspension was coated on Si substrate. After an applied pretreatment procedure, sample was calcined to remove Tween 20. PMMA film was then spin-coated and baked on a hot plate. To etch PMMA-MWCNT film, 10 Watt Ar plasma was applied at 40 mTorr pressure. After the transfer process on Si/SiO₂ substrate, PMMA was removed in acetone solvent.

When compared to chemical unzipping, this method produces graphene samples with higher quality. However, applied complex preparation and etching processes and also inefficiency of large scale production makes this method unfavorable.

2.6.4. Chemical Vapor Deposition (CVD)

CVD is the mostly used synthesis method due to its advantages to produce high quality mono-layer graphene. In this technique, carbon precursors (methane CH₄, ethylene C₂H₄) are deposited onto the surfaces of various metals such as Nickel (Ni) and Copper (Cu) (Kim *et al.*, 2009), (Reina *et al.*, 2008), (Eom *et al.*, 2009), (Levendorf *et al.*, 2009).

In order to obtain large scale high quality monolayer graphene, there are some

parameters that have to be optimized such as: flow rate of precursors, inert and reducing gases, reaction chamber temperature, heating and cooling rates, and the quality and thickness of the metal substrates.

Ni substrate is the one of the mostly used metal substrate in the growth of graphene with CVD. Ni film is firstly deposited on SiO₂/Si substrate with ~ 500 nm thickness using thermal evaporation or sputtering system. In the first step of the graphene growth with CVD, Ni substrate is heated to 1000 °C for 20 min under Ar and H₂ flow. This process let polycrystalline Ni to form larger sized grains with lower roughness which allows better uniformity of graphene grown on top of Ni substrate. Then, the sample is maintained at 1000 °C under the flow of H₂ with 1500 sccm and the flow of methane with 25 sccm during 10 min.

During the CVD process, graphene growth occurs with the precipitation of carbon as it is cooled. In the study of Reina *et al.*, they show that slower cooling rates less than 25 °C/min gives better area cover of mono to double layer graphene films than faster cooling rates (> 100 °C/min). For very slow cooling rates of 4 °C/min, maximum coverage with 87% is shown for less layer number than double-layer graphene (Reina et al., 2008). Li *et al.* used Cu substrate to grow graphene by a surface catalyzed process (Li et al., 2009). Even at low temperature, when compared to Ni, the solubility of carbon in Cu is relatively low. Since the process is self-limiting, a highly uniform graphene thin film, that is predominantly single layer, can be produced.

Graphene films produced using CVD technique have excellent electrical properties and large area coverage. CVD technique also allows transferring of graphene to other substrates such as silicon, glass and PDMS. These advantages make CVD based graphene an important alternative for applications of photovoltaic and flexible electronics.

CVD process involves three main stages. The first one is the catalyst film annealing at the temperatures between 900 and 1000 °C. Annealing process induces the recrystallization and grain size growth which leads to continuous graphene film deposition. Additionally, by annealing the Ni films, it is possible to induce a preferential orientation of the film towards the Ni (111) surface (Zhang et al., 2010). The annealing treatment must be carried out under a gas mixture of Ar (50-60% vol.) and H₂ (40-50% vol). Hydrogen plays a critical role in CVD grown graphene as it terminates graphene edges and help C atoms to diffuse through top layer and catalyst film to form adlayer graphene (Zhang et al., 2014).

The second step is an exposure to CH₄ After annealing process, during the exposure, temperature should be the same as the annealing temperature and it is very important

to expose metal film surface with diluted methane gas. The hydrocarbon gas is the same as the previous Ar and H₂ volume flow rates. During this process, methane is decomposed catalytically on the surface of metal film to produce carbon atoms on its surface. At these temperatures, carbon diffusion into the Ni film always occurs.

The last stage is the cooling of the metal film. If Ni is used as metal substrate annealing process is applied to promote carbon segregation that is stored inside the Ni film. Additionally, morphology of the few-layered graphene films is affected by the cooling rate. According to the study of Alfonso Reina *et al.*, cooling rates larger than 100 °C min⁻¹ shows multilayer graphene with more than two layers precipitated around the grain boundaries of the thin Ni film (Reina *et al.*, 2008).

Catalysis with atomically thin terraces including vicinal surfaces and different dimensional edges are great growing sides for graphene due to their extra dangling bonds. Therefore, reconstruction of Cu surface by pre-treatment makes Cu favorable catalysis for graphene. Terraced structure of Cu for increasing the density of nucleation sites are obtained at higher temperatures (Robertson, 1964), (Chen *et al.*, 2010)).

Several carbon allotropes including graphite (Ong *et al.*, 1992), diamond (Constant *et al.*, 1997), carbon nanotubes (Zhou *et al.*, 2006), (Ding *et al.*, 2009) and graphene (Li *et al.*, 2009) has been grown by using Cu as catalyzer. Graphene growth on Cu involves thermal decomposition of methane gas over the Cu substrate at higher temperatures. In the deposition process Cu foils with the thicknesses ranging from 25-50 μm (Li *et al.*, 2009), (Bae *et al.*, 2010), (Wei *et al.*, 2009) and Cu thin films deposited by e-beam (Ismach *et al.*, 2010), (Lee *et al.*, 2010), and thermal evaporation (Levendorf *et al.*, 2009), (Lee and Lee, 2010) on SiO₂/Si substrates (thickness > 500 nm) have been widely used .

CVD grown graphene on Cu has been obtained at temperatures ranging between 800-1000 °C (Lee and Lee, 2010), (Cai *et al.*, 2009) under low (0.5-50 Torr) (Li *et al.*, 2009), (Levendorf *et al.*, 2009) or atmospheric pressure (Lee *et al.*, 2010) with various methane and H₂ gas mixture ratios.

In achieving high quality graphene layers, pre-treatment of Cu foils has several important benefits. For example, as-received Cu substrates are coated with native oxide layer (CuO, Cu₂O) and this layer reduces the catalytic activity of Cu (Butt, 1983). Therefore, annealing treatment removes the oxide layer and also increases the Cu grain sizes which leads to more favorable nucleation sides on surface. Pre-treatment process typically carried out at temperatures near 1000 °C for 30 min annealing time (Li *et al.* (2009), Bae *et al.* (2010), Lee *et al.* (2010), Cai *et al.* (2009)).

Nucleation density and graphene flake size features are controllable parameters

by tuning the pre-treatment conditions, methane partial pressure and also growth chamber pressure (Li et al., 2009). Additionally, weak interaction between Cu and graphene leads flakes to expand over the grains by slight structural disruption (Mattevi et al., 2011). Thermal expansion coefficient (TEC) difference between graphene and Cu creates wrinkles on graphene ($\alpha_{graphene} = -6 \times 10^{-6}/K$ at 27 °C; $\alpha_{Cu} = 24 \times 10^{-6}/K$ (Bao et al., 2009), (Nelson and Riley, 1945). This large and negative thermal expansion coefficient constitutes shrinkage of Cu during cooling process and thus induces mechanical stress on graphene which induces wrinkle formation (Mattevi et al., 2011).

Graphene growth on Cu has three main stages (Figure 2.10). In the first stage, on Cu surface native oxide layer is present and by annealing under H₂ flow, this layer is removed, grains are expand and surface defects are annihilated. In the second stage, initial graphene domains are nucleated by the exposure of CH₄/H₂ atmosphere. Domains get the lattice orientations of the underneath Cu grains. At the last stage, graphene domains are enlarged with increasing growing time and finally they converge by leading continuous graphene film.

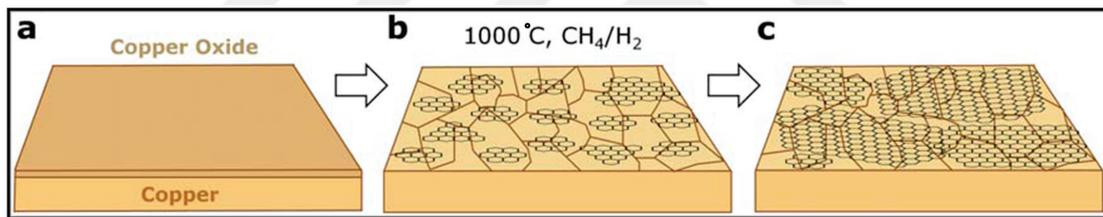


Figure 2.10. Graphene growth on Cu by CVD:(a) First stage; native oxide on Cu, (b) Second stage; graphene nucleation by CH₄/H₂ exposure, (c) Third stage; enlargement of graphene flakes. Reprinted with permission from (Source: Mattevi et al. (2011)). Copyright 2011 American Chemical Society.

2.7. Graphene Characterization Techniques

In characterization of graphene, optical microscopy is mostly used in correlation with Raman spectroscopy. Especially for height measurements Atomic Force Microscopy is used and contact potential difference is measured by Kelvin Probe Force Microscopy. These and other characterization techniques are discussed in detail at following subsections.

2.7.1. Optical Microscopy

Optical microscopy is an important tool to characterize graphene flakes at large scales. With the combination of Raman spectrometry, it gives basic information about the layer number. In optical microscopy, graphene coated areas and number of layers become distinguishable by their contrast (Blake et al., 2007).

Graphene layers are mostly observed by optical microscopy on a SiO₂ thickness of 300 nm. However, a little change in the thickness (e.g. 315 nm) can significantly affects the contrast (Geim and Novoselov, 2007). Additionally, in the study of Blake *et al.* showed that laboratory conditions, quality difference, optical path of the observation and also the opacity of graphene are other important factors that must be optimized to make reliable comparison (Blake et al., 2007). By using the Fresnel theory, they have demonstrated that contrast can be maximized for any SiO₂ thickness by using appropriate filters and also on other thin films such as Si₃N₄ and PMMA.

In the study of Bonaccorso *et al.* optical microscopy images of graphene layers produced by mechanical exfoliation method were used in Raman spectroscopy investigation to define the number of layers (Figure 2.11) (Bonaccorso et al., 2012).

Similarly Teo *et al.* investigated both theoretically and experimentally the visibility of single layer of graphene on various types of substrates by coating a resist layer with optimum thickness (Teo et al., 2008).

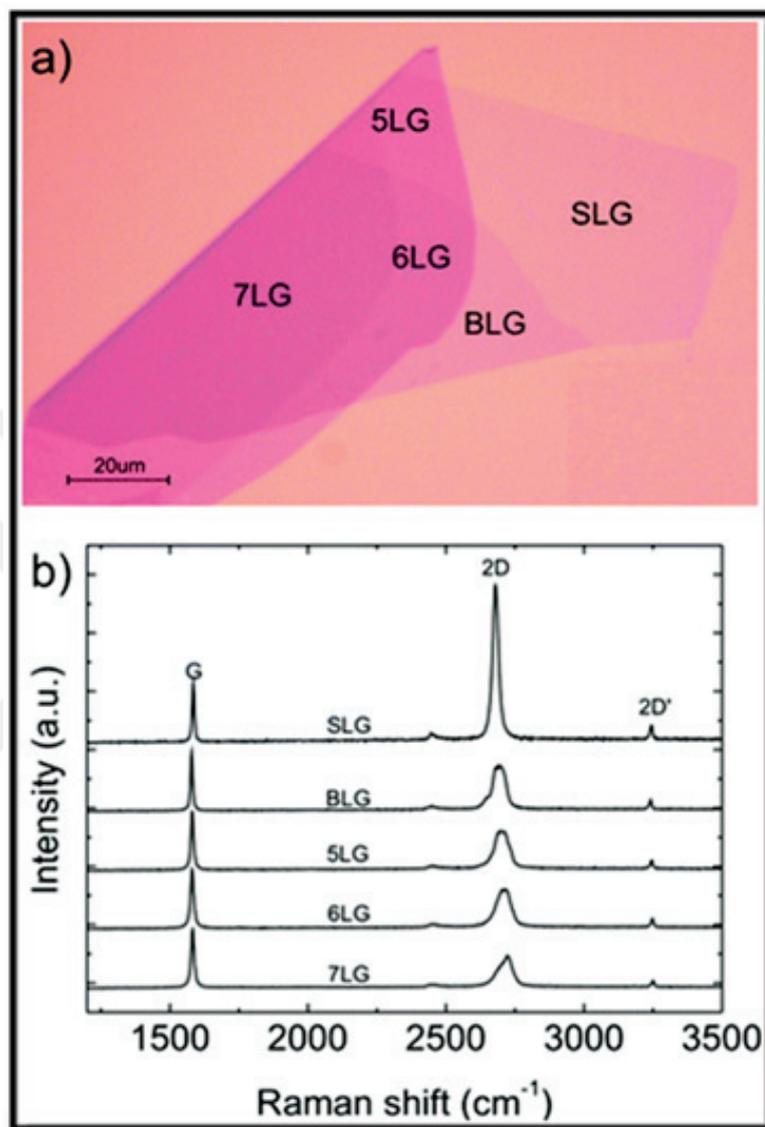


Figure 2.11. (a) Optical micrograph of MC flake, consisting of regions of different thickness, (b) Evolution of Raman spectra with the number of graphene layers. Reprinted with permission from (Ferrari et al., 2006). Copyright 2006 American Chemical Society. The spectra are normalized to have the same G peak intensity. Reprinted with permission from (Source: Bonaccorso et al. (2012)). Copyright 2012 American Chemical Society.

2.7.2. Atomic Force Microscopy (AFM)

Atomic Force Microscopy (AFM) is the one of the mostly used scanning probe microscopy technique that is used in both of the surface characterization of thin film substrate graphene grown and in the measuring of the graphene film thicknesses (Reina et al., 2008), (Zhang et al., 2010), (Mattevi et al., 2011).

The working principle of AFM is based on the force generated between a tip and the sample surface. Due to the attractive and repulsive interactions occurred between tip and sample move tip towards or away from the surface generating a signal that is used to create an image of sample topography.

Three AFM modes have appeared for special purpose; contact mode, tapping mode, an non-contact mode. Contact mode is one of the most common method operations of AFM. In this mode measuring topography occurs by sliding the probes tip across the surface. When a raster scan drags the tip over the sample, some sort of detection apparatus measures the vertical deflection of the cantilever, which indicates the local sample height.

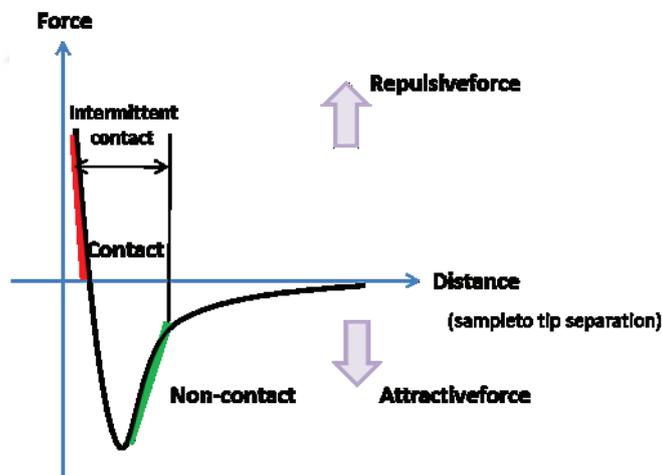


Figure 2.12. Force distance curve of AFM.

As shown in Figure 2.12, the repulsive region of the curve lies above the x-axis and attractive region is below the axis. One of the drawbacks of remaining in the contact with the sample is that there exist large lateral forces on the sample as the drip is dragged over specimen.

Tapping mode is the next common mode used in AFM. Topography is obtained

by lightly tapping the surface with an oscillating probe tip and eliminates shear forces. When operated in air or other gases the cantilever is oscillated at its resonant frequency (generally 100 kHz) and positioned above the surface so that it only taps the surface for a very small fraction of its oscillation period. This still contact with the sample in the sense defined earlier but the very short time over which this contact occurs that lateral forces are dramatically reduced as the tip scans over the surface. When imaging poorly immobilized or soft samples, tapping mode may be a far better choice than contact mode. This mode images show no surface alteration and better resolution.

Other methods of obtaining image are also possible with tapping mode. In constant force mode, the feedback loops adjust so that the amplitude of the cantilever oscillation remains constant. An image can formed from this amplitude signals, as there will be small variations in this oscillation amplitude due to the control electronics not responding instantaneously to change on the specimen surface.

Non-contact operation is another method which may be employed when imaging by AFM. Topography is measured by sensing Vander Waals attraction between the surface and probe tip. It provides lower resolution. The cantilever must be oscillated above the surface of the sample at such a distance that we are no longer in repulsive regime of the intermolecular force curve. This is a very difficult mode to operate in ambient conditions with the AFM. The thin layer of water contamination which exists on the surface will invariably form a small capillary bridge between the tip and the sample and cause the tip to "jump to contact". Even under liquids and vacuum, "jump to contact" is extremely likely and imaging is most probably occurring using tapping mode. Phase imaging maps surface composition based on differences in local mechanical or adhesive properties of the sample.

In so many studies AFM is used to investigate film and graphene surface. One example is the study of Zhang group. They deposited polycrystalline Ni film with the thickness of 500 nm on SiO₂/Si substrate by e-beam evaporation. Then, they compare AFM topography images of single crystal Ni (111) and deposited polycrystalline Ni thin film. While the roughness of Ni (111) substrate is measured as 5.3 nm, polycrystalline Ni film has the roughness of 36.3 nm (Zhang et al., 2010). In the same study, the thickness of grown graphene film transferred from Ni (111) substrate is measured. Transferred graphene film's topography image and its height profile are shown in Figure 2.13. According to height profile thickness is measured as 0.93 nm which is considered to be one or two layers due to the roughness of SiO₂/Si substrate.

Again in another study, Reina *et al.* used AFM to compare annealed polycrys-

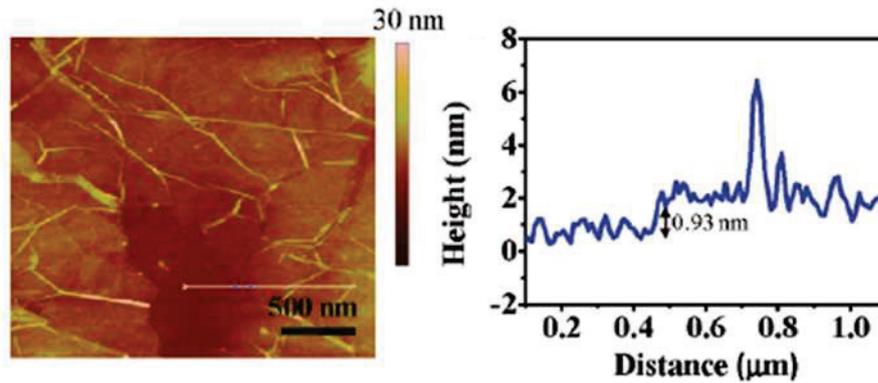


Figure 2.13. (a) AFM image and (b) AFM height profile of transferred graphene film. Reprinted with permission from (Source: Zhang et al. (2010)). Copyright 2010 American Chemical Society.

talline Ni thin film surface before and after the CVD graphene growth (Reina et al., 2008). The AFM images are shown in Figure 2.14.

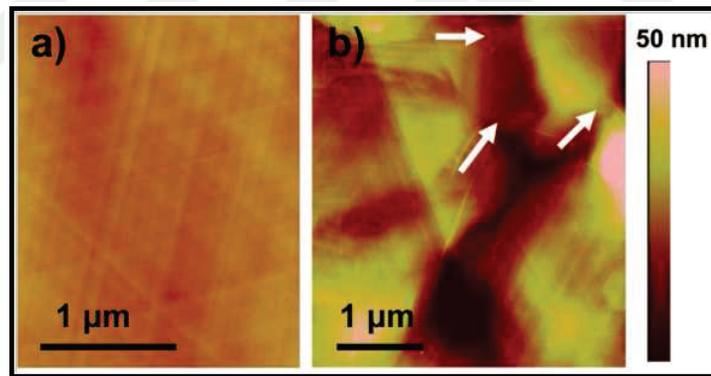


Figure 2.14. AFM topography images of annealed polycrystalline Ni thin film (a) before and (b) after the graphene growth Reprinted with permission from (Source: Reina et al. (2008)). Copyright 2008 American Chemical Society.

Additionally, height profile taken from two different regions showed that grown graphene films are between 1-8 layers that also confirmed by TEM measurements. AFM images and measured height profile from the regions signed in topography image are shown in Figure 2.15.

AFM images of graphene films transferred on to SiO₂/Si substrate from Cu was investigated by Srivastava *et al.* and Bae *et al.* The transfer process of graphene on

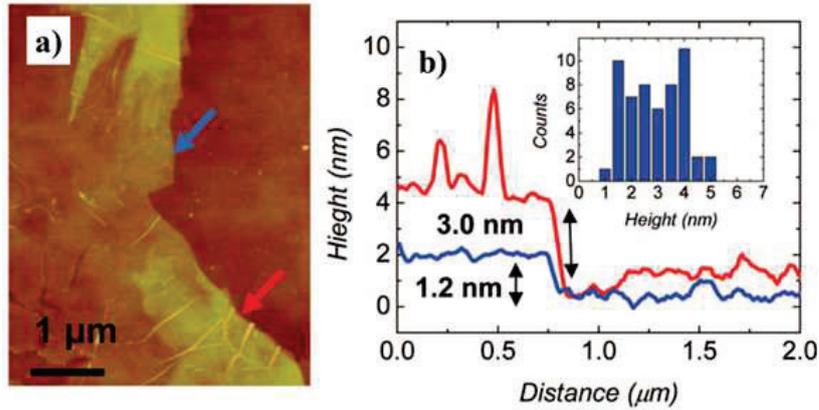


Figure 2.15. (a) AFM topography and (b) height profile of transferred graphene film Reprinted with permission from (Source: Reina et al. (2008)). Copyright 2008 American Chemical Society.

insulating layer leads to formation of cracks and wrinkles on graphene surface. As shown in Figure 2.16, the height profile of the graphene taken by using AFM gives information about the number of layers (Bae et al., 2010), (Srivastava et al., 2010).

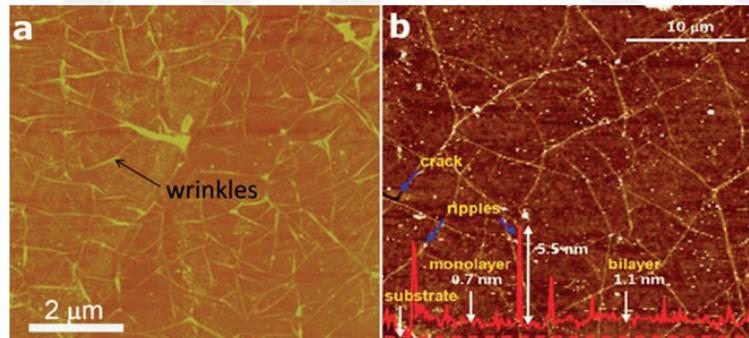


Figure 2.16. (a) AFM image of single layered graphene on SiO₂/Si. Reprinted with permission from (Source:(Srivastava et al., 2010)). Copyright 2010 American Chemical Society. (b) AFM image and height profile of transferred graphene film. Reprinted with permission from (Source: Bae et al. (2010)). Copyright 2010 American Chemical Society

2.7.3. Kelvin Probe Force Microscopy (KPFM)

KPFM was derived from existing AFM and measures the work function in conducting materials or the surface potential in nonconducting materials on nanometer scales. KPFM has been used to provide an information about charge distribution and surface potential of electrochemically etched surfaces, semiconductors, lipid membranes.

The Kelvin method measures the work function, that is the work required to remove the valence electron from an atom, in metals and the surface potential in nonmetals to within 0.1mV. Suppose that, two metals have two different Fermi levels (the energy of the highest occupied quantum state in a system of fermions). When the external contact is occurred between these metals, electron transfer starts to equalize their Fermi levels. This electron flow creates the contact potential difference (CPD) between the two surfaces, where they are oppositely and equally charged. If the bias voltage is applied, the flow of the electrons can be stopped. The Kelvin Method works by applying an external potential to balance CPD. The applied external voltage amount is equal to the work function or surface potentials of the sample.

In literature, KPFM has been used in interlayer screening, surface potential, work function and local voltage drop measurements of different structured graphene layers (Lee et al., 2009), (Yu et al., 2009), (Yan et al., 2011), (Liscio et al., 2011).

In the study of Lee *et al.*, KPFM was used to report interlayer screening effect of graphene by using a gate device configuration (Lee et al., 2009). They showed that if the number of layers increases, the exponential decrease occurs in surface potential. Also the work function relation of graphene layers was calculated in the same study. Figure 2.17 shows their gated graphene structure.

Functionalized graphene sheets (FGSs) were investigated in the study of Yan *et al.* They determined the intrinsic conductivity of FGSs, the charge transport mechanism between them and metal contacts and also the correlations between electrical properties and topographic properties. Kelvin Voltage maps of FGSs were presented taken with 3 different external bias voltage values and work function differences between the tip and the sample were represented with the voltages (Figure 2.18).

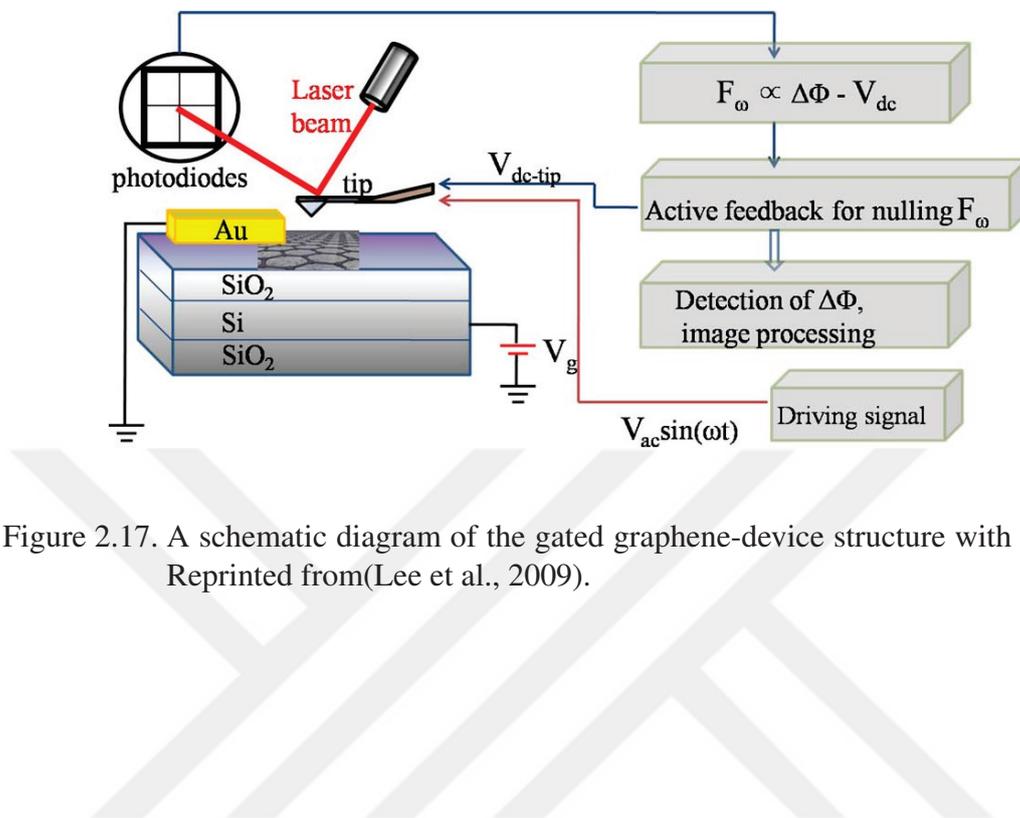


Figure 2.17. A schematic diagram of the gated graphene-device structure with KPFM. Reprinted from(Lee et al., 2009).

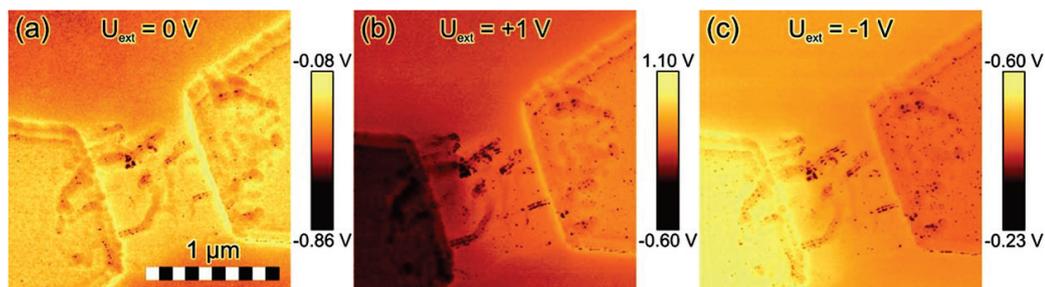


Figure 2.18. Kelvin voltage maps with external bias (a) 0 V, (b) +1.0 V, and (c) -1.0 V. The left contact was connected to the ground for all the measurements. The voltages represent the work function difference between the AFM tip and the scanned object. Reprinted with permission from (Source: Yan et al. (2011)). Copyright 2011 American Chemical Society.

2.7.4. Scanning Electron Microscopy (SEM)

Scanning Electron Microscopy (SEM) is a tool that uses electrons instead of light in imaging sample surface and characteristics. It has many advantages when compared to traditional microscopes. Large electrical field depth allows more detailed investigation of specimens at the same time. It has much higher resolution, thus samples can be magnified at much higher levels. Electrons are oriented by electromagnets instead of lenses, therefore, users have much control in the degree of magnification.

In SEM, electrons are generated by an electron gun that is placed at the top of the microscope. The electron beam vertically directed through electromagnetic fields and lenses in a vacuum environment. Electrons and X-rays ejected from the sample after the beam-sample interaction. Emitted X-rays, backscattered electrons and secondary electrons are collected by detectors and converted into signal. In this way final images were generated. Schematic diagram of SEM is shown in Figure 2.19.

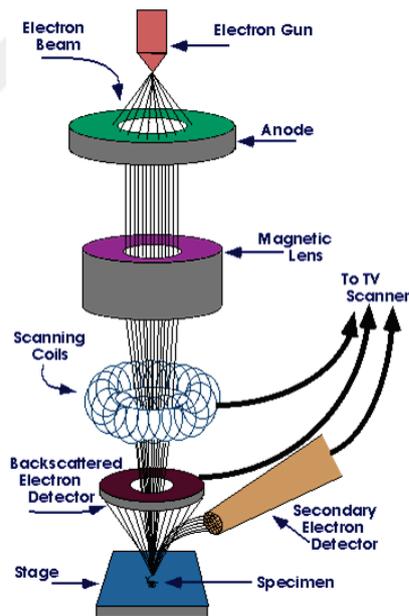


Figure 2.19. Schematic diagram of SEM.

2.7.5. Raman Spectroscopy

Raman spectroscopy is an effective and non-destructive tool for characterizing semiconductors. It is mostly used for getting information about crystal quality, alloy composition, carrier concentration, scattering time and strain in semiconductors.

Raman spectroscopy is based on the inelastic scattering of light by elementary excitations. Raman scattering occurs due to the interaction of incident light with material which leads to a creation of a phonon or an annihilation.

Ferrari *et al.* showed that in the Bernal AB stacking case, second order G' feature that is appeared in Raman spectra can be used to get information about the number of layers in a graphene sample (Ferrari et al., 2006). G' feature is originated from the double resonance (DR) Raman process (Narula and Reich, 2008), (Saito et al., 2001) that electrons and phonons are linked in graphene dispersion relation (Ferrari et al., 2006), (Gupta et al., 2006), (Graf et al., 2007), (Mafra et al., 2007), (Malard et al., 2007).

In monolayer graphene, due to the DR process, electron-phonon scattering is occurred along the $K\Gamma K'$ direction. A Raman spectrum of a monolayer graphene taken with a laser energy of 2.41 eV with G and G' bands is shown in Figure 2.6. At room temperature G' band exhibits a single Lorentzian feature with a full width at half maximum (FWHM) value of $\sim 24 \text{ cm}^{-1}$. In the Raman spectrum, when compared to G -band, G' has higher intensity and this large relative intensity of G' can be explained by triple resonance (TR) process as shown in Figure 2.20. This spectrum is unique for all sp^2 carbon atoms because of the linear energy dispersion relation (Malard et al., 2009).

In bilayer graphene with Bernal AB layer stacking, electronic and phonon bands split into two components with special symmetries. Due to the motion of carbon atoms in the two layers, one of the component is in phase and the other component is out of phase with respect to each other. Bilayer graphene has a parabolic $E(k)$ dispersion relation and show k^2 dependence near $k = 0$ with having two valance and two conduction bands (Neto et al., 2009), (McClure, 1957), (Slonczewski and Weiss, 1958), (Partoens and Peeters, 2006).

Electronic structure of bilayer graphene is shown in Figure 2.21 where the upper(lower) and lower(upper) branches of the valance(conduction) band are labeled as π_1 (π_1^*) and π_2 (π_2^*), respectively (Neto et al., 2009). The major steps of the DR process occur along the T line (ΓK) along which the π_2 and π_1^* bands belong to the T_1 totally symmetric irreducible representation, while the π_1 and π_2^* have odd T_2 symmetry (Dresselhaus et al., 2007).

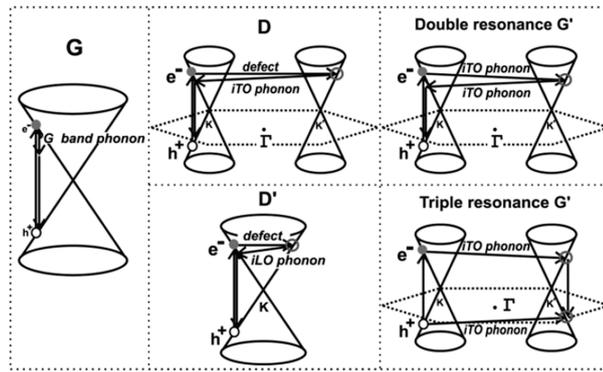


Figure 2.20. (Left) First-order G-band process and (Center) one-phonon second-order DR process for the D-band (intervalley process) (top) and for the D' -band (intravalley process) (bottom) and (Right) two-phonon second-order resonance Raman spectral processes (top) for the double resonance G' process, and (bottom) for the triple resonance G' band process (TR) for monolayer graphene (Dresselhaus et al., 2005). For one-phonon, second-order transitions, one of the two scattering events is an elastic scattering event. Resonance points are shown as open circles near the K point (left) and the K' point (right). Reprinted with permission from (Source: Malard et al. (2009)). Copyright 2009 American Chemical Society.

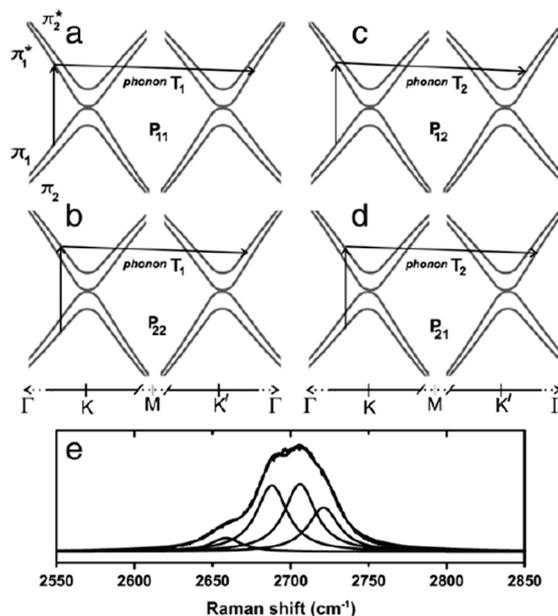


Figure 2.21. Schematic view of the electron dispersion of bilayer (2-LG) graphene and its measured G' band. Reprinted with permission from (Source: Malard et al. (2009)). Copyright 2009 American Chemical Society.

As it is shown in figure 2.21 (a-d), four different P_{ij} processes were provided where i (j) represents the electron scattered from (to) each conduction band $\pi^*_{i(j)}$. While the P_{11} and P_{22} processes come from an iTO phonon, with $S T_1$ symmetry, P_{12} and P_{21} processes arise from an iTO phonon with $AS T_2$ symmetry. These four scattering processes involve four Raman peaks in the G' band. Raman spectra of a AB stacked bilayer graphene is shown Figure 2.21(e) with fitted G' band by four Lorentzians each one having FWHM value of $\sim 24 \text{ cm}^{-1}$ (Malard et al., 2007).

The G' band continues to evolve with the number of graphene layers until the final material bulk graphite is achieved. For HOPG the G' band can be considered as two different peaks (see Fig.2.22(e)). The Raman spectra of G' band for (a) monolayer, (b) bilayer, (c) trilayer, (d) four layer graphene and (e) HOPG are compared in Figure 2.22. In figure, the evolution of the Raman spectra with the number of layers is significant. After 4-layer, Raman spectra of G' band starts to take the form of HOPG band where the 4-LG is analyzed by 3 peaks like HOPG.

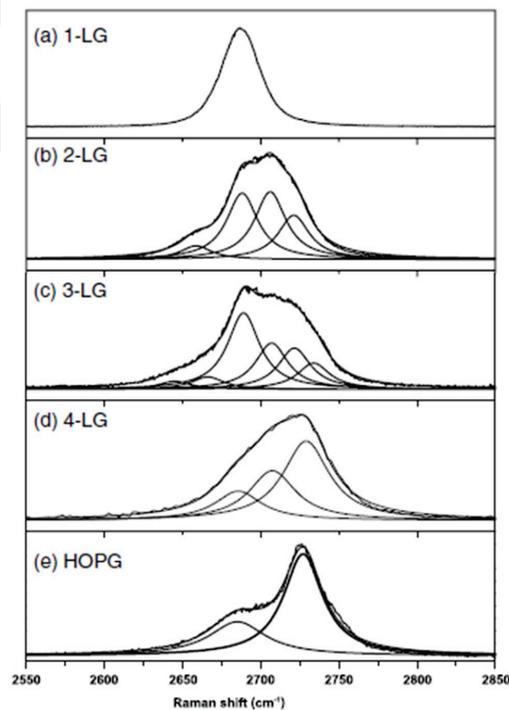


Figure 2.22. The measured G' Raman band. Reprinted with permission from (Source: Malard et al. (2009)). Copyright 2009 American Chemical Society.

2.8. Sensing Applications of Graphene

Gas adsorption, storage and separation in carbon based materials are based on physisorption on surface by electrostatic and dispersion interactions such as VdW interactions. Surface characteristics of the adsorbed molecule and structural properties (size and shape with its polarizability, magnetic susceptibility, permanent dipole moment and quadrupole moment) of target molecule affect the strength of the interaction. For example, an adsorbent with a high specific surface area is a good candidate for adsorption of a molecule with high polarizability but no polarity. Similarly, adsorbents with highly polarized surfaces are good for adsorbate molecules with high dipole moments (Li et al., 2009), (Yang, 2003). Generally, adsorption of H₂ and N₂ gas molecules on carbon nanostructures are relatively low where CO, CH₄ and CO₂ intermediate and NH₃, H₂S and H₂O are relatively high. Therefore, for increase the gas adsorption surface modifications such as doping, functionalization and improving pore structure and specific surface area of nanocarbons are important.

2.8.1. Gas Sensors Based on Pristine Graphene

Due to its 2D structure, gas molecule adsorption affects the electron transport mechanism of graphene and makes it highly sensitive. Local carrier concentration of the graphene changes with the adsorbent characteristics even if it has electron accepting or losing characteristics (Schedin et al., 2007). Pristine graphene has high electrical conductivity and low intrinsic noise, thus a few charge carrier adsorbance leads to significant change in charge carrier density and electrical conductivity gives detectable reaction (Varghese et al., 2015).

In the study Schedin *et al.* gas sensing properties of graphene were investigated for the first time by constructing micrometer-sized sensor of mechanically exfoliated few-layer pristine graphene (Schedin et al., 2007). Under high vacuum environment this sensor had the ability of sensing even a single molecule of nitrogen dioxide (NO₂). They also explained that if the hole concentration increases by electron acceptors, the measured resistivity decreases and if the electron concentration increases, the measured resistivity also increases. Therefore, when the sensor is exposed to electron acceptors such as NO₂, H₂O; resistivity decreases, and when the sensor is exposed to CO, NH₃; resistivity increases (Figure 2.23).

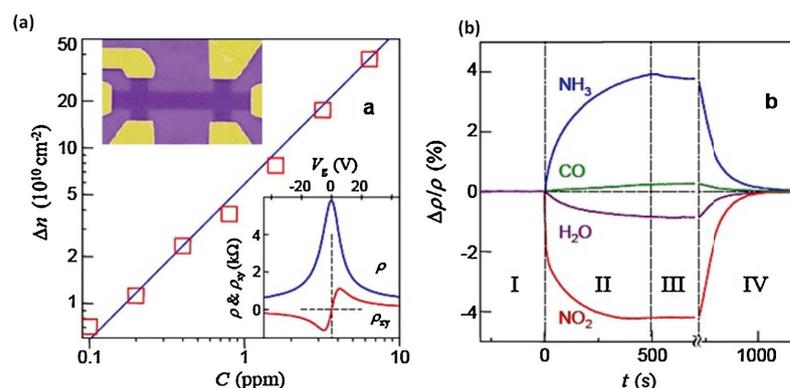


Figure 2.23. (a) Chemically induced charge carrier concentration in SLG versus NO_2 concentration; Upper inset: SEM of the sensor device; hall bar width is $1 \mu\text{m}$; Lower inset: Graphene device characteristics under applied electric field. (b) Resistivity (ρ) change under various gas exposures with 1 ppm flow amount. Region I: the sensor response in vacuum; II: exposure to a 5-L volume of a diluted chemical; III: evacuation; and IV: annealing at 150° . Reprinted with permission from (Source: Schedin et al. (2007)). Copyright 2007 American Chemical Society.

In the study of Wehling *et al.* it was shown that DOS of graphene is suitable for chemical sensing and their results showed correlation with the Schedin *et al.* (Wehling et al., 2008). First-principles simulations of H_2O , NH_3 , NO_2 and NO gas molecules based on Density Functional Theory calculations also showed that they are physically adsorbed on pristine graphene (Leenaerts et al., 2008).

Hydrogen adsorption kinetics onto various graphene flakes were analyzed by Ganji *et al.* They used non-local vdW corrected DFT and calculated the adsorption energy for physisorbed H_2 on coronene surface (Ganji et al., 2015). Their results showed good agreement with experimental results. Lee *et al.* studied DFT and second-order Møller-Plesset (MP2) calculations of both physisorbed and chemisorbed CO_2 on graphene and clarified the adsorption energies which are also in good agreement with experimental and previous theoretical findings (Lee and Kim, 2013).

Ko *et al.* used 3.5-5 nm thick mechanically exfoliated graphene layers on SiO_2/Si substrate to construct a NO_2 gas sensor (Fig. 2.24) (Ko et al., 2010). Metal contacts were patterned by e-beam lithography technique. Their sensors gave reproducible and reversible results with fast response, high selectivity and high sensitivity under 100 ppm NO_2 exposure at room temperature.

Yoon *et al.* compared the response of HOPG flakes under CO_2 , NO_2 and NH_3

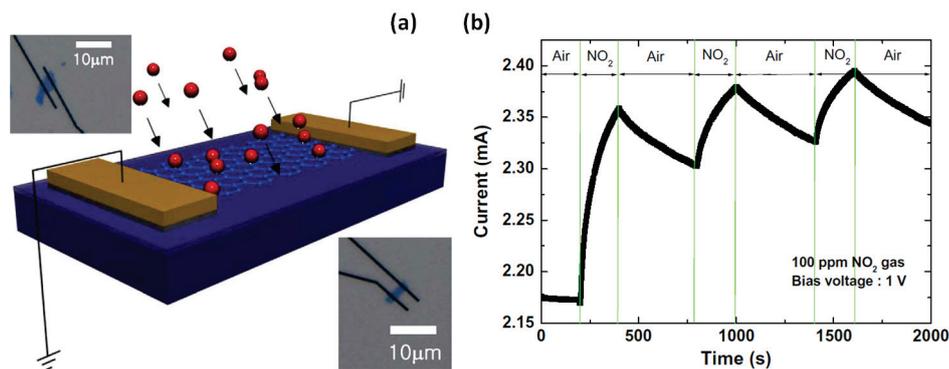


Figure 2.24. (a) Graphene based NO₂ gas sensor diagram. Upper and Bottom insets: Optical images. (b) Sensor response under periodic Air - NO₂ gas alteration. Reprinted with permission from (Source: Ko et al. (2010)). Copyright 2010 American Chemical Society.

gas exposures (Yoon et al., 2011). While the response time and recovery time of the sensor under CO₂ exposure was measured as 8 s and 10 s, respectively, high temperature annealing at high vacuum was required for desorption of NO₂ and NH₃ gas molecules.

Table 2.1. Graphene Detection Limit (DL) of NO, NO₂, NH₃, N₂O, O₂, SO₂, CO₂ and H₂O. Reprinted from (Chen et al., 2012).

Gas	C_{min}	Graphene DL (ppt)	CNTs DL (ppt)
NO	10	0.158	0.59
NO ₂	40	2.06	1.51
NH ₃	200	33.2	27.8
N ₂ O	200	103	-
O ₂	200	38.8	-
SO ₂	200	67.4	-
CO ₂	200	136	-
H ₂ O	200	103	-

CVD grown graphene based sensor had the ability of detecting low concentrations with the limit of part-per-quadrillion (ppq) range at room temperature conditions by in situ cleaning of graphene under UV light (Chen et al., 2012) (Figure 2.25). Their results showed that UV light exposed pristine graphene sensors have ~ 3 times better sensitivity than CNT based gas sensors as indicated in Table 2.1. In another study different vapors of chemicals such as tetrahydrofuran, methanol, acetonitrile and chloroform were examined using pristine graphene transistor by low frequency noise spectrum measurements. While some chemical vapors showed different characteristic frequencies in the spectrum, some

vapors introduce change only in resistance measurements (Rumyantsev et al., 2012).

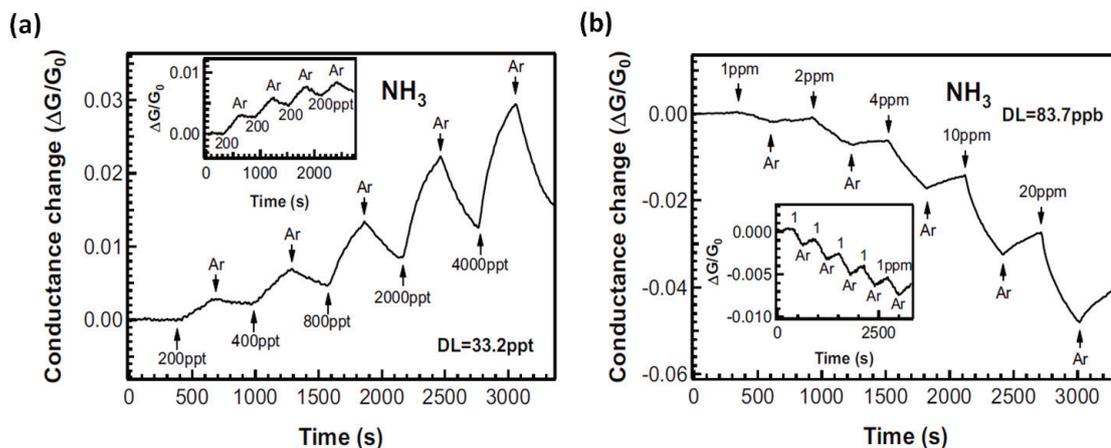


Figure 2.25. (a) Response of NH_3 sensor under in situ UV light illumination. The inset shows the reproducibility of sensor response at 200 ppt of NH_3 exposure. (b) Response of NH_3 sensor without UV light illumination. Reprinted from (Chen et al., 2012).

CO_2 and LPG gas sensing properties of electrochemically exfoliated few-layer graphene were studied by Nemade *et al.* at room temperature. Sensor sensitivity was measured as 3.83 for CO_2 and 0.92 for LPG with the response times of 11 sec and 5 sec, respectively (Nemade and Waghuley, 2013).

Kumar *et al.* developed a resistive gas sensor by transferring CVD grown graphene on a smooth paper. Sensor response under NO_2 exposure was found as $118\% \text{ ppm}^{(-1)}$ and it was improved by a factor of 2.5 by 10 min applied UV exposure. The low detection limit of the sensor was measured as 300 parts per trillion (ppt) (Kumar et al., 2015).

A graphene/n-Si Schottky junction that fabricated by mechanical deposition of natural HOPG was tested under H_2S gas exposures at different temperatures. When compared to previously reported H_2S sensors, this Schottky diode based sensor showed better selectivity, reproducibility, easy adsorption and desorption (Fattah and Khatami, 2014).

2.8.2. Gas Sensors Based on Defective and Functionalized Graphene

Currently, graphene gas detectors are also extremely sensitive; they have a minor competitive edge over existing sensors. Such graphene detectors can be produced

so cheaply that they can be used in suitable applications. Functionalization and make graphene more defective by etching process might improve the selectivity of graphene sensors, especially for bio-sensing. Major advantage of graphene sensors is their ability in functionalization. With a single device, multidimensional measurements such as strain, gas environment, pressure and magnetic field can be achieved.

2.8.2.1. Chemically Modified Graphene Based Sensors

The ability of graphene to undergo physical and chemical changes makes it easily modified and functionalized material (Varghese et al., 2015). Therefore, atomic doping, molecular impregnation and chemical functionalization studies of graphene attract great attention. Graphene has symmetric band structure which makes it suitable for chemical modification. Chemical modification leads to tuning surface and chemical features of graphene.

Doping graphene by heteroatoms such as N₂, S, B, Si, etc. tunes the electronic properties of graphene by altering band gap structure (Usachov et al., 2011), (Kong et al., 2014), (Liu et al., 2011). Defect formation in graphene basal plane also changes the physical and chemical properties and enhances the gas sensing performance (Terrones et al., 2012), (Su and Shieh, 2014), (Yoo et al., 2014), (Allen et al., 2009), (Cui et al., 2013), (Huang et al., 2012), (Jeong et al., 2010).

In the study of Niu *et al.* graphene nanosheets were doped with phosphorus (P-GNS) and constructed an improved NH₃ sensor (Figure 2.26). When compared to thermally reduced graphene, P-GNS based sensors showed better response, shorter recovery and response time at room temperature (Niu et al., 2014).

One of the other method that was used in the improvement of the graphene sheets based NO₂ gas sensors is the co-doping with N₂ and silica atoms. N and Si-containing GO-ionic liquid composites are annealed at high temperatures and they incorporated in graphene network. While the N atoms act as adsorption sites for NO₂ gas molecules, Si atoms modify the electronic structure of graphene (Niu et al., 2013).

There are also studies that focus on the modification of reduced graphene oxide (RGO) to improve their gas sensing abilities. Recently, cysteamine hydrochloride (CH) modified RGO films were fabricated as flexible NO₂ gas sensors as shown in Figure 2.27 (Su and Shieh, 2014). In another study reduction of GO by tannic acid lead to n-type doping which shows electron donating behavior under NH₃ exposure (Yoo et al., 2014).

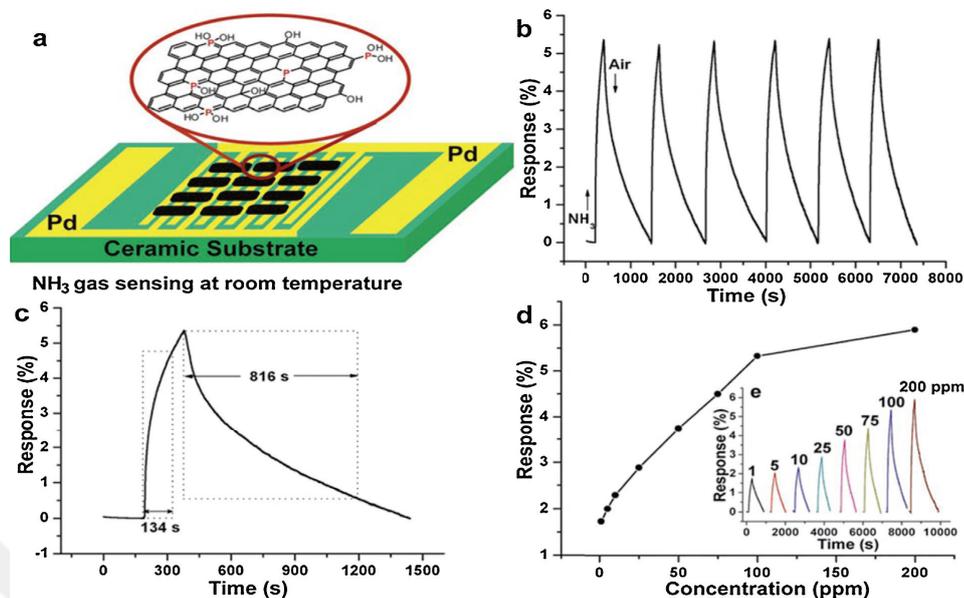


Figure 2.26. (a) P-GNSs based NH_3 sensor structure, (b) the response of P-GNS-400 at 100 ppm NH_3 exposure, (c) response and recovery time plot, (d) and (e) are the response values of P-GNS-400 under various NH_3 concentrations. Reprinted with permission from (Source: Niu et al. (2014)). Copyright 2014 American Chemical Society.

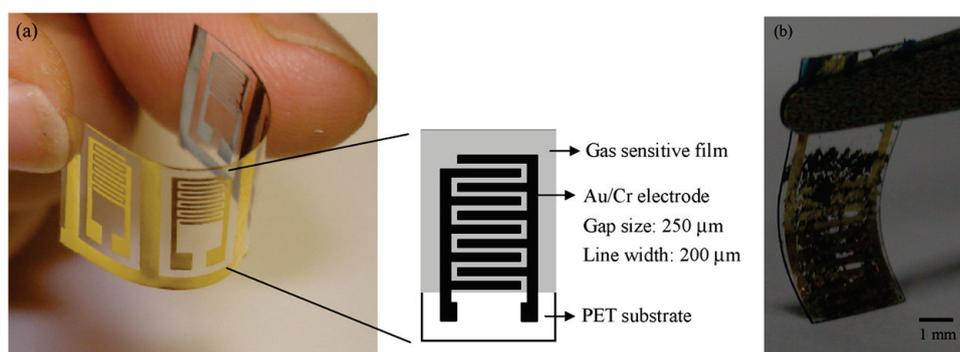


Figure 2.27. (a) Structure of flexible gas sensor; (b) Photograph of bent gas sensor based on RGO film anchored on a PET substrate. Reprinted with permission from (Source: Su and Shieh (2014)). Copyright 2014 American Chemical Society.

2.8.2.2. Graphene/nanoparticle Hybrid Based Sensors

Graphene when used as gas sensor shows high affinity by inducing significant change in its electrical conductance. However, the main deficiency of these graphene based sensors is their poor selectivity under various gas species. For example; they cannot distinguish different gases, cannot determine the type of the gases and their concentration (Allen et al., 2009). In that manner, graphene and RGO based hybrid nanostructures especially functionalized with metal and metaloxide nanoparticles show promising results in enhancing sensor sensitivity and selectivity (Varghese et al., 2015).

Nobel metal nanoparticles (such as Pt, Pd and Au) decorated graphene based gas sensors were studied by Kaniyoor *et al.* When compared to Pt decorated MWCNT based sensors, Pt decorated graphene sensor showed better response time under the 4% vol of H₂ in air at room temperature (Kaniyoor et al., 2009).

Decorating CVD grown graphene with metal nanoparticles were discussed in the study of Gutes *et al.*. By using Cu as reducing agent; gold, palladium, platinum and silver nanoparticles were deposited. After the transfer of the decorated graphene film onto a transducer, measurements were carried on using two comb-shaped gold electrodes. The sensing device showed fast response to gas molecules; however its slow desorption due to strong S-Au bonding makes it disfavored (Gutés et al., 2012).

Chung *et al.* compared the sensing characteristics of PG and Pd decorated CVD-grown graphene under H₂ gas exposure (Chung et al., 2012). While the Pd decorated sensor showed remarkable resistance change, no detectable response was observed in the case of PG based sensor. At room temperature, the sensing response of 33%.

Palladium nanoparticle functionalized graphene nanoribbons were fabricated by Pak *et al.* for H₂ gas sensing (Pak et al., 2014). By using periodically arrayed graphene nanoribbons they achieved rapid response of 90% within 60 s under 1000 ppm H₂ gas flow and 80% recovery was observed in N₂ environment under 1000 ppm H₂ was measured for 3 nm thick Pd layer deposited graphene sensors.

While Graphene and RGO based hybrid nanostructures enhance sensitivity, they also show good selectivity. Recently, there are also studies that focused on the functionalization of graphene with semiconducting metal oxide nanoparticles, such as SnO₂ (Mao et al., 2012), (Zhang et al., 2014), CuO₂ (Zhou et al., 2013), TiO₂ (Esfandiar et al., 2012), ZnO (Liu et al., 2014), (Singh et al., 2012) and their gas sensing applications.

2.8.2.3. Graphene/polymer Hybrid Based Sensors

Previous studies of polyaniline functionalized CNTs exhibited better performance in gas sensing performance when compared to pristine CNTs (Mangu et al., 2011), (Srivastava et al., 2010). Based on the improvement in CNTs, graphene and RGO were also functionalized with polymers and the benefits of the two material were combined. The reported graphene/RGO based polymer hybrids had enhanced sensing properties when compared to bare graphene/RGO (Huang et al., 2012), (Parmar et al., 2013), (Huang et al., 2013), (Ye et al., 2014), (Mishra et al., 2014)). Similarly, Parmer *et al.* investigated toluene sensing behaviors of PANI and graphene/polyaniline nanocomposite (C-PANI) films at various temperatures (Parmar et al., 2013). While the PANI films showed better sensor response, the overall sensing performance in terms of its response and recovery time of C-PANI is more favorable.

A highly sensitive and selective H₂ gas sensor was achieved by PMMA coated Pd nanoparticle (NP) functionalized single layer graphene hybrid (Hong et al., 2015). Pd NPs were deposited on CVD grown graphene by graphene-buffered galvanic displacement reaction between Cu and Pd ions and then PMMA membrane was coated by spin coating method. Due to the selective filtration of H₂ by polymer coating, sensor didn't showed any response under CO, NO₂ or CH₄ gas exposures and it showed 66.7% response within 2.81 min under 2% H₂ gas exposure. Recovery time was also measured as 5.52 min.

NH₃ sensing properties were investigated with graphene poly(3,4-ethylenedioxy thiophene): poly(styrene sul-fonate) (PEDOT:PSS) composite film by Seekaew *et al.* (Seekaew et al., 2014). Graphene dispersed conducting PEDOT:PSS solution ink was printed onto a transparent substrate with predeposited electrodes. Sensor showed high sensitivity and selectivity to NH₃ gas due to increased specific surface area of graphene and enhanced interaction of composite film with NH₃ molecules.

Various polymers were also used to construct graphene/ polymer based gas sensor for evaluating the sensitivity towards different gases (Zhou et al., 2014), (Rañola et al., 2015), (Lin et al., 2013), (Jang et al., 2013). Obtained results showed that graphene/ polymer nanohybrids are more suitable in gas sensing rather than bare graphene or bare polymer films.

2.8.2.4. Self-Assembled Monolayer Modified Graphene Based Sensors

Self-assembled monolayers (SAMs) are well-oriented molecular structures formed by the adsorption of an active surfactant on a substrate surface. As a result of intramolecular, intermolecular and interfacial forces, ordered 2D and 3D polymolecular structures can be obtained. Atoms and molecules are bounded to surface in two ways; physisorption that is corresponding to physical adsorption and chemisorptions that is corresponding to chemical adsorption.

Physisorption is the adsorption of a thin layer of molecules to a surface without the formation of a chemical bond. The binding is resulted from hard core repulsions and the interplay of weak attractive forces such as vdW and electrostatic forces which exist over long ranges. Physisorption is a reversible process and the adhesion involved can also take place in multilayer. On the other hand, chemisorption is the adsorption of molecules to a surface through the formation of a chemical bond. SAMs are formed spontaneously upon the immersion of a substrate into a solution containing an active surfactant molecule in organic solvent. These molecules consist of three parts; head group enhances chemisorption to the substrate and binds the molecule to the substrate surface strongly, chain or backbone takes place in the packaging density of the molecules and specific functional tail group constitutes the other surface of the film and modifies the bulk surface properties.

Lee and his group reported a study of "Modification of Electronic Properties of Graphene with Self-Assembled Monolayers" in 2010 (Lee et al., 2010). They synthesized stable self-assembled monolayers of fluoroalkyl silanes at the surface of graphite and graphene and observed that the mechanism of SAM formation on graphene is based on a defect-mediated nucleation, followed by a lateral 2D polymerization that eventually leads to a complete monolayer coverage by a cross-linked and robust 2D siloxane network. This distinct morphology of SAM nucleation suggests that it can be used as a simple technique for visualization or electronic passivation of graphene edges and defects, as well as for complete SAM coverages. They speculate that free silanol groups (Si-OH) at the SAM-graphene interface might be responsible for a strong protonic doping of the surface due to high acidity of the protons.

CHAPTER 3

MATERIALS AND METHODS

3.1. Materials

N-type Silicon wafers with $\langle 100 \rangle$ orientations were purchased from Si-Mat Company, Germany. S1318 Photoresist (PR) was also purchased from Microposit Company.

Cu foils with 25 μm thickness and 99.8% purity were purchased from Alfa Easier Company.

3.2. Silicon Wafer Oxidation

Silicon wafers were cleaned in acetone and in deionized water, respectively for 15 min and dried with N_2 gas stream. Then, wafers were placed into furnace tube for wet oxidation. System was heated up to 850 $^\circ\text{C}$ with 28 $^\circ\text{C}/\text{min}$ ramp under Argon gas flow. At 850 $^\circ\text{C}$, 1 slm O_2 gas and water stream was flown into furnace tube. At 900 $^\circ\text{C}$ Ar gas was stopped and O_2 flow was increased to 2 slm at 1000 $^\circ\text{C}$. Oxidation was carried on for one hour and heating process was stopped and Ar gas started for cooling. Thickness of the oxide layer was measured as nearly 300 nm as shown in Figure 3.1.



Figure 3.1. SiO_2/Si substrates.

3.3. Cu Foil Annealing

Firstly, to specify the appropriate temperature zone where the growth will be occurred, that is the zone where temperature is the highest, we annealed the Cu foils at different temperatures under 100 sccm Ar and 100 sccm H₂ gas mixture flow. We found that Cu foil was melted at 1080 °C and the appropriate zone was found as the thermocouple region as shown in Figure 3.2.



Figure 3.2. Cu foil annealed at 1080 °C.

Then, the temperature at where foils will be annealed but not melted was investigated. Cu foils were annealed at 1075 °C, 1073 °C and 1070 °C. The highest temperature that foil annealed but not melted was found as 1073 °C. Cu foils that were annealed at various temperatures are shown in Figure 3.3.

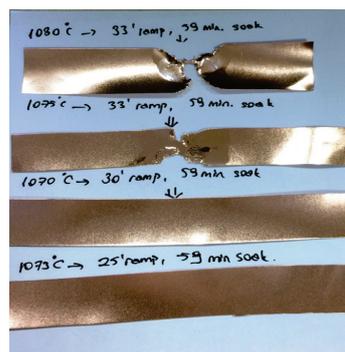


Figure 3.3. Cu foils annealed at different temperatures.

3.4. Graphene Growth by CVD Technique

In order to find the appropriate growth parameter, Cu foils were annealed at different temperatures under Argon and H₂ gas mixture flow. Methane gas flow amount and flow time affects the layer number and the quality of the grown graphene. Therefore, different CH₄ flow amounts and growth time parameters were also investigated. Table 3.1 includes all applied growth parameters.

Table 3.1. Annealing, Growth and Gas Flow Parameters of Graphene Samples.

Sample	Ramp Time (min)	Annealing Growth Temperature (°C)	Annealing Time (min)	Growth Time (min)	Ar Flow (sccm)	H ₂ Flow (sccm)	CH ₄ Flow (sccm)
GRP309	33	1000	59	15	-	10	10
GRP310	33	1000	59	15	-	20	5
GRP311	33	1000	59	5	-	20	5
GRP312	33	1000	59	3	-	20	5
GRP313	33	1000	59	3	-	20	5
GRP314	33	1000	59	2	-	20	5
GRP315	33	1000	59	2	-	30	5
GRP316	33	1000	59	5	200	20	5
GRP317	33	1000	59	5	200	20	5
GRP318	33	1000	59	3	200	20	5
GRP319	33	1000	59	2	200	20	5
GRP320	33	1073	30	3	200	20	5
GRP321	33	1073	30	3	200	20	5
GRP322	33	1073	30	3	200	20	5
GRP323	40	1070	30	5	200	20	5
GRP324	33	1073	30	3	200	20	3
GRP325	33	1073	30	3	200	20	5
GRP326	33	1073	30	3	200	20	5
GRP327	33	1075	59	3	200	20	5
GRP328	33	1073	59	3	200	20	5

The ideal monolayer graphene growth temperature was achieved at 1073 °C under 5 sccm Methane (CH₄), 20 sccm Hydrogen (H₂) and 200 sccm Argon (Ar) gas flows on commercial Cu foils as mentioned at previous report. Cu foils were annealed at the same temperature for 59 min under 20 sccm H₂ and 200 sccm Ar gas flows. The graph shown in Figure 3.4 presents the graphene growth process with temperature and time interval values. Cooling process was carried under 20 sccm H₂ and 200 sccm Ar gas flows.

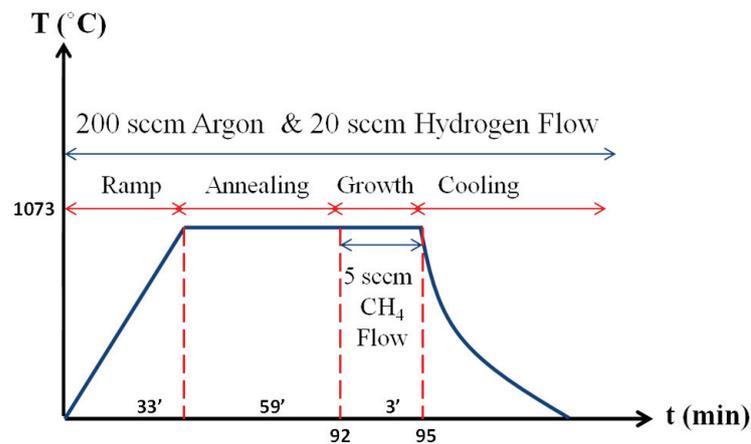


Figure 3.4. Standard Graphene Growth Process

3.5. Anisotropic Hydrogen Etching of Graphene with CVD

Zhang *et al.* showed that anisotropic hydrogen etching of chemical vapor deposited graphene is possible by applying reverse reaction of growth conditions (Zhang et al., 2011). Clean and high efficient anisotropic etching was obtained at 800 °C and 500 m Torr with 30 sccm H₂ gas flow. In addition, 80% of measured angles at etched graphene edges were found as 120°, and the etched edges were confirmed to be along the $\langle 11\bar{2}0 \rangle$ zigzag direction.

Similarly, Geng *et al.* showed that by varying Ar/H₂ flow rate ratio, etched graphene pattern could be modulated from a simple hexagonal pattern to complex fractal geometric patterns (Geng et al., 2013). Cu foils were annealed at 1160 °C for 20-30 min and growth occurred at same temperature with 0.5 sccm CH₄, 800 sccm Ar and 20 sccm H₂ gas flow for 30 min. Etching process applied following growth under varied H₂ gas flows (3-100 sccm) for 5 min.

Based on these studies, we focused on to find actual anisotropic etching parameters of graphene with applying various growth-etching times and gas flow rates. Figure 3.5 roughly shows CVD growth and etching process.

Most of the etching processes were applied at the same temperature with the growth process. But, some samples were also etched at lower temperatures than growth

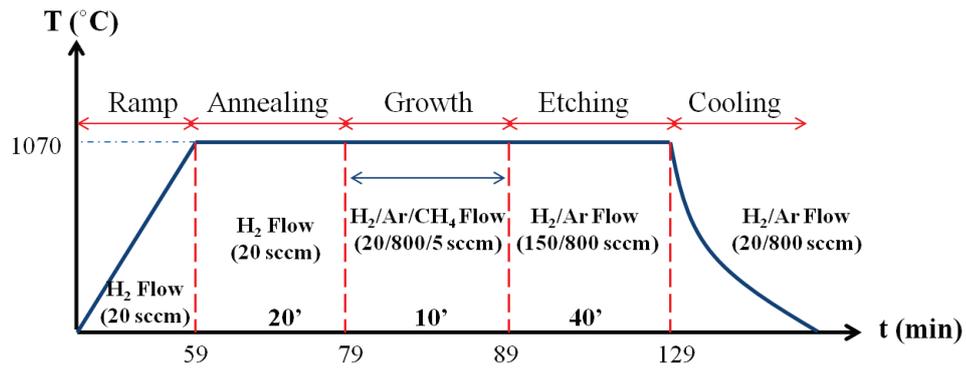


Figure 3.5. Graphene Growth and Etching process of CVD graphene.

temperature¹. Etching process that is belong to these samples are shown in Figure 3.6.

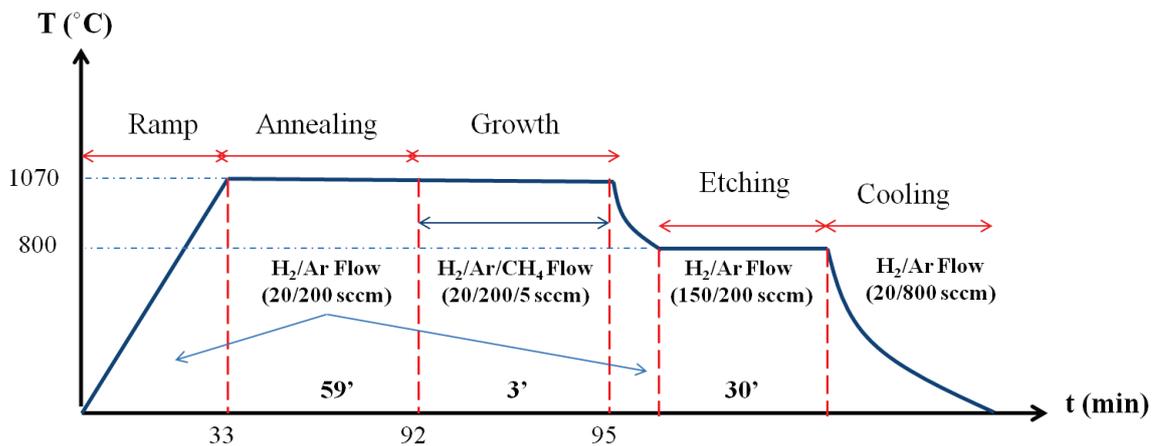


Figure 3.6. Graphene Growth and Etching process of CVD graphene at lower temperature.

Graphene samples that were grown and following reverse-reaction etched on Cu foils with CVD system were listed in Table 3.2.

¹Some of the graphene samples were cooled down to 800 °C under H_2/Ar gas flow after the growth and etching was carried on at 800 °C.

Table 3.2. CVD Grown and Etched Graphene Samples.

Sample	Temperature (°C)	CH ₄ Flow (sccm)	Ar Flow (sccm)	Growth H ₂ (sccm)	Growth Time (min)	Etching H ₂ Flow (sccm)	Etching Time (min)
GRP339	1070	0.5	800	20	30	120	10
GRP343	1070	1	800	20	30	150	10
GRP345	1070	5	800	20	30	150	20
GRP353	1073	5	200	20	3	200	30
GRP356	800	5	200	20	3	150	30
GRP360	1070	5	800	20	12	150	10
GRP372	1070	5	800	20	10	150	15
GRP373	1070	5	800	20	10	150	20
GRP379	1070	0.5	800	20	30	150	20
GRP380	800	0.5	800	20	30	150	20
GRP381	1070	2.7	800	20	30	150	20
GRP393	1070	5	800	20	10	150	40
GRP409	1070	3	200	20	0.5	150	10
GRP414	1070	5	800	20	10	150	15
GRP429	1070	3.6	200	20	10	150	20
GRP438	1070	5	800	20	5	150	40
GRP441	1070	5	200	20	3	150	40
GRP447	1070	5	200	20	0.17	150	20
GRP462	1070	5	800	20	10	150	60
GRP485	1070	5	800	20	10	150	40
GRP486	1070	3.6	800	20	10	150	20

3.6. Graphene Transfer onto Substrates

In the transfer process, S1318 photoresist (PR) was drop casted over graphene layers on Cu foils and annealed at 70 °C for 24 h. Cu/graphene/S1318 PR samples were dipped into FeCl₃ solvent until the Cu foils were etched completely. After rinsed by deionized water and dried by N gas stream, graphene/S1318 PR samples were transferred on SiO₂/Si substrates. Then they were soft baked at 70 °C for 30 sec and hard baked at 120 °C for 2 min. S1318 PR layers were then etched in acetone-acetone-iso-propanol solvents for 20 sec in each, respectively. Transfer process is presented in Figure 3.7.

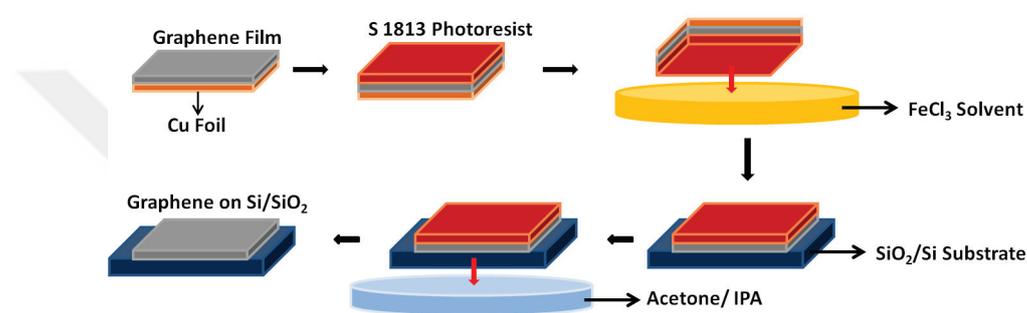
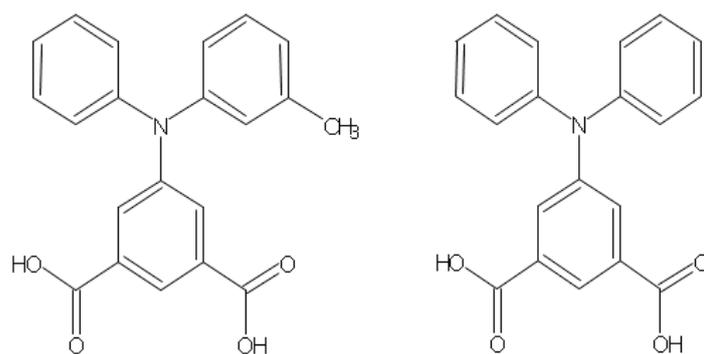


Figure 3.7. Graphene transfer from Cu foil on to SiO₂/Si substrate.

3.7. Self-Assembled Monolayer (SAM) Functionalization

5-[(3-methylphenyl)(phenyl)amino]isophthalic acid (MePIFA) and 5-diphenylamino]isophthalic acid (DPIFA) aromatic small molecules with double bond carboxylic acid were used as self-assembled monolayers (SAMs). The synthesis procedure of SAM molecules was reported in our study (Can et al., 2014). SAM molecules with 1mM concentration were prepared at room temperature in methanol solution. For the graphene based sensor fabrication, graphene films were modified by Me-PIFA and D-PIFA molecules. Molecular structures of these molecules are shown in Figure 3.8. Graphene transferred substrates were kept in methanol-SAM solutions for 24 h to be covered with MePIFA and DPIFA SAM molecules. The substrates were then rinsed with methanol to remove SAM molecules' residues.



MePIFA

5-[(3-methylphenyl)(phenyl)amino]

isophthalic acid

DPIFA

5-(diphenyl)amino]

isophthalic acid

Figure 3.8. Chemical structures of (a) MePIFA and (b) DPIFA SAM molecules.

3.8. Gold Electrode Deposition

Interdigitated gold electrodes were constructed by photolithography technique. Glass substrates were cleaned by standard cleaning process: substrates were kept in ultrasonic bath in DI water - acetone - ethanol - isopropanol - DI water, respectively for 15 min in each. Then they were dried by N₂ stream. For cleaning from volatile species and organic contamination, oxygen plasma was applied.

After the cleaning process of the substrates, they were placed into thermal evaporation system for metal film deposition. When the pressure was reached to 10⁻¹ Torr, thin layer of chromium (Cr) was firstly evaporated over substrates to achieve good mechanical adhesion. Then the gold layer deposited with the thickness of ~ 60 nm was deposited over the Cr layer.

Photolithography process was applied to the metal coated these substrates. We used positive photoresist (PR) during microfabrication. Firstly, positive PR AZ1505 is spin coated over metal films with 4600 rpm for 50 sec. After the applied soft bake process at 90 °C for 5 sec. on a hot plate, UV light exposure was applied. As we used positive PR, when UV light is dropped on it through a mask, polymer chains that exposed are broken up. The mask had 3 μm width and gap separation. The UV exposure was carried

for 3 sec. and the samples were then dipped into developer (AZ726 MIF) solution for 3 sec. for the complete etching of PR layer on exposed area. After the etching of PR, gold deposited regions also had to be etched. For this purpose, solution with the name of Aqua regia which is composed of nitric acid and hydrochloric acid in a volume ratio of 1:3 was used. Gold coated samples were dipped into this solution for 5 sec. and immediately the rinsed in DI water to terminate etching process. The additional Cr layer was also by Cr etchant solution.

After the etching process, constructed gold electrodes were cleaned again with the same cleaning process used at the beginning of the lithography process. Constructed electrode pattern is shown in Figure 3.9.

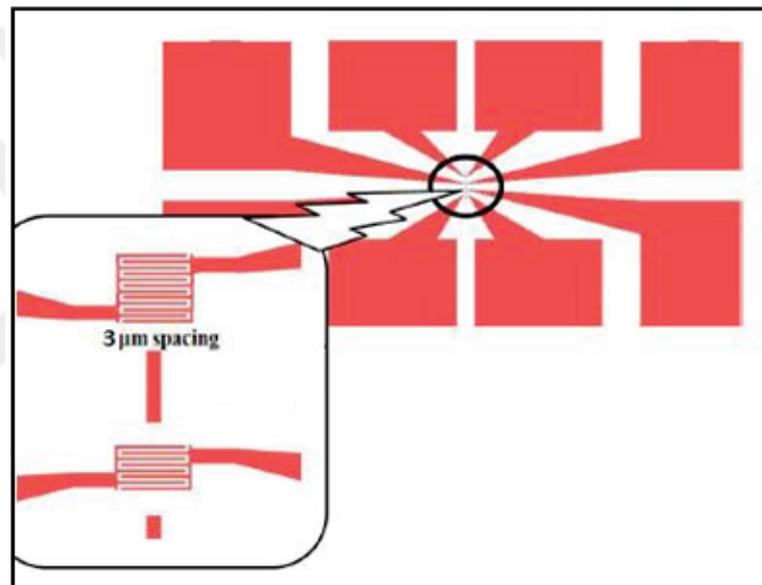


Figure 3.9. Gold electrode scheme that was patterned by photolithography process.

CHAPTER 4

RESULTS AND DISCUSSIONS

4.1. Superficial Characterization

Optical Microscopy, SEM and AFM characterization results are discussed in detail in the following subsections as superficial characterizations.

4.1.1. Optical Characterization

Surface images of bare commercial Cu foils that annealed at four different temperatures taken by optical microscopy during AFM investigations are shown in Figure 4.1.

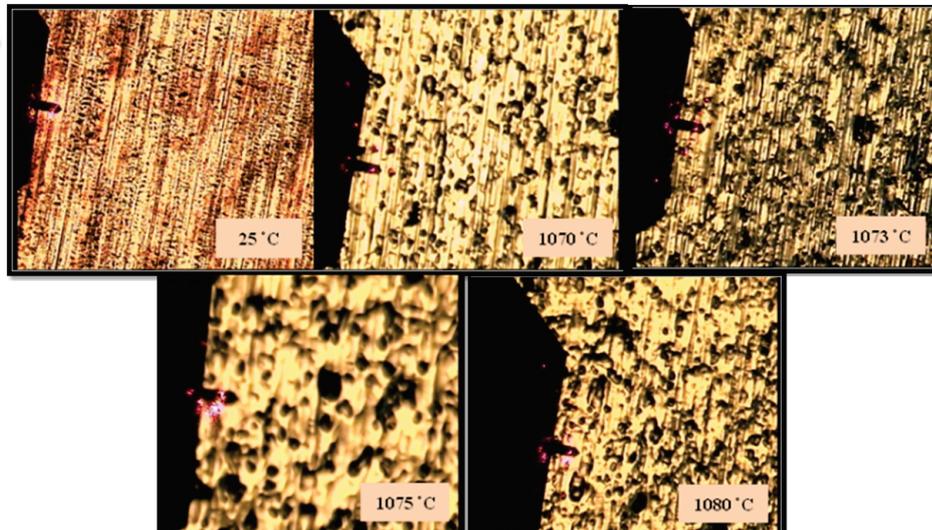


Figure 4.1. Optical microscopy images of bare and annealed commercial Cu foils.

Cu foils were melted at temperatures of 1075 °C and 1080 °C. Optical images that were taken from melted areas are shown in Figure 4.2.

It is clear from Figure 4.2 that stripes were opened and grains were expanding at melting temperatures. The stripes are nucleation sites for graphene growth but at these

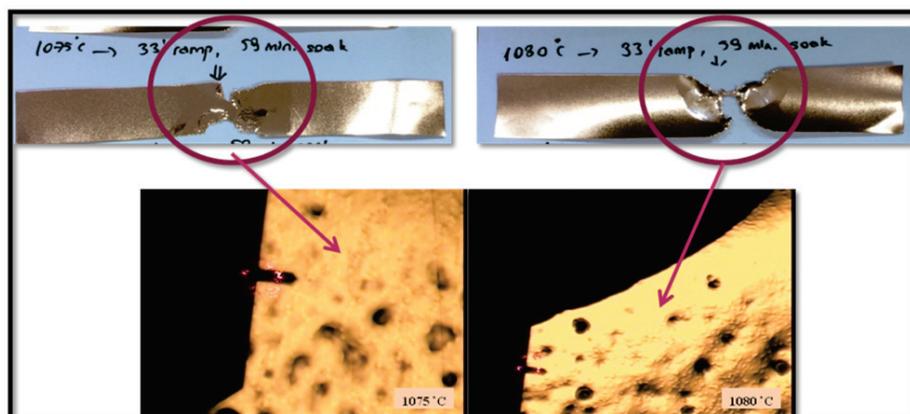


Figure 4.2. Optical images taken from melted sides of Cu foils annealed at 1075 °C and 1080 °C.

sides graphene growth occurs unstrained and multilayer graphene growth becomes unavoidable. Therefore it is important to make these stripes wide by annealing to obtain continuous monolayer graphene sides.

During the growth process of GRP323, Cu foil was annealed at 1070 °C under Ar (200 sccm) and H₂ (20 sccm) gas mixture. Then growth occurred with including 5 sccm CH₄ gas flow for 5 min. Figure 4.3 shows the optical microscopy image of this GRP323 sample.

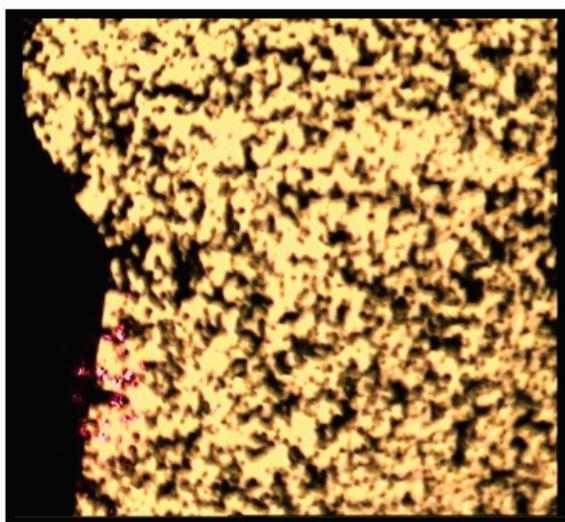


Figure 4.3. Optical microscopy image of GRP323 sample.

GRP402 sample was grown with standard graphene growth process on Cu foil and transferred on to SiO₂/Si wafer. Figure 4.4 shows the optic microscopy images of transferred GRP402 sample with three magnifications.

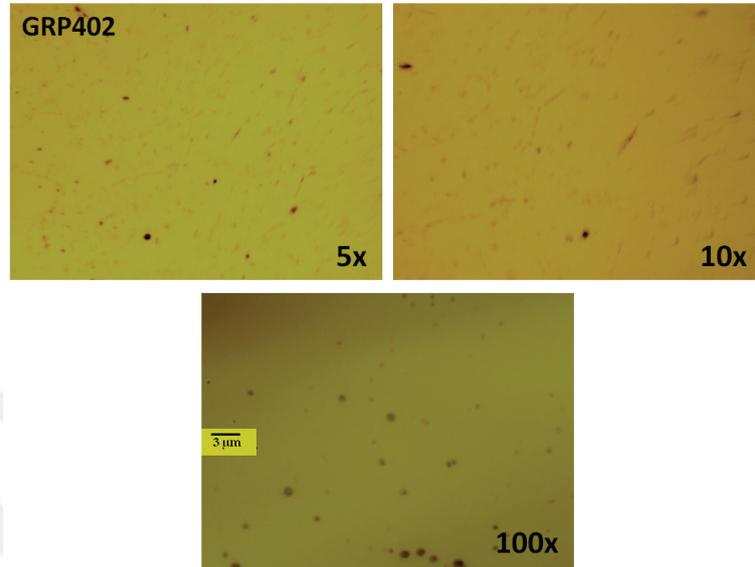


Figure 4.4. Optical microscopy images of GRP402 sample with three different magnifications.

Optical microscopy images of GRP345 and GRP356 on SiO₂/Si substrate with 100x magnification and 3 μm scale bar are shown in Figure 4.5. GRP345 sample was grown under CH₄/H₂/Ar gas flows with 5sccm/ 20sccm/ 800sccm, respectively, for 30 min at 1070 °C. CVD reverse-reaction etching was applied with 150 sccm H₂ and 800 sccm Ar flows for 20 min at 1070 °C. And GRP356 sample was grown under CH₄/H₂/Ar gas flows with 5sccm/ 20sccm/ 200sccm, respectively, for 3 min. at 1073 °C and etched under 200 sccm H₂ and 200 sccm Ar flows for 20 min at 800 °C.

In Figure 4.5 the etching temperature effect may be observed as sample that was etched at higher temperature (GRP345) is unspotted and has wider etched regions but sample that was etched at lower temperature (GRP356) is more defective.

Optical microscopy images of etched GRP372 and GRP373 samples on SiO₂/Si substrates are shown in Figure 4.6. GRP372 was grown on Cu foil at 1070 °C under 5 sccm CH₄, 20 sccm H₂ and 800 sccm Ar flows during 10 min. Etching was done at the same temperature for 15 min under 150 sccm H₂ and 800 sccm Ar gas flows. GRP373 sample was growth with the same parameters of GRP373 and only etching time was extended to 20 min. Optical microscopy images seem different from GRP356 and

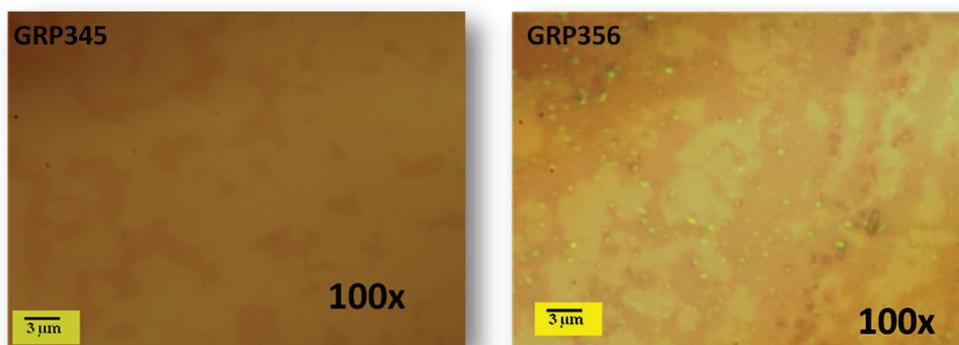


Figure 4.5. Optical Microscopy images of GRP345 and GRP356 samaples.

GRP345, because of the microscope's light bulb change. Contrast difference between etched and un-etched parts of the graphene was unclear, thus we had problems during the Raman measurements.

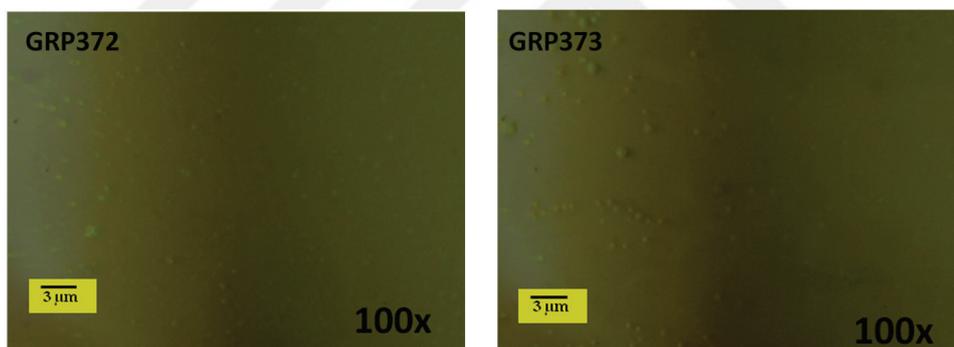


Figure 4.6. Optical Microscopy images of etched GRP372 and GRP373 samples.

GRP379 sample was grown with 0.5 sccm CH_4 , 20 sccm H_2 and 800 sccm Ar gas flows for 30 min and CVD reverse etching was done at 1070 °C under 150 sccm H_2 and 800 sccm Ar gas flows during 20 min. GRP380 sample was grown with 0.5 sccm CH_4 , 20 sccm H_2 and 800 sccm Ar gas flows for 30 min and CVD reverse etching was done at 800 °C under 150 sccm H_2 and 800 sccm Ar gas flows during 20 min. It is seen from Figure 4.7. that etching at lower temperatures are also possible. But etched area regions of GRP379 are more significant.

GRP381 sample was grown on Cu foil at 1070 °C under 2.5 sccm CH_4 , 20 sccm H_2 and 800 sccm Ar gas flows for 30 min. Etching was carried with 150 sccm H_2 and

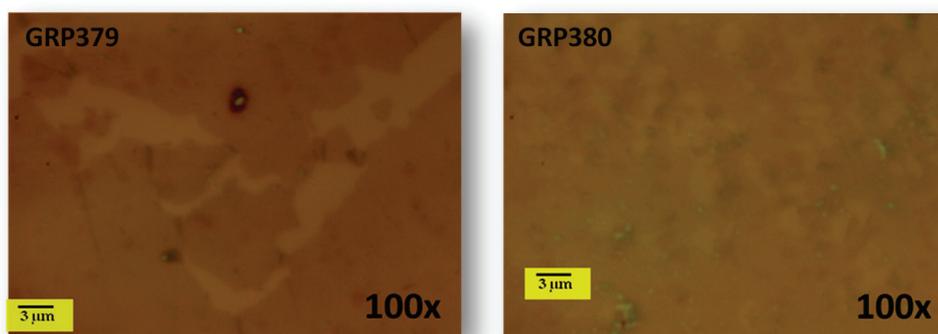


Figure 4.7. Optical Microscopy images of GRP379 and GRP380 samples.

800 sccm Ar gas flows for 20 min at the same temperature. Hexagon-like shapes are very distinct (Figure 4.8).

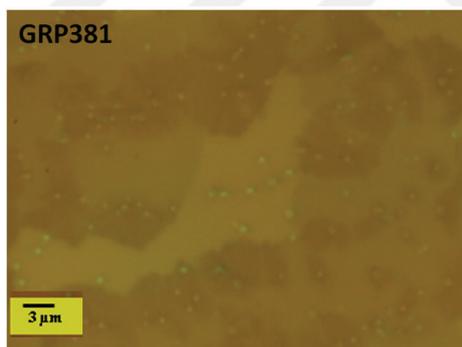


Figure 4.8. Optical Microscopy images of GRP381 sample.

Optical microscopy images of GRP414 and GRP462 samples on SiO₂/Si substrate are shown in Figure 4.9. GRP414 sample was grown under CH₄/H₂/Ar gas flows with 5sccm/ 20sccm/ 800sccm, respectively, for 10 min CVD reverse-reaction etching was applied with 150 sccm H₂ and 800 sccm Ar flows for 15 min. Both growth and etching processes were carried at 1070 °C. GRP462 sample was grown with the same parameters with GRP414 sample; however, it was etched for 60 mins. under 150 sccm while GRP414 was etched for 15 min. Etching time of 60 min led to full graphene etching from the surface, therefore, graphitic peaks couldn't obtained from the surface of GRP462 during Raman investigation.

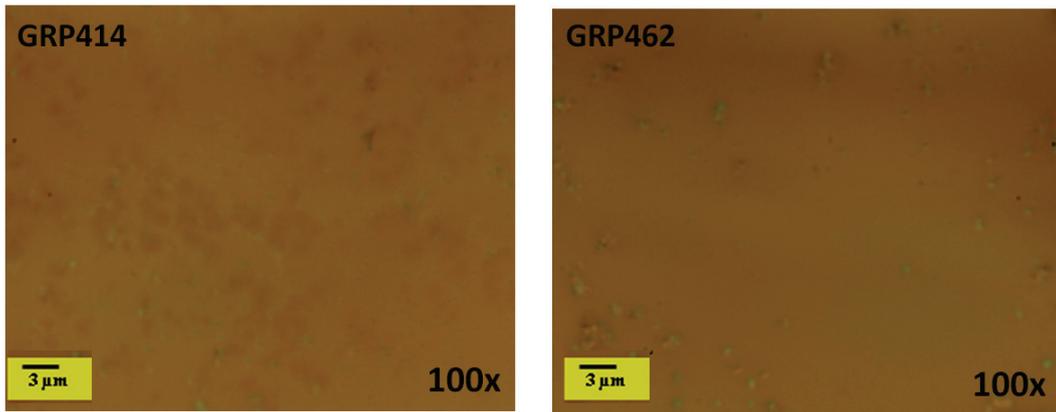


Figure 4.9. Optical Microscopy images of GRP414 and GRP462 samples.

GRP429 was grown under $\text{CH}_4/\text{H}_2/\text{Ar}$ gas flows with 5sccm/ 20sccm/ 800sccm, respectively, for 10 min. CVD reverse-reaction etching was applied with 150 sccm H_2 and 800 sccm Ar flows for 20 min. And GRP438 was grown under $\text{CH}_4/\text{H}_2/\text{Ar}$ gas flows with 5sccm/ 20sccm/ 800sccm, respectively, for 5 min. CVD reverse-reaction etching was applied with 150 sccm H_4 and 800 sccm Ar flows for 40 min. Both growth and etching processes for two samples were carried at 1070 °C. Their optical microscopy images are shown in Figure 4.10.

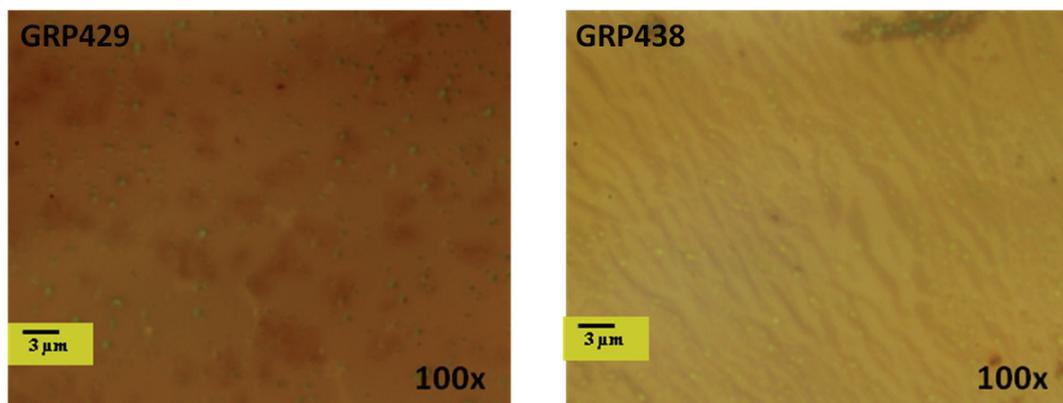


Figure 4.10. Optical Microscopy images of GRP429 and GRP438 samples.

GRP485 sample was grown under $\text{CH}_4/\text{H}_2/\text{Ar}$ gas flows with 5sccm/ 20sccm/ 800sccm, respectively, for 10 min. CVD reverse-reaction etching was applied with 150 sccm H_2 and 800 sccm Ar flows for 40 min. And GRP486 was grown under $\text{CH}_4/\text{H}_2/\text{Ar}$ gas flows with 3.6sccm/ 20sccm/ 800sccm, respectively, for 10 min. CVD reverse-reaction etching was applied with 150 sccm H_2 and 800 sccm Ar flows for 20 min. Both growth and etching processes for two samples were carried at 1070 °C. Their optical microscopy images are shown in Figure 4.11.

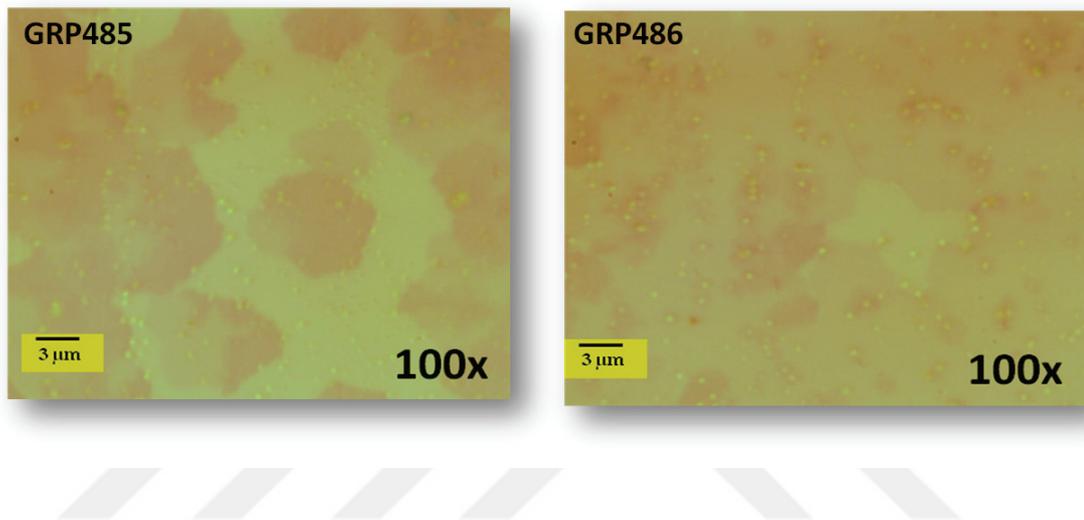


Figure 4.11. Optical Microscopy images of GRP485 and GRP486 samples.

When the contrast difference of GRP486 sample is considered, it is composed of three different layered regions.

GRP463 sample was grown with standard graphene growth parameters and transferred on to combed gold electrodes to use it in electrical gas sensing experiments. Its optical images on gold electrodes are shown in Figure 4.12. with four different magnifications.

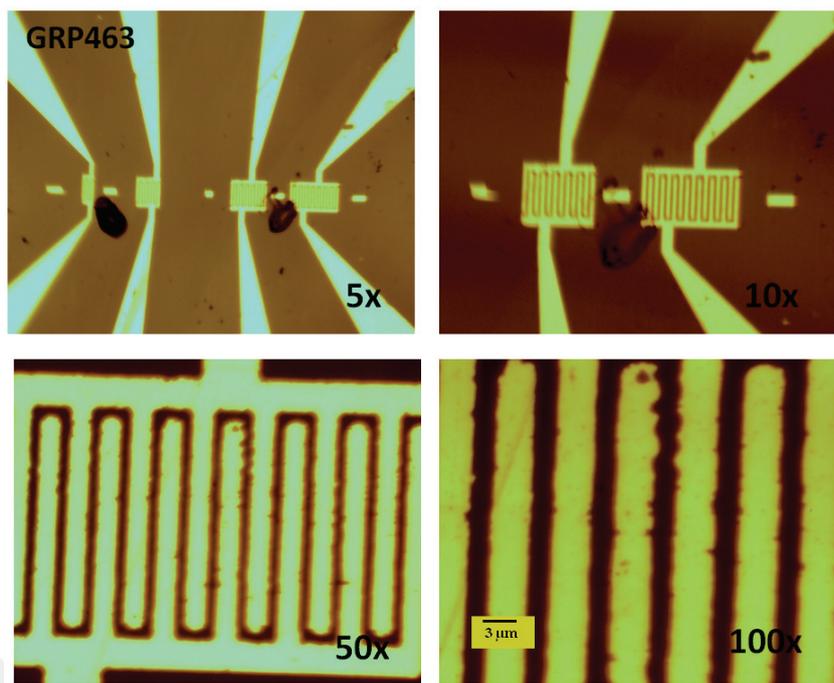


Figure 4.12. Optical Microscopy images of GRP463 with four different magnifications.

4.1.2. Scanning Electron Microscopy (SEM) Characterization

SEM images of GRP394 sample that was grown with 5 sccm CH_4 , 20 sccm H_2 and 800 sccm Ar gas flows are presented in Figure 4.13.

It is seen from the Figure 4.13 that, there are various graphene grains over the Cu surface consisting many stepped terraces and pits. EDX analysis showed that particles located on graphene surfaces are mostly belongs to oxidized silicon elements that were formed by impurities come from Cu foil and quartz tube during the growth process.

CVD grown GRP393 sample with same parameters of GRP394 sample was etched with reverse-reaction at 1070 °C for 40 min under 150 sccm H_2 and 800 sccm Ar gas exposures on Cu Foil substrates. SEM images are shown in Figure 4.14.

From these results we see that, etched parts of the Cu foil have lighter contrast compared to graphene coated grains and similar to GRP394 sample, they consist of terraces and pits.

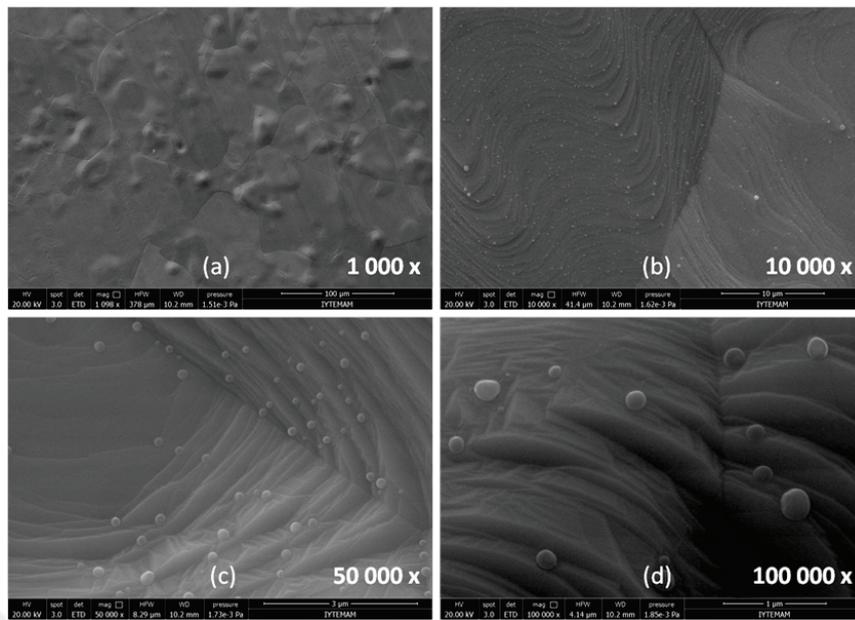


Figure 4.13. SEM images of GRP394 sample on Cu foil with (a) 1000x, (b) 10000x, (c) 50000x and (d) 100000x magnifications.

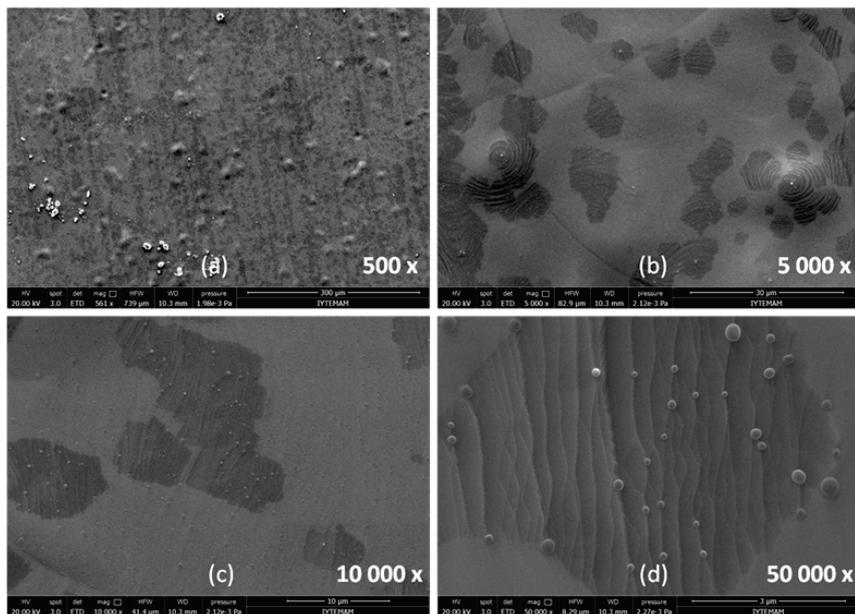


Figure 4.14. SEM images of GRP393 sample on Cu Foil with (a) 500x, (b) 5000x, (c) 10000x and (d) 50000x magnifications.

SEM images of four different graphene/SiO₂/Si samples that were grown and etched by various parameters are presented in Figure 4.15.

While GRP345 was grown under 5 sccm CH₄, 20 sccm H₂ and 800 sccm Ar flows, GRP381 was grown under 2.7 sccm CH₄ for 30 min. Both of these two samples were etched under 150 sccm H₂ and 800 sccm Ar gas flows for 20 min. It is seen that multilayer graphene films were etched easier than that of monolayer graphene films in the same etching time interval.

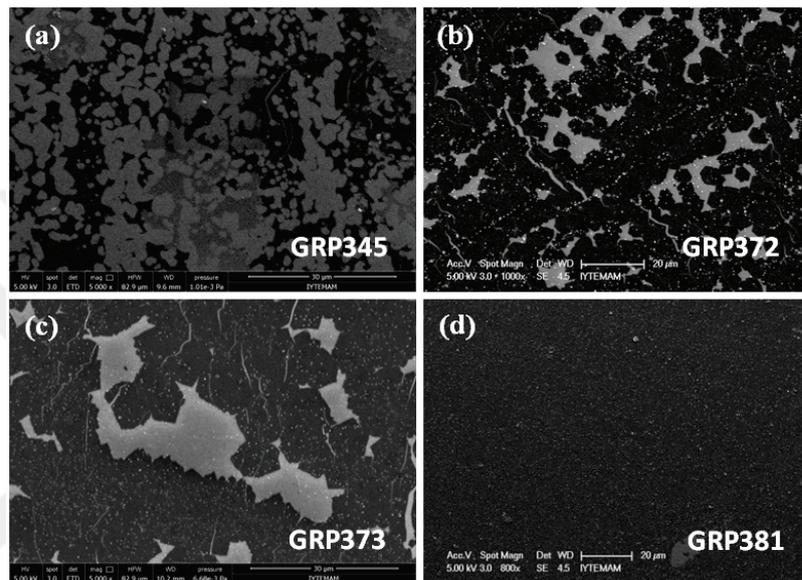


Figure 4.15. SEM images of (a) GRP345, (b) GRP372, (c) GRP373 and (d) GRP381 samples with (a)-(c) 30 μm and (b)-(c) 20 μm scale bars.

GRP372 and GRP373 samples were both grown under 5 sccm CH₄ flow for 10 min and while GRP372 was etched under 150 sccm H₂ flow and 800 sccm Ar flow for 15 min, GRP373 was etched under 150 sccm for 20 min. From the SEM images we can see that, this 5 min of etching time difference didn't affect the surface morphology too much. Images that are shown in Figure 4.16 also support this condition.

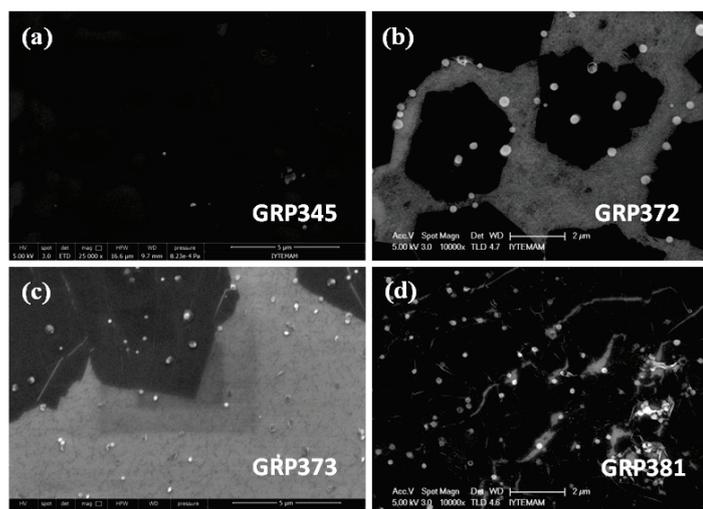


Figure 4.16. SEM images of (a) GRP345, (b) GRP372, (c) GRP373 and (d) GRP381 samples with (a)-(c) 5 μm and (b)-(c) 2 μm scale bars.

As mentioned before in chapter 3 and in section 3.5, some reverse-reaction CVD etchings were carried at 800 °C. To indicate the etching temperature effect, SEM images of GRP379 sample that was etched at 1070 °C and GRP380 sample that was etched at 800 °C are presented in Figure 4.17.

Scanning Electron Microscopy images of H₂ etched and transferred GRP429 sample by reverse reaction method are presented in Figure 4.18. Etched graphene flakes are observed as sharp-pointed due to the anisotropic H₂ etching.

GRP485 sample was grown under 5sccm CH₄/20 sccm H₂ /800 sccm Ar gas flows on Cu foil for 10 min and etched under 150 scmm H₂/800 sccm Ar gas flows for 40 min. Then sample was transferred from Cu surface on to SiO₂/Si substrate. SEM images of GRP485 that are taken by 1000x, 2500x, 5000x and 10000x magnifications are shown in Figure 4.19.

While the etched areas are represented by lighter contrast, graphene flakes have darker contrast. From the SEM images presented in Figure 4.19 it is obvious that lighter areas are completely etched after the etching process and graphene flakes are also etched anisotropically. Graphene flakes are inclined honeycomb structures.

GRP486 sample was grown under 3.6 sccm CH₄/20 sccm H₂ /800 sccm Ar gas flows on Cu foil for 10 min and etched under 150 scmm H₂/800 sccm Ar gas flows for 200 min. Then sample was transferred from Cu surface on to SiO₂/Si substrate. SEM images of GRP486 that are taken by 1000x, 2500x, 5000x and 10000x magnifications are shown in Figure 4.20.

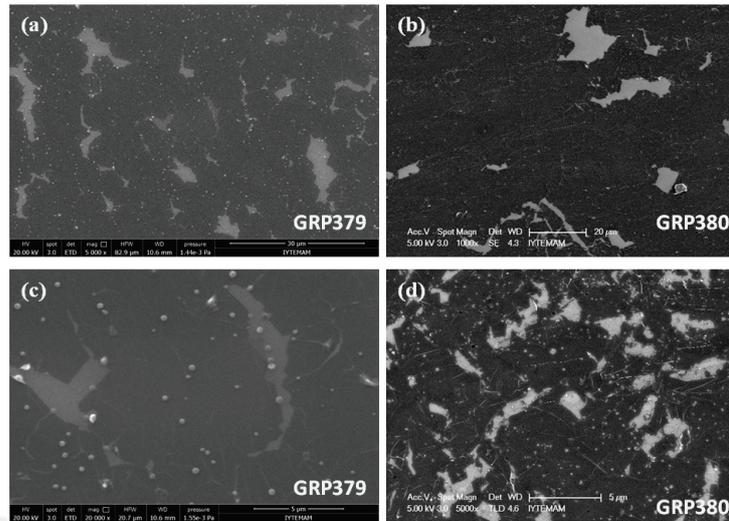


Figure 4.17. SEM images of (a) GRP379 sample with 30 μm , (b) GRP380 sample with 20 μm , (c) GRP379 and (d) GRP380 samples with 5 μm scale bars.

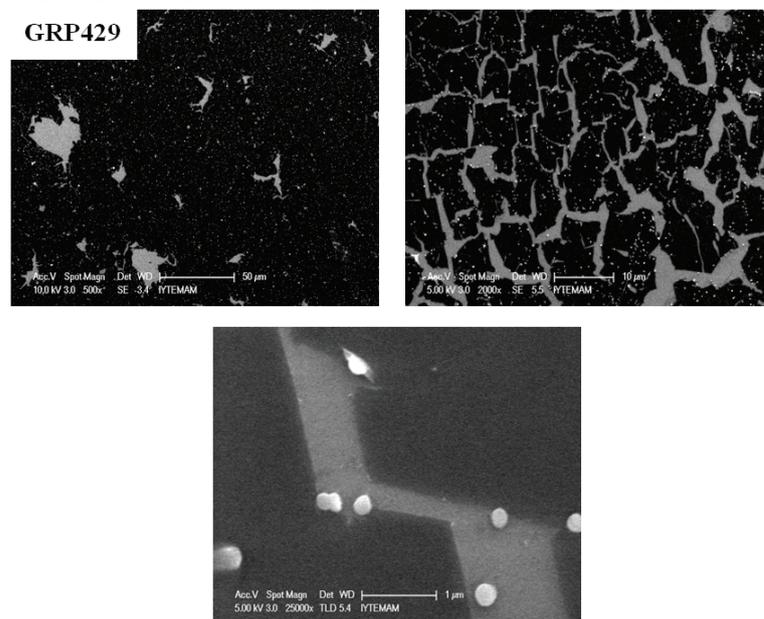


Figure 4.18. SEM images of etched GRP429 sample with (a) 50 μm , (b) 10 μm and (c) 1 μm scale bars.

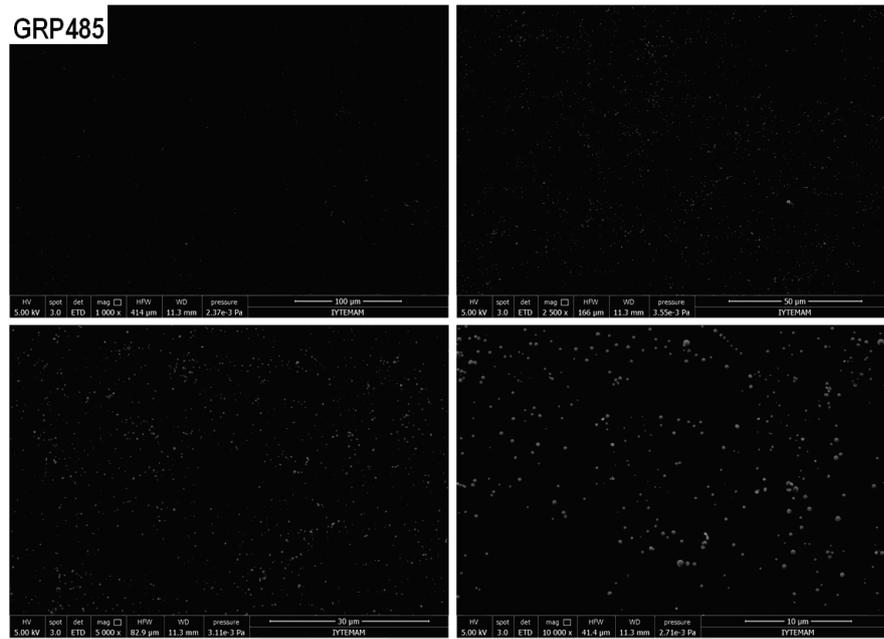


Figure 4.19. SEM images of etched GRP485 sample on SiO₂/Si with a)1000x, b) 2500x, c) 5000x and d) 10000x magnifications.

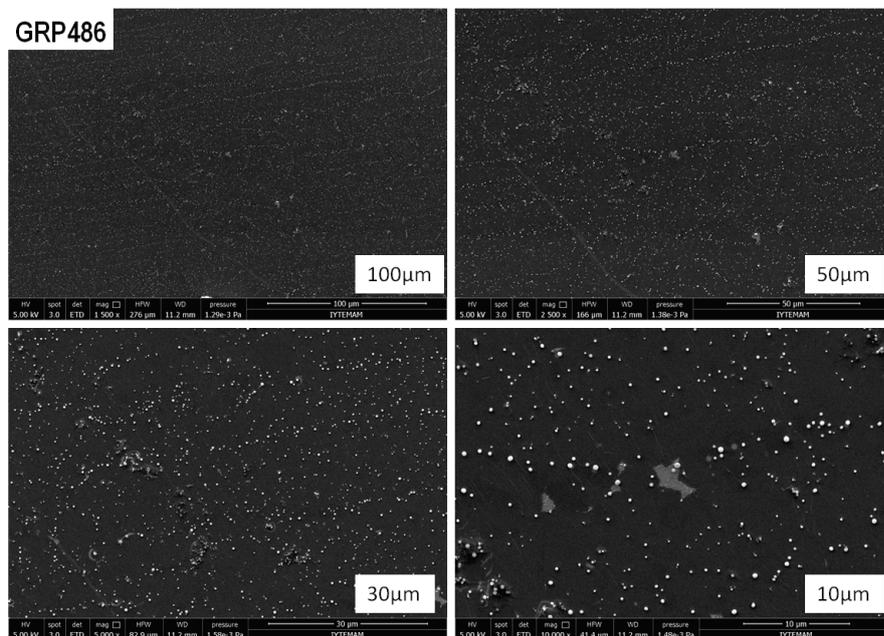


Figure 4.20. SEM images of etched GRP486 sample on SiO₂/Si with a)1000x, b) 2500x, c) 5000x and d) 10000x magnifications.

When compared to GRP485 sample, GRP486 has lower amount and sized completely etched regions. If GRP486 is considered as few layered graphene, etching process may be resulted with gradually etching. Therefore, optical microscopy and Raman spectrometry results give more significant information.

GRP428 sample was grown with standard growth parameters and transferred on to quartz crystal for gas sensing measurements. SEM images after transfer on gold coated crystal are shown in Figure 4.21.



Figure 4.21. SEM images of GRP428 sample on gold coated QCM with a) 35x, b) 200x and c) 2000x magnifications.

4.1.3. Atomic Force Microscopy (AFM) Characterization

Surface topography and phase contrast images were investigated by AFM at tapping (semi-contact) mode. During all the scans, a golden silicon tip with a curvature of 10 nm was used.

Surface topography and phase contrast images of bare commercial Cu foils that were investigated by AFM are presented in Figure 4.22.

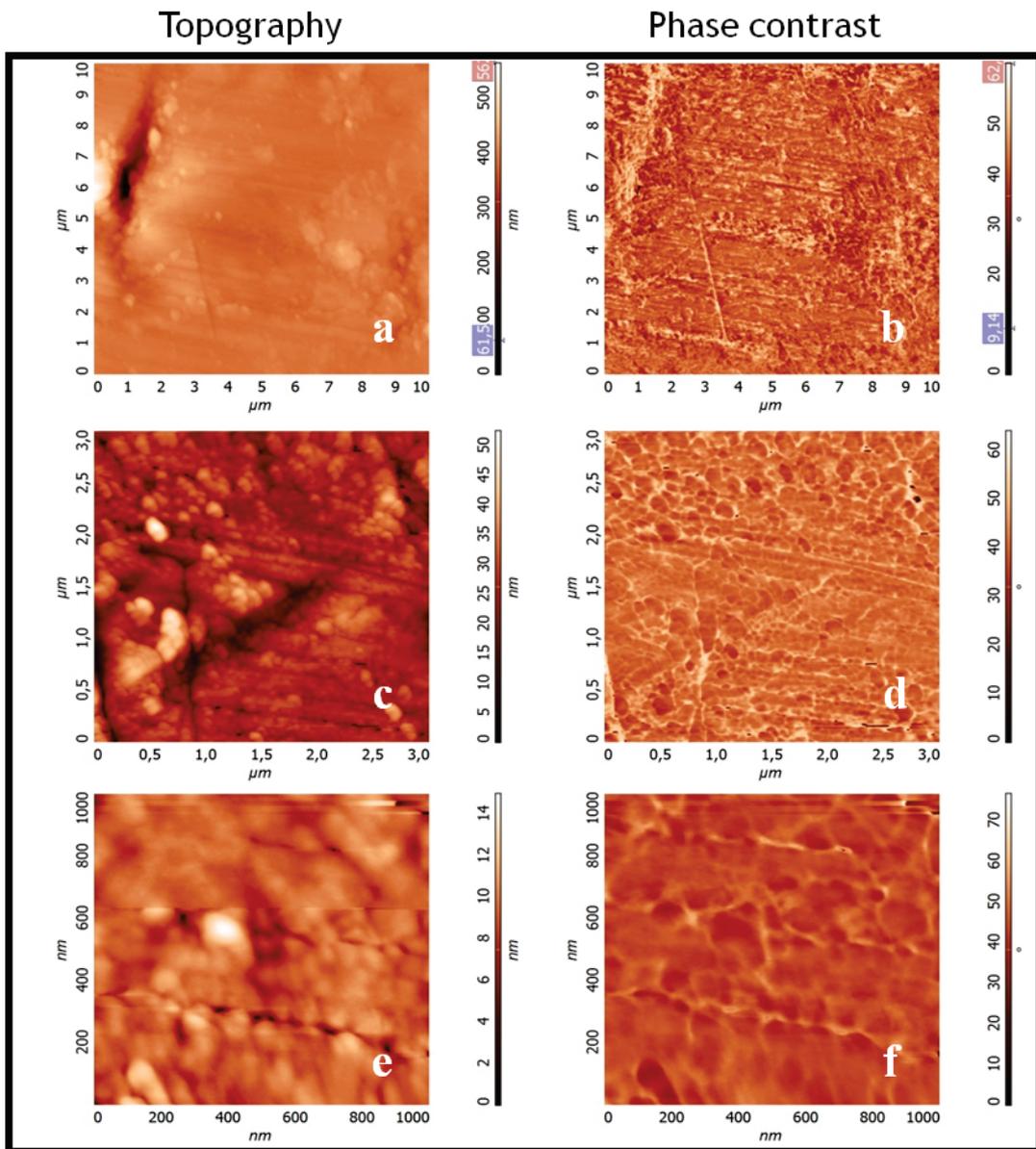


Figure 4.22. Surface topography (a, c, and e) and phase contrast (b, d and f) images of bare Cu Foil with $10 \mu\text{m}^2$, $3 \mu\text{m}^2$ and $1 \mu\text{m}^2$ areas.

Cu foils that were annealed at 1070 °C had surface topography and phase contrast from 3 μm^2 area like shown in Figure 4.23.

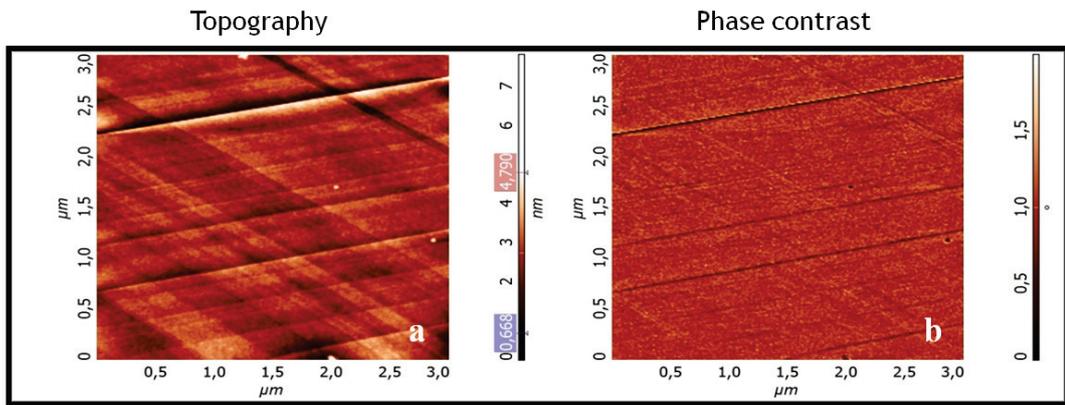


Figure 4.23. (a) Surface topography and (b) phase contrast images of Cu foils annealed at 1070 °C taken from 3 μm^2 area.

When compared with not annealed samples, annealed sample has lower roughness and opened strip characteristics which we need in graphene growth. Surface topography and phase contrast images of Cu foils that annealed at 1073 °C is presented in Figure 4.24.

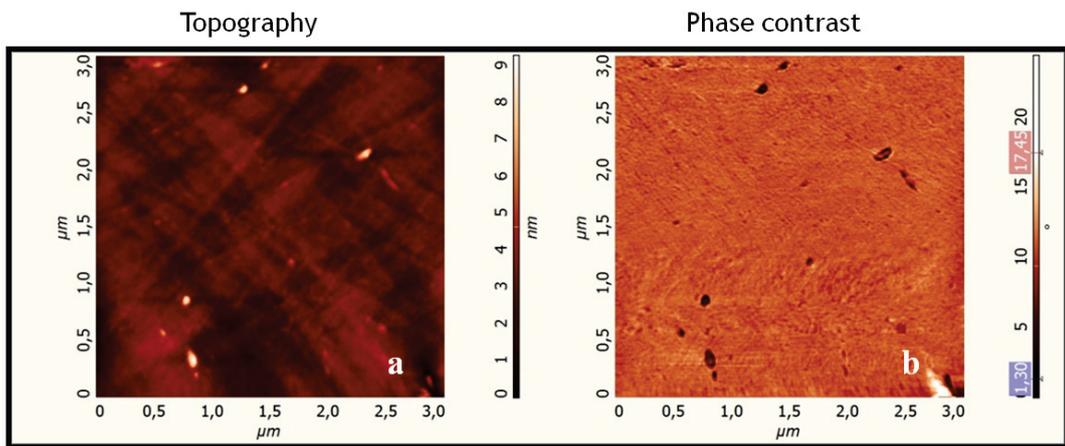


Figure 4.24. (a) Surface topography and (b) phase contrast images of Cu foils annealed at 1073 °C taken from 1 μm^2 area.

Surface topography and phase contrast images of Cu foils that annealed at 1075 °C is shown in Figure 4.25.

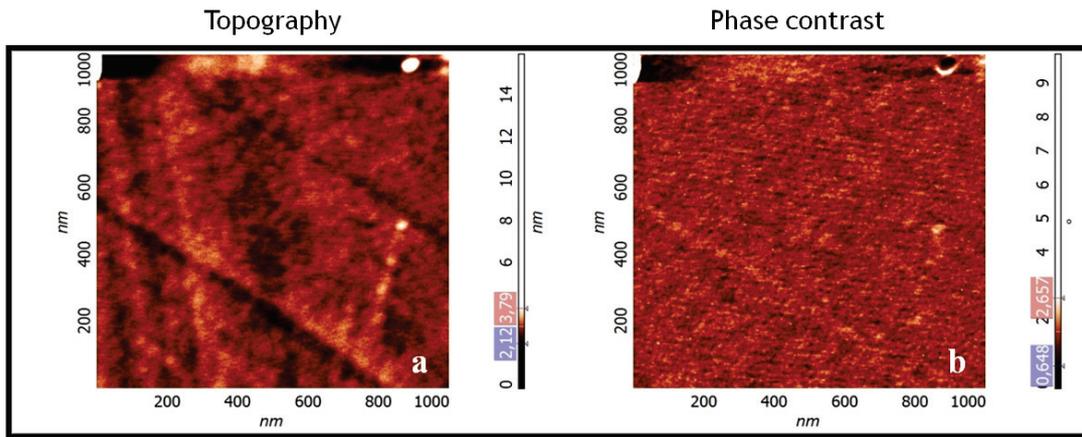


Figure 4.25. (a) Surface topography and (b) phase contrast images of Cu foils annealed at 1075 °C taken from 3 μm^2 area.

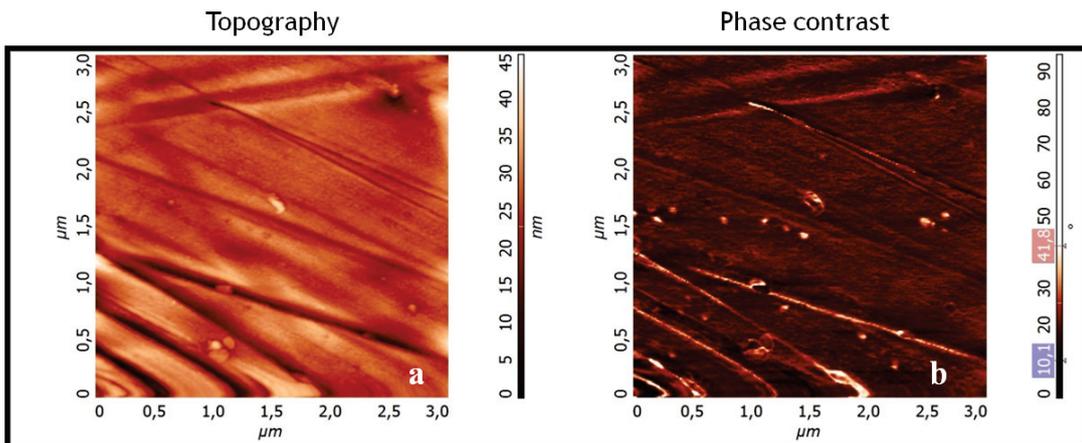


Figure 4.26. (a) Surface topography and (b) phase contrast images of Cu foils annealed at 1080 °C taken from 3 μm^2 area.

Surface topography and phase contrast images of Cu foils that annealed at 1080 °C is presented in Figure 4.26.

As mentioned before, sample regions near the center were melted at 1080 °C. Surface topography images that were taken from these sides are shown in Figure 4.27.

We found that with annealing up to 1080 °C, especially at melting sides, surface roughness (rms) value decreased from 4.993 nm to 1.299 nm.

Surface topography and phase contrast images of grown GRP323 sample with

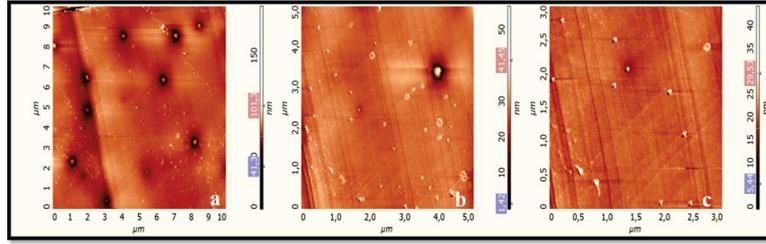


Figure 4.27. Surface topography images of Cu foils annealed at 1080 °C taken from (a) 10, (b) 5 and (c) 3 μm^2 areas.

three different scanning areas are presented in Figure 4.28.

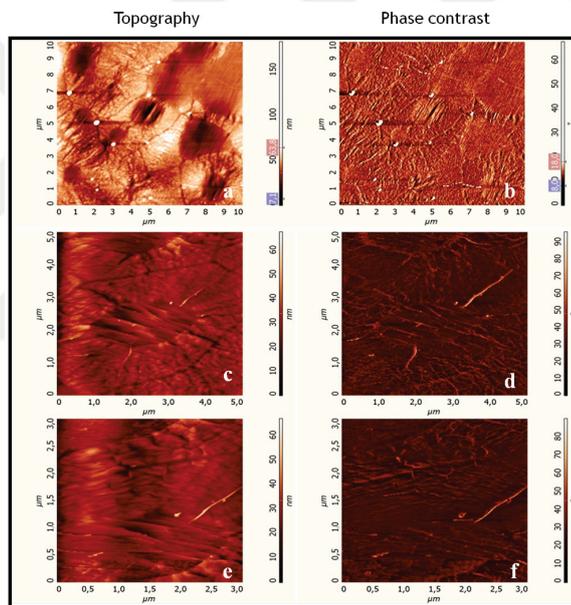


Figure 4.28. Surface topography and phase contrast images of GRP323 sample from (a) 10 μm^2 , (b) 5 μm^2 and (c) 3 μm^2 area.

Graphene growth of nucleation seeds and Cu grain boundaries are seen from AFM images of GRP323 sample clearly (Fig. 4.28).

4.2. Structural Characterization

Raman spectrometry and Kelvin probe force microscopy results are discussed under structural characterization sections.

4.2.1. Raman Spectroscopy Results

Raman Spectrum of the GRP312 sample and its optical microscopy images with and without laser are shown in Figure 4.29. Laser points the region that is investigated during spectra measurement.

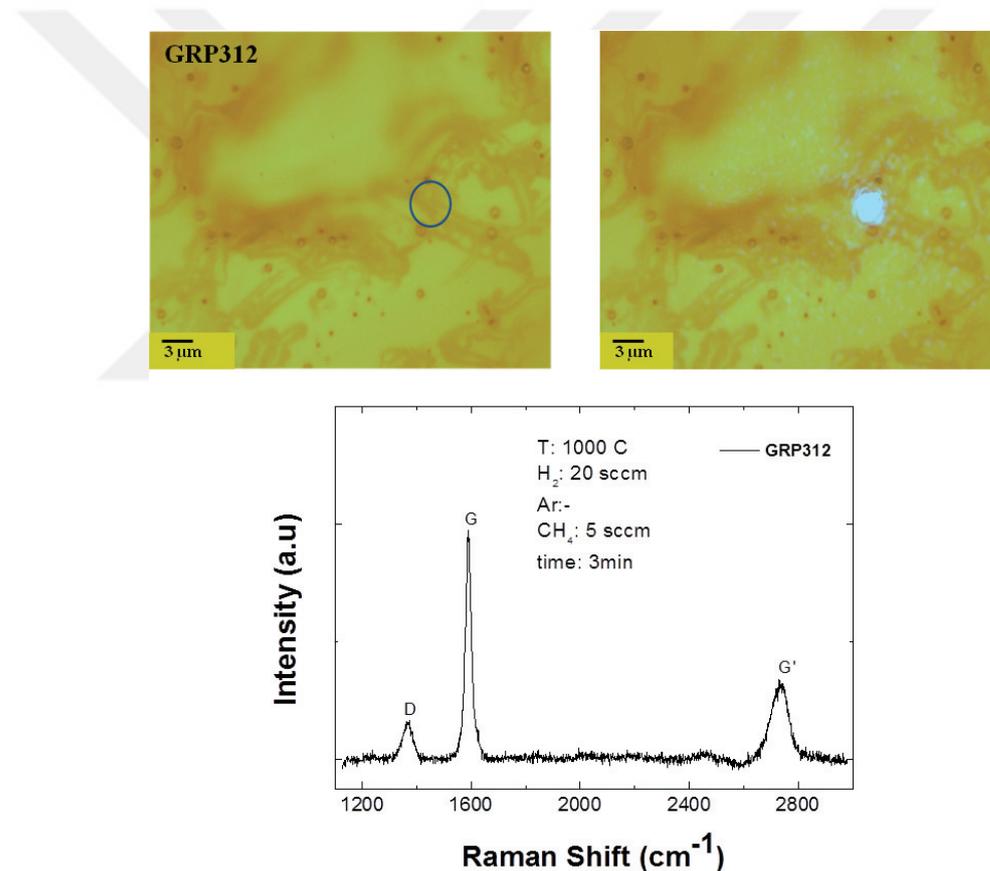


Figure 4.29. Optical Microscopy images and Raman Spectrum of GRP312 sample.

Raman spectrum on selected region shows two main peaks including a G band 1590 cm⁻¹ and G' 2735 cm⁻¹. The intensity ratios of the G to G' peaks give information about the number of layer. Additionally the intensity ratio of D to G peaks gives information about the defect sides, thus, information about the quality of the graphene sample.

For GRP312 sample the ratio of $I_G/I_{G'}$ ~ 3 and symmetric G' peak with a full width at half maximum (FWHM) of 74 cm^{-1} (Figure 4.30). The D peak located at 1368 cm^{-1} with low intensity corresponds to graphene with low defected sides. The intensity ratio I_D/I_G is ~ 0.162 .

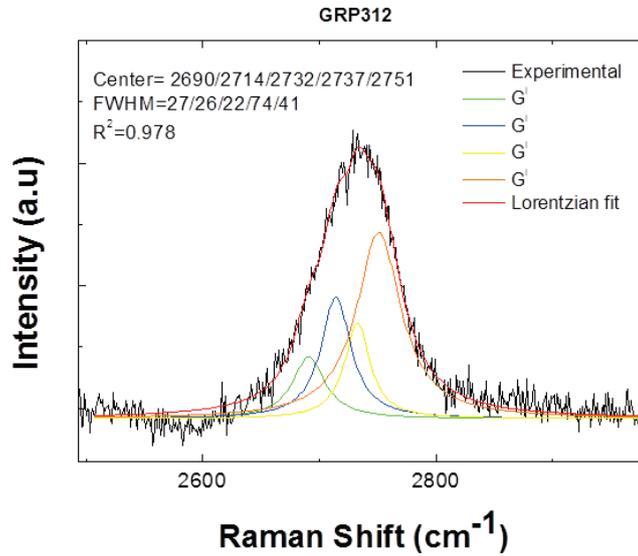


Figure 4.30. G' band Raman spectrum of GRP312 sample that is fitted with four Lorentzian.

Raman Spectrum of the GRP318 sample and its optical microscopy images with and without laser are shown in Figure 4.31. Raman spectrum on selected region shows two main peaks including a G band at 1593 cm^{-1} and G' band at 2729 cm^{-1} . For GRP318 sample the ratio of $I_G/I_{G'}$ ~ 1.36 and symmetric G' peak with a FWHM of 58 cm^{-1} (Figure 4.32). The D peak located at 1372 cm^{-1} and the intensity ratio I_D/I_G is ~ 0.318 .

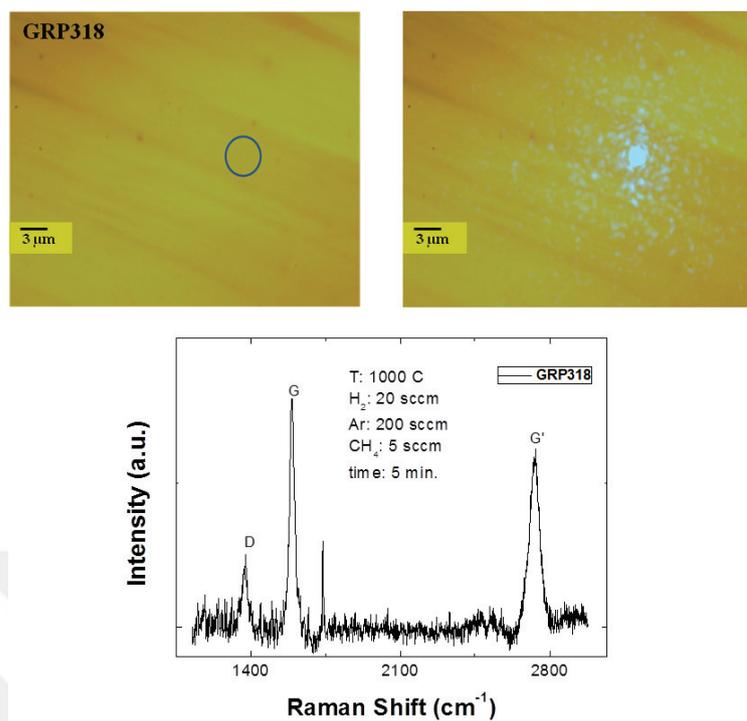


Figure 4.31. Optical Microscopy images and Raman Spectrum of GRP318 sample.

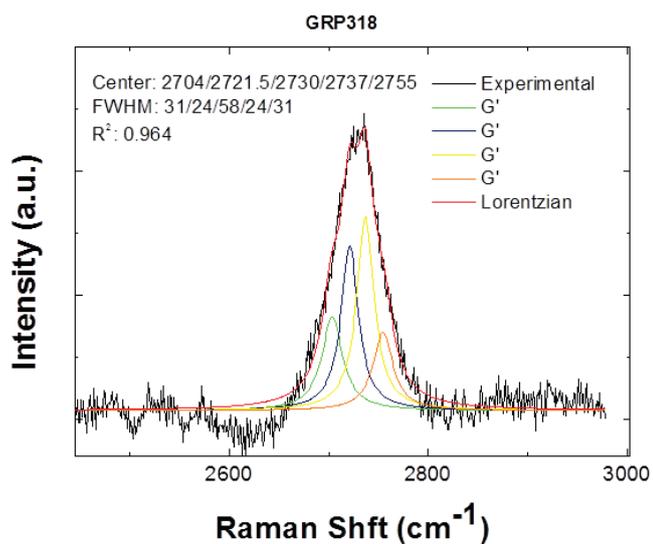


Figure 4.32. G' band Raman spectrum of GRP318 sample that is fitted with four Lorentzian.

Figure 4.33 shows the optical microscopy images of GRP320 sample with and without laser and the Raman spectrum taken from circled area. While G band located at 1590 cm^{-1} , D and G' bands located at 1366 cm^{-1} and 2712 cm^{-1} , respectively. Intensity ratio of G band to G' band was $I_G/I_{G'} \sim 0.69$ and intensity ratio of D band to G band was $I_D/I_G \sim 0.15$.

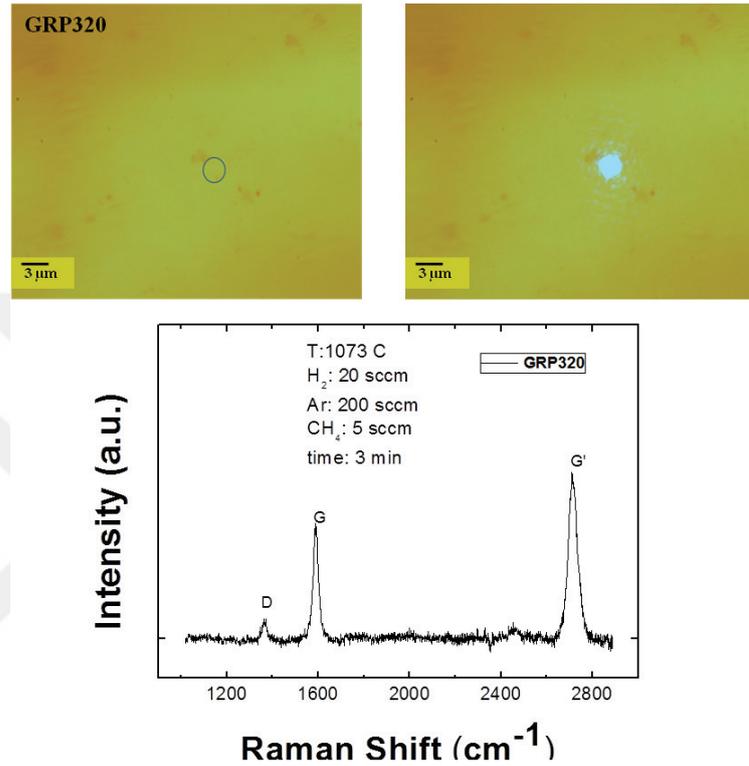


Figure 4.33. Optical Microscopy images and Raman Spectrum of GRP320 sample.

Symmetric G' band had a FWHM of 44 cm^{-1} , as shown in Figure 4.34.

Raman spectrometry results taken from etched part of the GRP345 sample is shown in Figure 4.35. The spectra taken from the lighter regions that were etched during CVD reverse-reaction doesn't include any graphitic peaks and thus support successful etching.

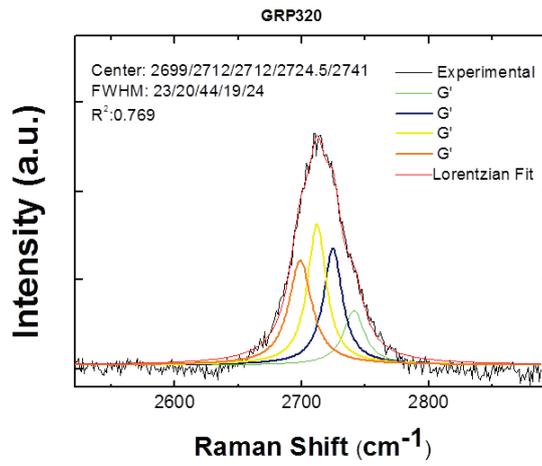


Figure 4.34. G' band Raman spectrum of GRP320 sample that is fitted with four Lorentzian.

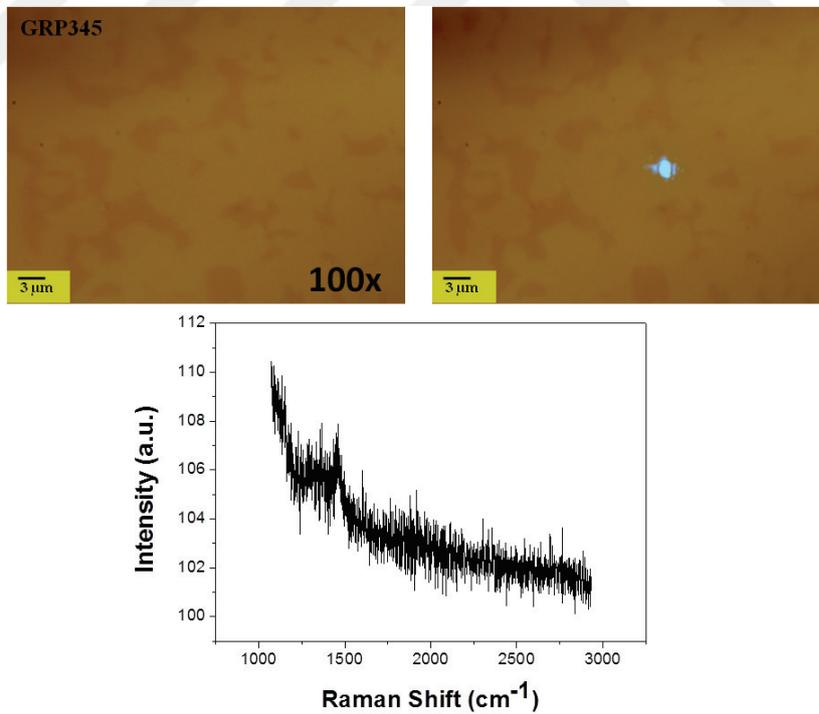


Figure 4.35. Optical Microscopy images with/without laser reflection and Raman Spectrum of GRP345 sample from etched area.

In Figure 4.36, Raman spectrum that was taken from darker regions belongs to multi-layer graphene on SiO₂/Si substrate. D peak that is representing defect sites becomes clear due to PMMA residuals of transfer process.

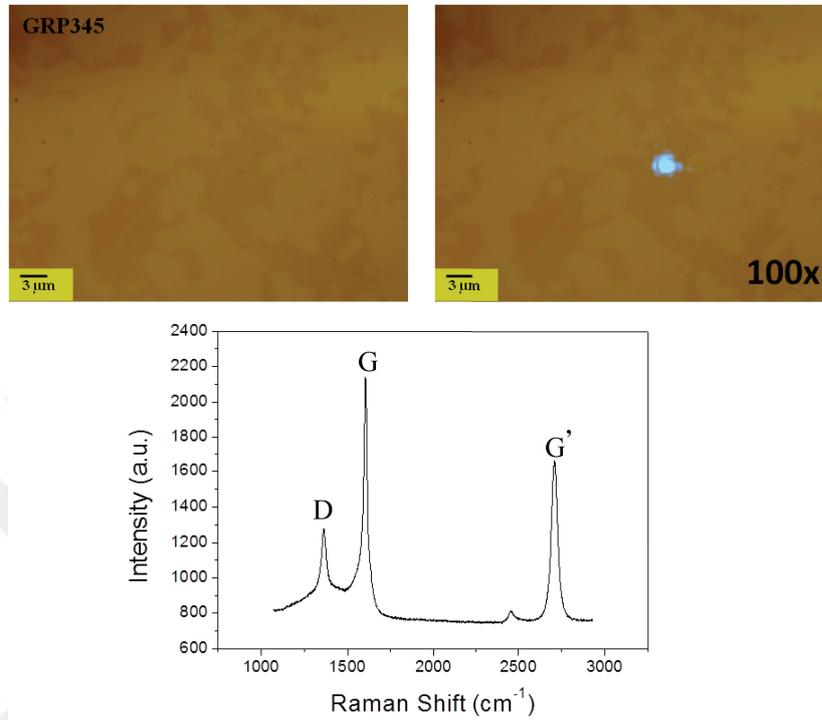


Figure 4.36. Optical Microscopy images with/without laser reflection and Raman Spectrum of GRP345 sample from non-etched area.

Raman spectrum on selected region shows two main peaks including a G band 1603 cm^{-1} and G' 2707 cm^{-1} . The intensity ratios of the G to G' peaks give information about the number of layers. Additionally the intensity ratio of D to G peaks gives information about the defect sites, thus, information about the quality of the graphene sample. For GRP345 sample the ratio of $I_G/I_{G'} \sim 1.28$ and symmetric G' peak with a FWHM of 42 cm^{-1} (Figure 4.37). The D peak located at 1363 cm^{-1} with the intensity ratio $I_D/I_G \sim 0.60$.

GRP356 sample was etched with reverse-reaction at $800\text{ }^\circ\text{C}$. Regions with lighter contrast shows etched parts of the film and Raman spectrum that belongs to these are shown in Figure 4.38. From the spectrum we see that etched parts are bi-layer graphene with higher defective sites.

G band located at 1597 cm^{-1} , D and G' bands located at 1360 cm^{-1} and 2704 cm^{-1} , respectively. Intensity ratio of G band to G' band was $I_G/I_{G'} \sim 0.89$ and intensity

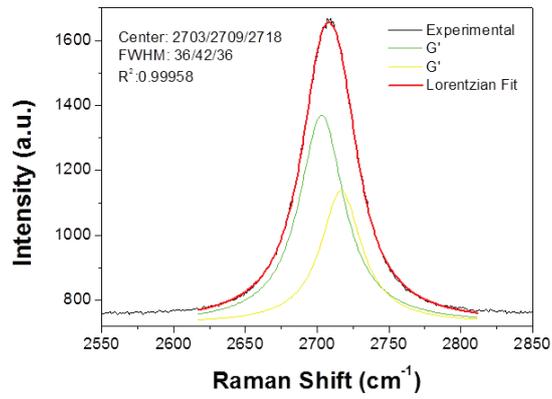


Figure 4.37. G' band Raman spectrum of GRP345 sample that was fitted with two Lorentzian.

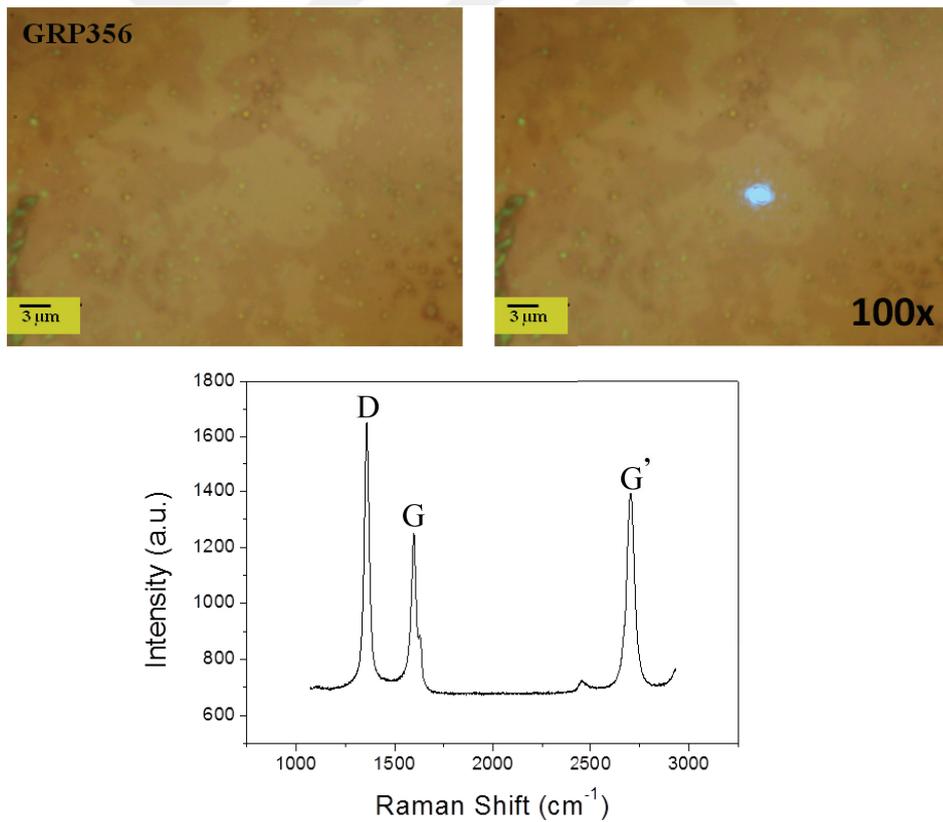


Figure 4.38. Optical Microscopy images with/without laser reflection and Raman Spectrum of GRP356 sample from etched area.

ratio of D band to G band was $I_D/I_G \sim 1.32$.

Figure 4.39. shows G' band spectrum four Lorentzian fits and have a symmetric G' peak with a FWHM of 46 cm^{-1} .

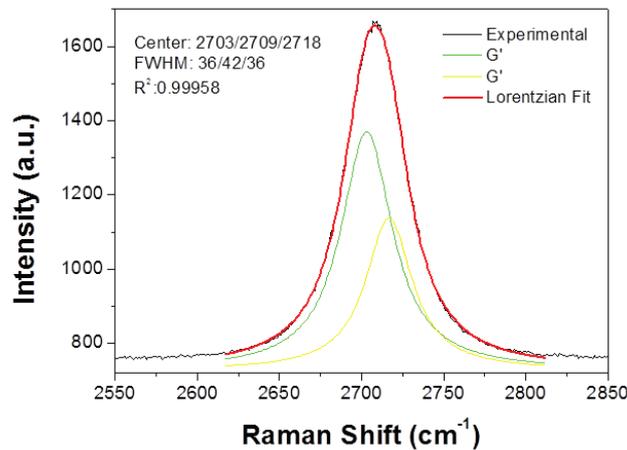


Figure 4.39. G' band Raman spectrum of GRP356 sample that was fitted with four Lorentzian.

Raman spectrum taken from darker sides is multi-layer graphene (Figure 4.40) where G band is located at 1586 cm^{-1} , G' is located at 2719 cm^{-1} and D is at 1366 cm^{-1} with $I_G/I_{G'} \sim 1.07$ and $I_D/I_G \sim 0.45$ intensity ratios.

FWHM value of G' band value is $\sim 58 \text{ cm}^{-1}$ (Figure 4.41).

Due to the lightening problem, etched parts of the GRP372 sample couldn't be observed by optical microscopy. But from non-etched region, Raman spectrum was obtained as shown in Figure 4.42 representing bi-layer graphene characteristics.

For GRP372, G band was located at 1588 cm^{-1} , G' band at 2708 cm^{-1} and D band at 1362 cm^{-1} . Intensity ratios were calculated as $I_G/I_{G'} \sim 0.69$ and $I_D/I_G \sim 0.58$. Symmetric G band with a FWHM of 36 cm^{-1} , is shown in Figure 4.43.

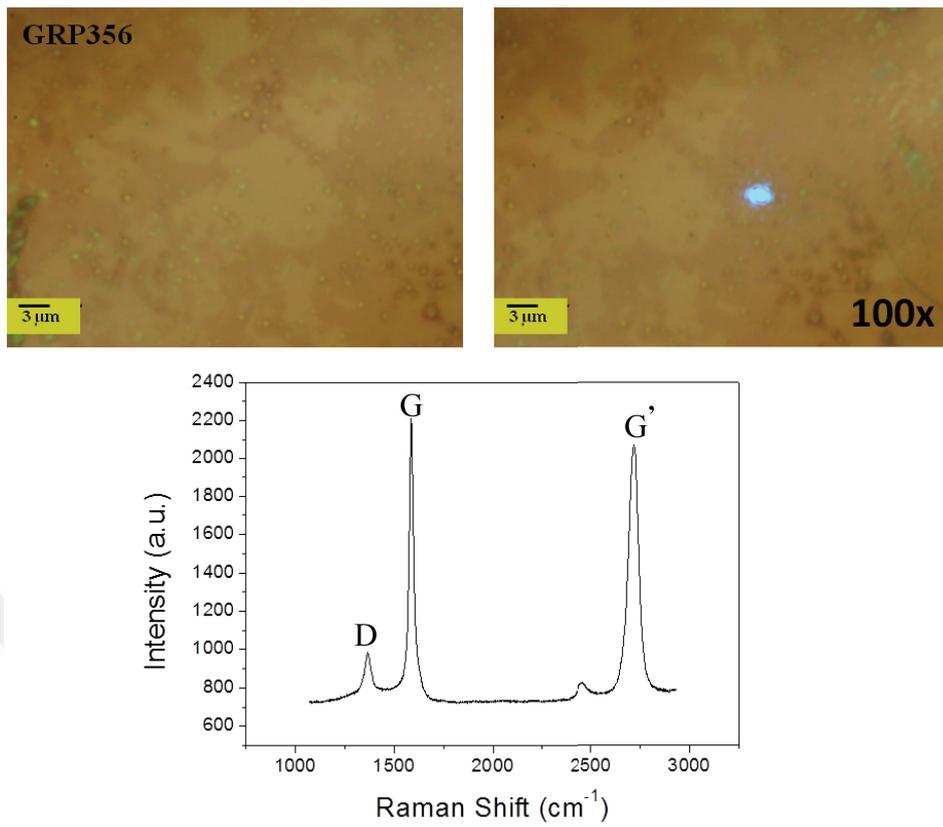


Figure 4.40. Optical Microscopy images with/without laser reflection and Raman Spectrum of GRP356 sample from non-etched area.

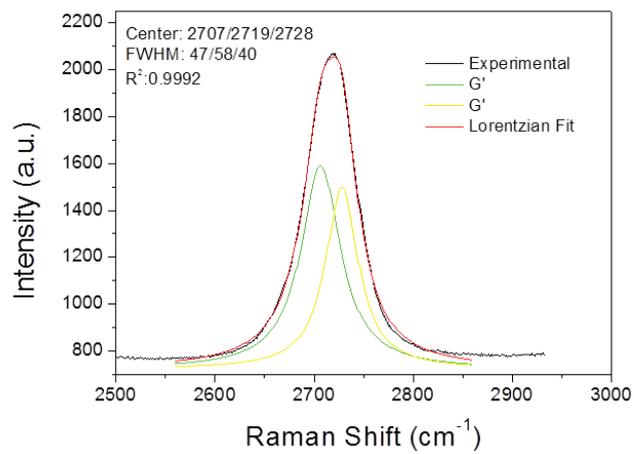


Figure 4.41. G' band Raman spectrum of GRP356 sample that was fitted with two Lorentzian.

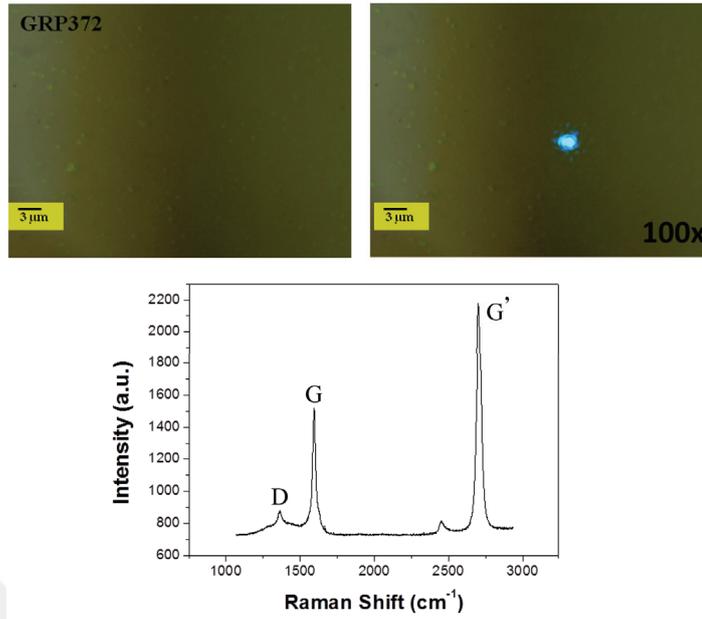


Figure 4.42. Optical Microscopy images with/without laser reflection and Raman Spectrum of GRP372 sample from non-etched area.

Optical microscopy images of GRP373 sample and Raman spectrum that was taken from non-etched region is presented in Figure 4.44. Intensity of G' peak is higher than G peak with the ratio of $I_G/I_{G'} \sim 0.68$ and $I_D/I_G \sim 0.56$. D band is located at 1365 cm^{-1} , G band is at 1592 cm^{-1} and G' band is located at 2709 cm^{-1} .

G' band that was fitted by four Lorentzian is shown in Figure 4.45. FWHM value was found as 33 cm^{-1} .

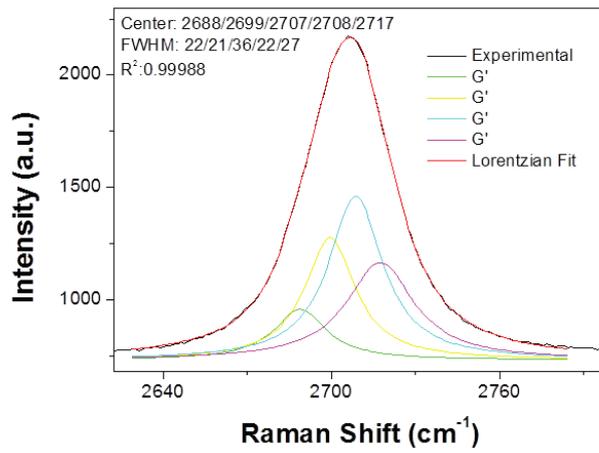


Figure 4.43. G' band Raman spectrum of GRP372 sample that was fitted with four Lorentzian.

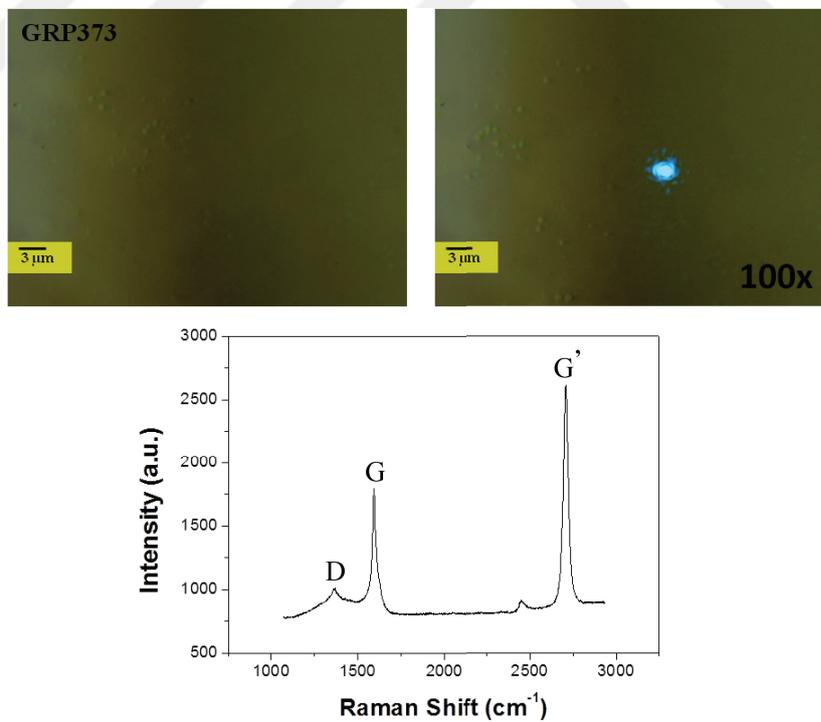


Figure 4.44. Optical Microscopy images with/without laser reflection and Raman Spectrum of GRP373 sample from non-etched area.

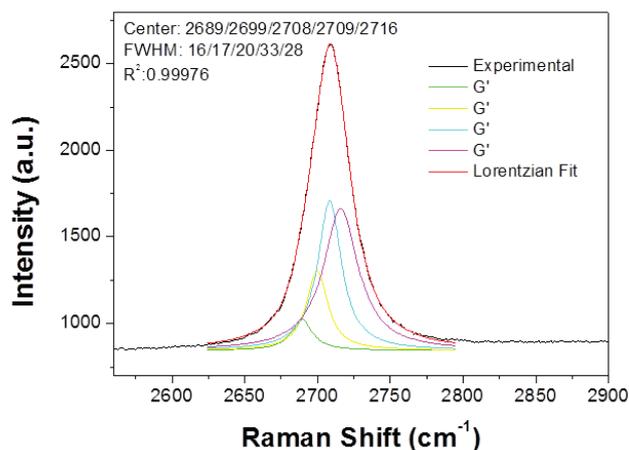


Figure 4.45. G' band Raman spectrum of GRP373 sample that was fitted with four Lorentzian.

Raman spectrum of etched region of GRP373 sample is shown in Figure 4.46. Peak located at 1450 cm^{-1} probably arises from PMMA residuals and step arises from electrical signal noises.

Raman spectrum of GRP379 taken from regions with lighter contrast is shown in Figure 4.47. As seen from the spectrum, there is no any graphitic peaks and graphene is completely etched at these sites.

Raman spectrum that is obtained from the darker regions is presented in Figure 4.48. At these non-etched regions bi-layer graphene characteristics are observed.

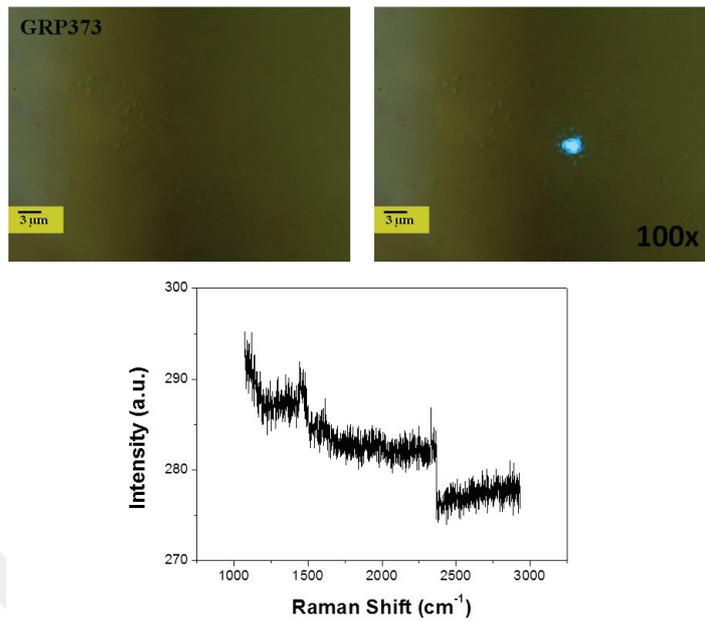


Figure 4.46. Optical Microscopy images with/without laser reflection and Raman Spectrum of GRP373 sample from etched area.

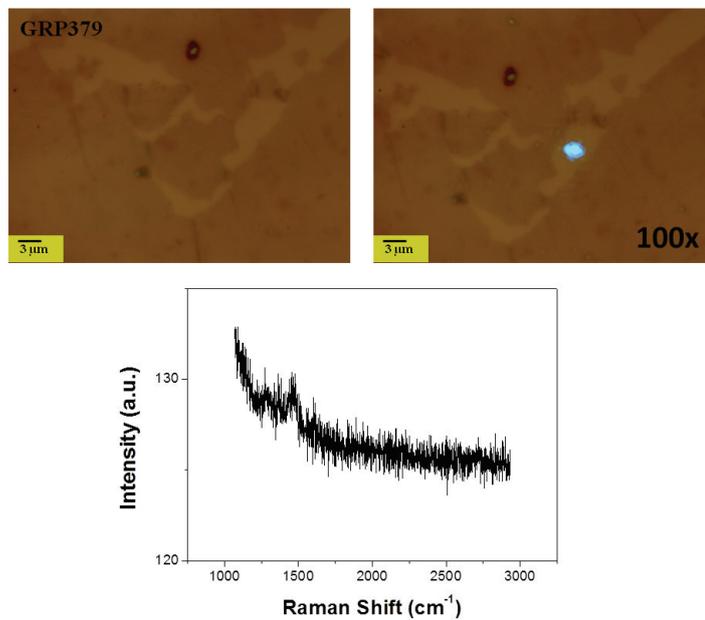


Figure 4.47. Optical Microscopy images with/without laser reflection and Raman Spectrum of GRP379 sample from etched area.

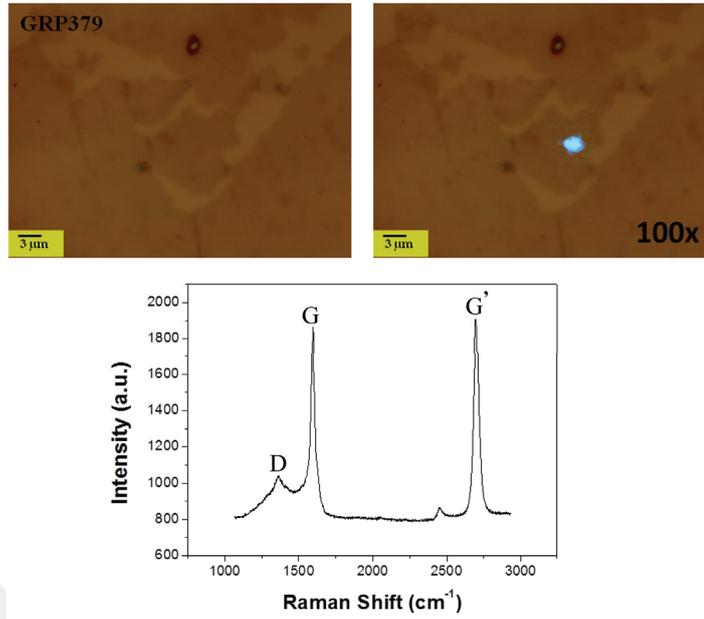


Figure 4.48. Optical Microscopy images with/without laser reflection and Raman Spectrum of GRP379 sample from non-etched area.

GRP379 sample's G band located at 1591 cm^{-1} , G' band at 2700 cm^{-1} , and D band is located at 1360 cm^{-1} . Intensity ratios are found as; $I_G/I_{G'} \sim 0.98$.

G' band of GRP379 that was fitted by four Lorentzian is shown in Figure 4.49. FWHM value was found as 39 cm^{-1} .

GRP380 sample's non-etched region gives Raman spectrum with G band located at 1603 cm^{-1} , G' band at 2709 cm^{-1} , and D band is located at 1363 cm^{-1} . Intensity ratios are found as; $I_G/I_{G'} \sim 0.97$, $I_D/I_G \sim 0.70$ (Figure 4.50).

While darker regions are composed of few-layer graphene, lighter regions are composed of bi-layer graphene as shown in Figure 4.50. Few-layer GRP380 spectrum was fitted by two Lorentzians as shown in Figure 4.51. G' band has FWHM at 37 cm^{-1} .

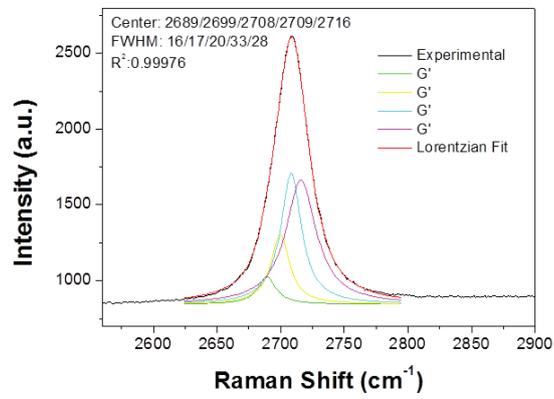


Figure 4.49. G' band Raman spectrum of GRP379 sample that was fitted with four Lorentzian.

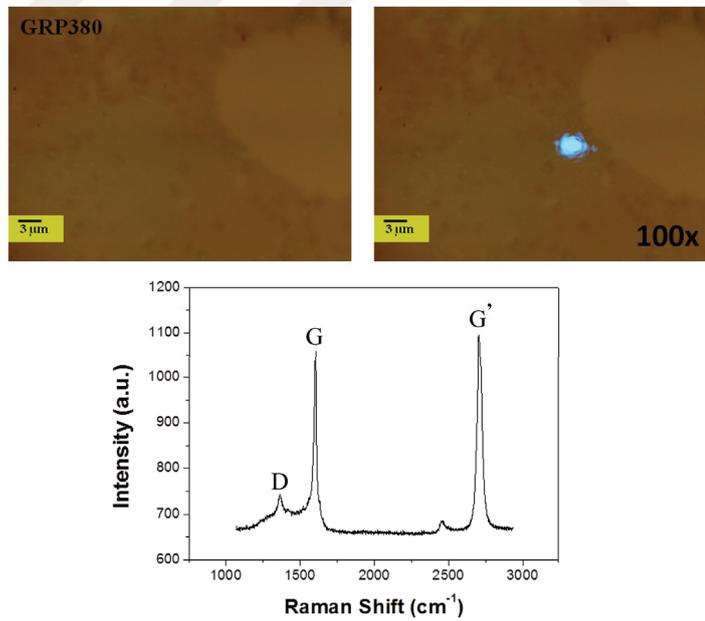


Figure 4.50. Optical Microscopy images with/without laser reflection and Raman Spectrum of GRP380 sample from non-etched area.

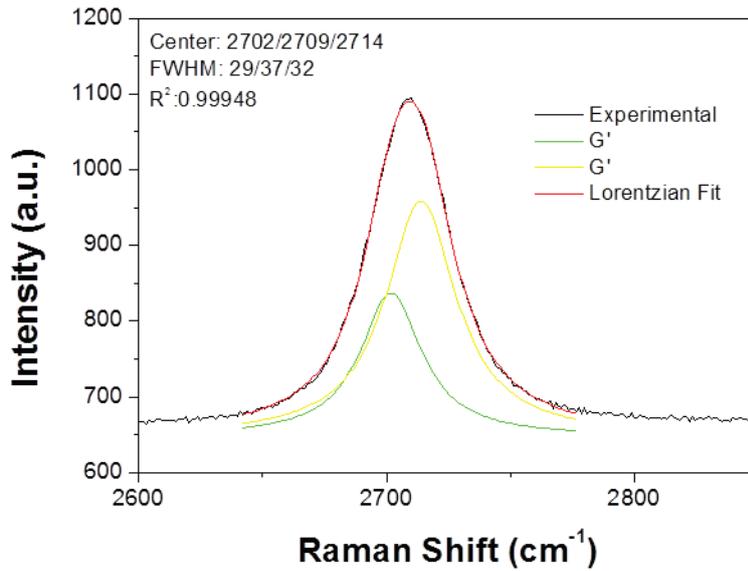


Figure 4.51. G' band Raman spectrum of GRP380 sample that was fitted with two Lorentzian.

Bi-layer GRP380 sample's Raman spectrum is shown in Figure 4.52 that G band is located at 1600 cm^{-1} , G' is at 2707 cm^{-1} , and D band is at 1365 cm^{-1} . Intensity ratios are $I_G/I_{G'} \sim 0.92$, $I_D/I_G \sim 0.84$.

Bi-layer GRP380 sample's spectrum was fitted by four Lorentzians and FWHM is found as 42 cm^{-1} as shown in Figure 4.53.

GRP381 sample's optical images are very consistent with SEM images. It is seen that etching was occurred fractionally. Etched parts show lightest contrast (Figure 4.54), bi-layer regions give middle contrast and few-layer regions give darker contrast (Figure 4.55).

Bi-layer regions of GRP381 sample give G band at 1605 cm^{-1} , G' band at 2709 cm^{-1} and D band at 1364 cm^{-1} as seen in Figure 4.55.

In Figure 4.56, symmetric G' band has FWHM value of 35 cm^{-1} for bi-layer GRP381.

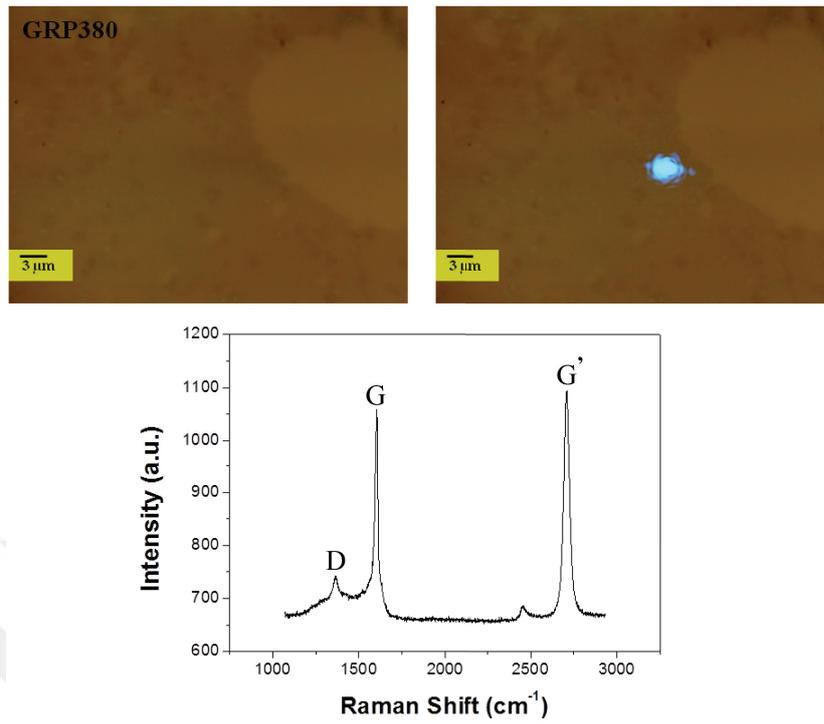


Figure 4.52. Optical Microscopy images with/without laser reflection and Raman Spectrum of GRP380 sample from etched area.

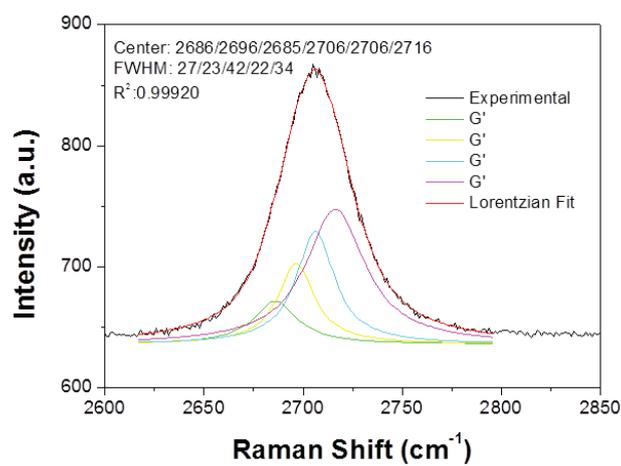


Figure 4.53. G' band Raman spectrum of GRP380 sample that was fitted with four Lorentzian.

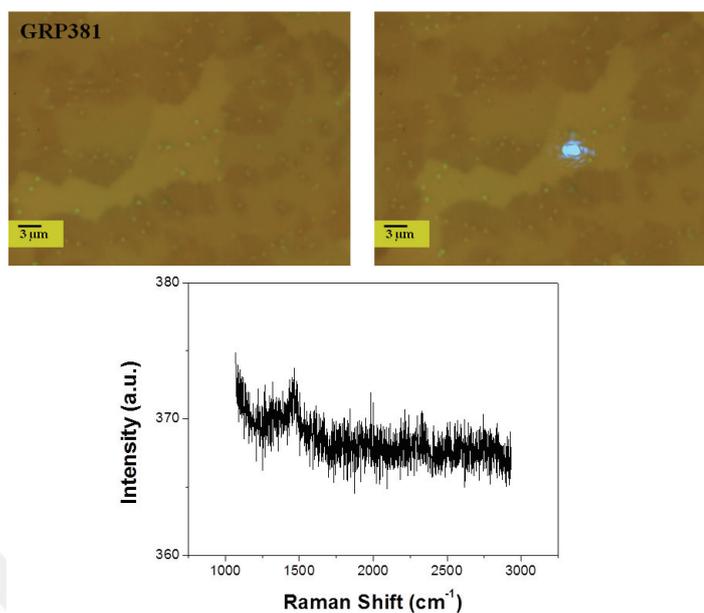


Figure 4.54. Optical Microscopy images with/without laser reflection and Raman Spectrum of GRP381 sample from etched area.

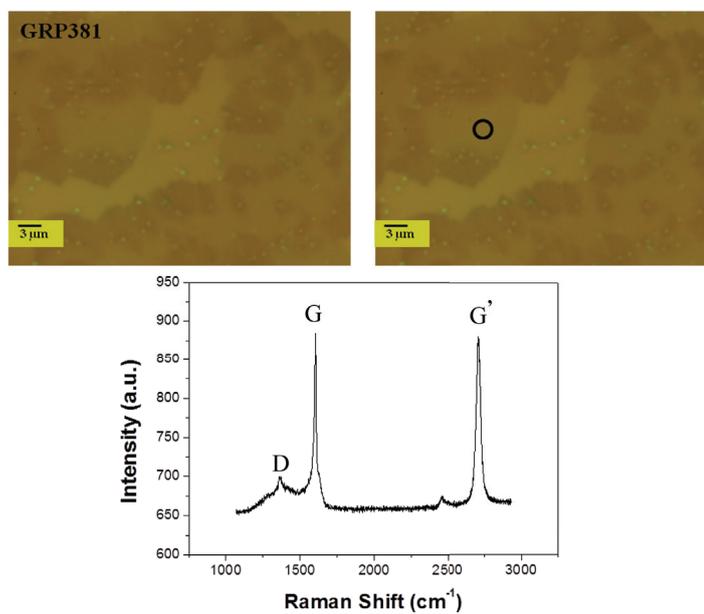


Figure 4.55. Optical Microscopy images with/without laser reflection and Raman Spectrum of GRP381 sample from non-etched area.

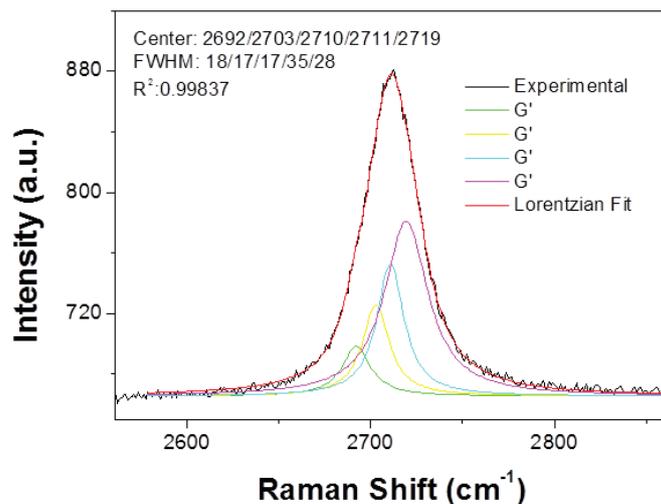


Figure 4.56. G' band Raman spectrum of GRP381 sample that was fitted with four Lorentzian.

Some of the prepared graphene films were also transferred onto gold quartz crystals in order to achieve initial gas sensing experiments using QCM technique.

Optical microscopy images and Raman spectrum of empty gold quartz crystal are shown in Figure 4.57.

As the Raman spectrum was taken from the gold region, the fluorescence effect is observed as inclined plot. Therefore, this effect is ignored and substrate baseline was subtracted from the obtained Raman spectrum results for other graphene transferred QCM substrates.

GRP353 sample was grown on Cu foil under 5 sccm CH_4 , 20 sccm H_2 and 200 sccm Ar gas flows at 1073 °C and etching was carried on at the same temperature under 200 sccm H_2 and 200 sccm Ar gas flows. H_2 etching increases defect sides on graphene and etching occurs along these sides. Optical microscopy images and subtracted Raman spectrum of transferred GRP353 sample on gold quartz crystal are presented in Figure 4.58.

GRP403 sample was grown under 10 sccm C_2H_4 , 100 sccm Ar and 10 sccm H_2 gas flows with 1 Torr pressure on Cu foil. Optical microscopy images and subtracted Raman Spectrum of transferred GRP403 sample on gold quartz crystal is shown in Figure 4.59.

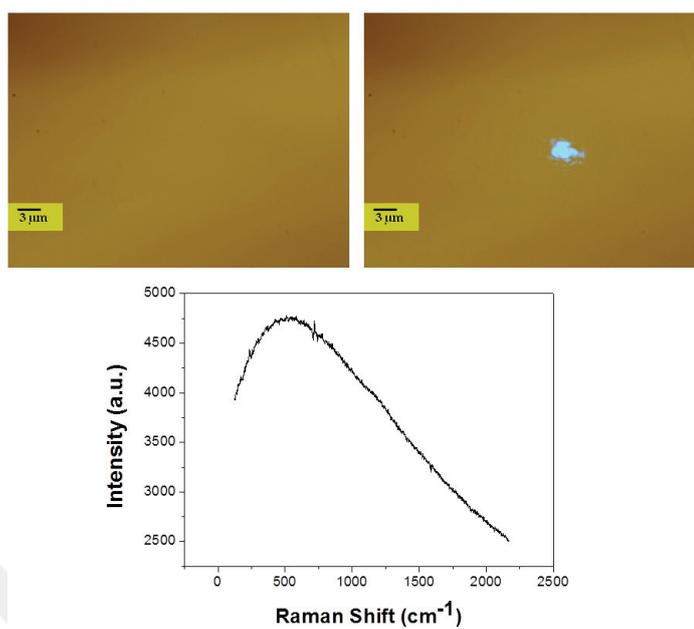


Figure 4.57. Optical Microscopy images with/without laser reflection and Raman Spectrum of empty gold quartz crystal.

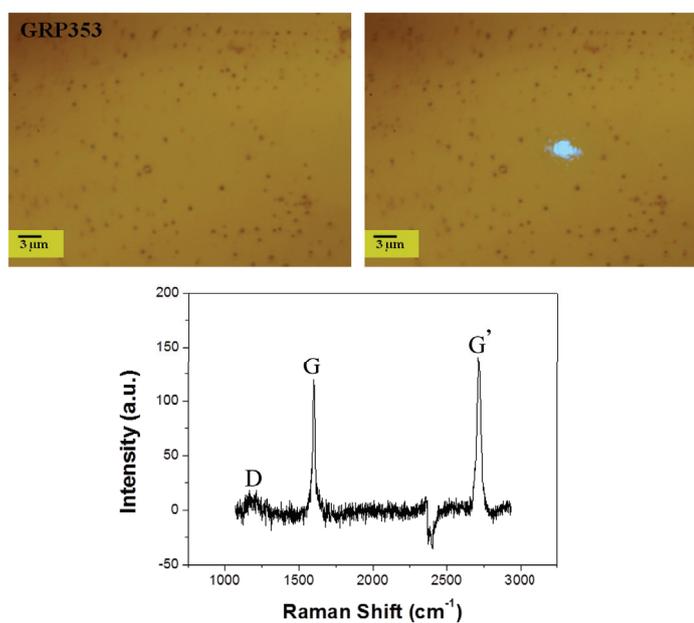


Figure 4.58. Optical Microscopy images with/without laser reflection and Raman Spectrum of GRP353 sample on gold quartz crystal.

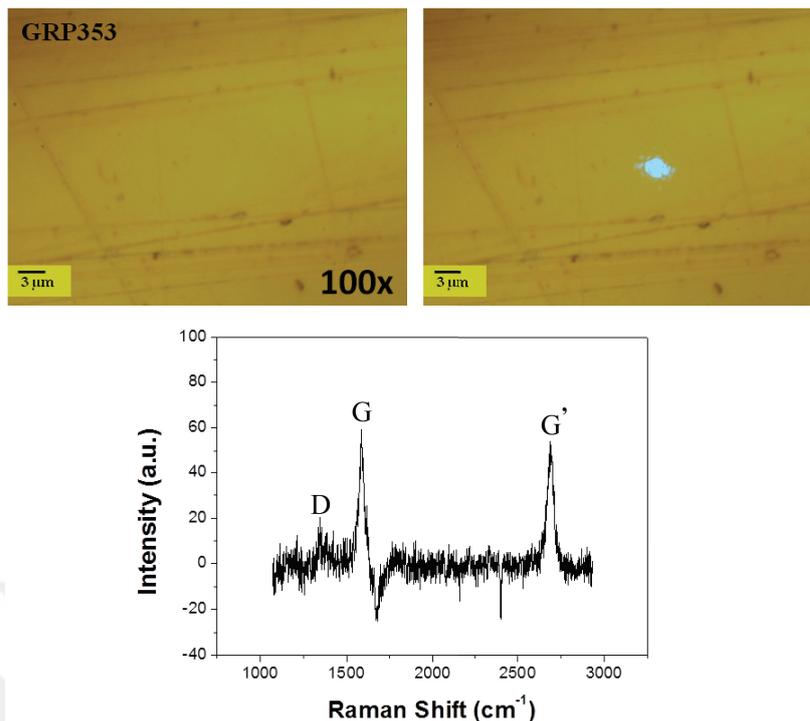


Figure 4.59. Optical Microscopy images with/without laser reflection and Raman Spectrum of GRP403 sample on gold quartz crystal.

GRP352 sample was grown on Cu foil under 5 sccm CH_4 , 20 sccm H_2 and 200 sccm Ar gas flows at 1073 °C and transferred on to gold quartz crystal. Optical microscopy images and Raman spectrum that is shown in Figure 4.60 belong to GRP352 on gold quartz crystal.

Optical microscopy images of GRP414 with and without laser reflection with 100x magnifications are shown in Figure 4.61. Raman spectrum of the non-etched region is showed graphitic characteristics with few layer structures.

Raman spectrum of GRP429 sample that was obtained from the lighter and etched regions are presented in Figure 4.62. These regions are composed of bi-layer graphene.

According to Figure 4.63, darker regions of GRP429 have multi-layer graphene characteristics.

Raman spectrum of etched GRP438 sample taken from darker regions show bi-layer graphene structures (Figure 4.64).

Lighter, thus, etched regions give no any graphitic peaks supporting a successful etching process as shown in Figure 4.65.

GRP441 sample was grown on Cu foil under 5 sccm CH_4 , 20 sccm H_2 and 200

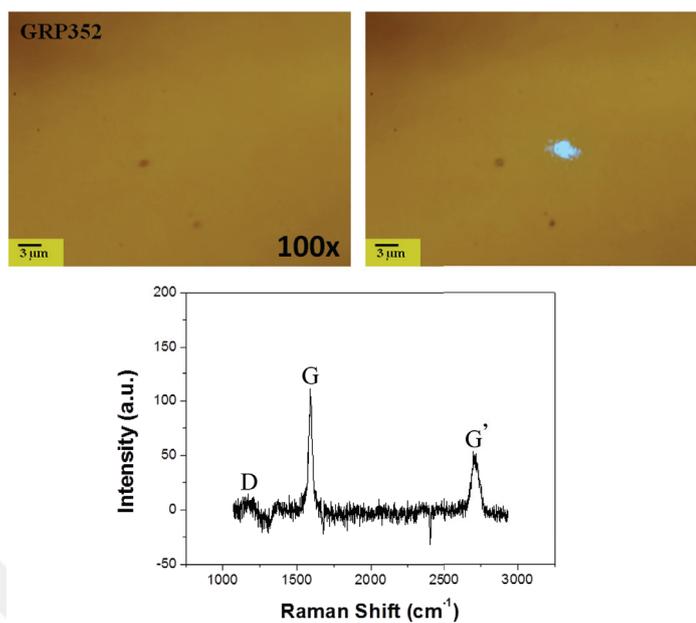


Figure 4.60. Optical Microscopy images with/without laser reflection and Raman Spectrum of GRP352 sample on gold quartz crystal.

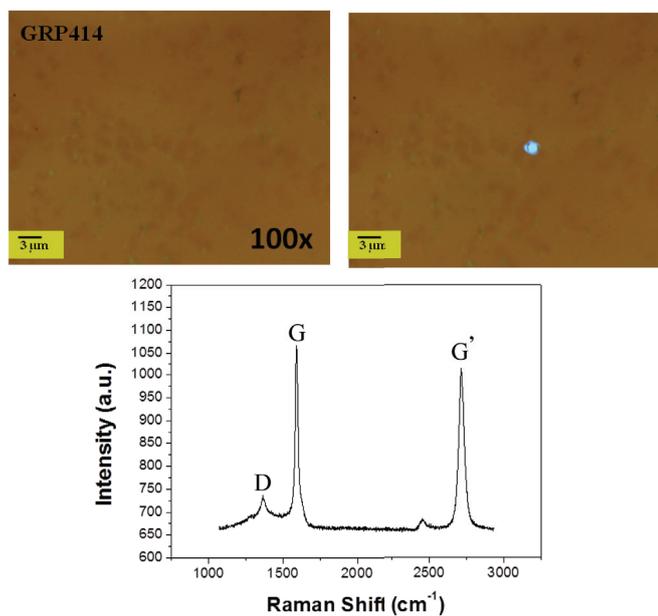


Figure 4.61. Optical Microscopy images with/without laser reflection and Raman Spectrum of GRP414 sample from non-etched area.

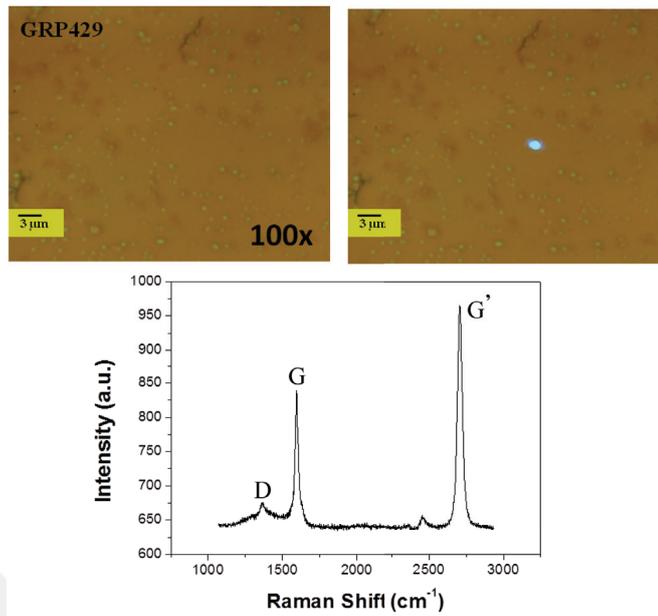


Figure 4.62. Optical Microscopy images with/without laser reflection and Raman Spectrum of GRP429 sample from etched area.

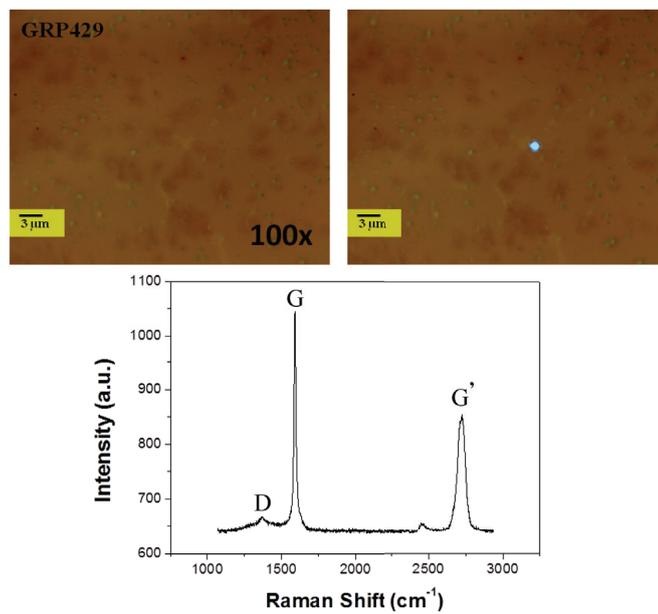


Figure 4.63. Optical Microscopy images with/without laser reflection and Raman Spectrum of GRP429 sample from non-etched area.

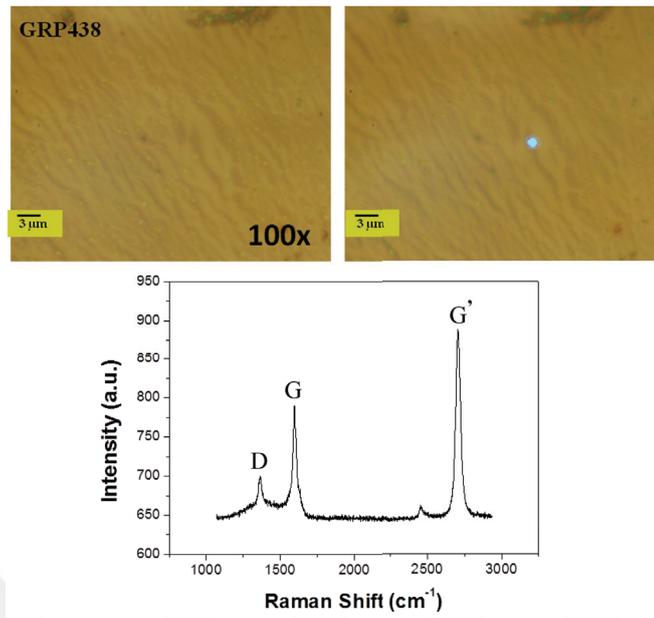


Figure 4.64. Optical Microscopy images with/without laser reflection and Raman Spectrum of GRP438 sample from non-etched area.

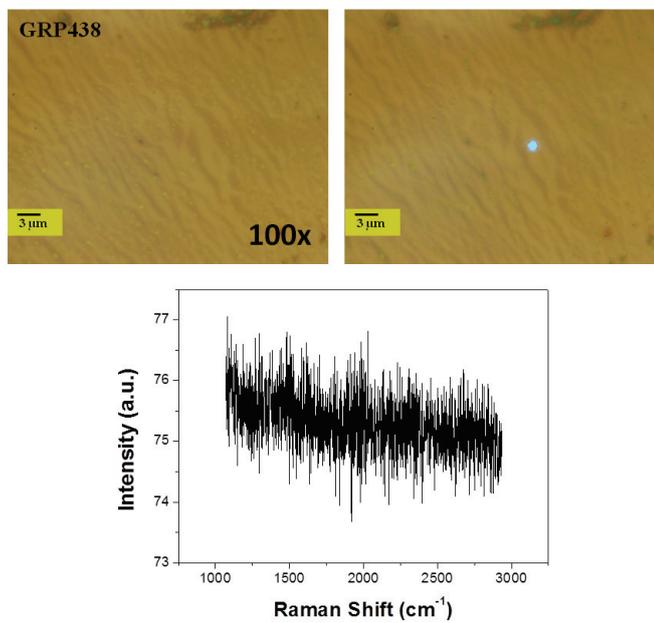


Figure 4.65. Optical Microscopy images with/without laser reflection and Raman Spectrum of GRP438 sample from etched area.

sccm Ar gas flows at 1073 °C for 3 min and etched under 150 sccm H₂ and 800 sccm Ar gas flows for 40 min. While the Raman spectrum of darker regions show multi-layer graphene characteristics in Figure 4.66, lighter regions show bi-layer characteristics (Figure 4.67).

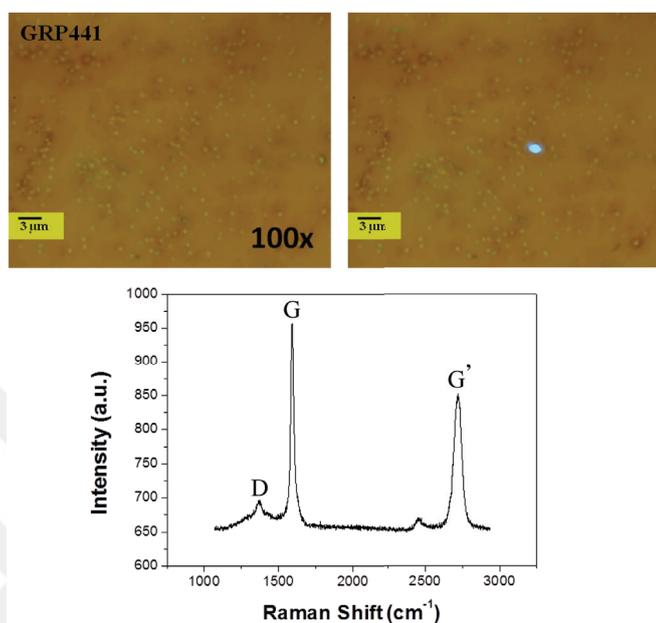


Figure 4.66. Optical Microscopy images with/without laser reflection and Raman Spectrum of GRP441 sample from non-etched area.

Grown and etched GRP428 and GRP439 samples were also transferred onto quartz crystals for gas sensing measurements. Raman spectrum of transferred GRP428 on QCM showed graphitic peaks with supporting successful transfer process in Figure 4.68.

Figure 4.69 shows optical image and Raman spectrum of transferred GRP439 sample. Again graphitic peaks are presented confirming graphene existence.

Optical image and Raman spectrum of GRP485 taken from the lighter region is presented in Figure 4.70. The lighter regions are completely etched and show no any graphitic characteristics.

Raman spectrum obtained from non-etched part of the GRP485 sample is shown in Figure 4.71. Non-etched regions of GRP485 sample show bi-layer graphene characteristics.

Raman spectrum taken from the etched regions of GRP486 sample is shown in Figure 4.72.

Raman spectrum taken from the lightest region shows no any graphitic peaks.

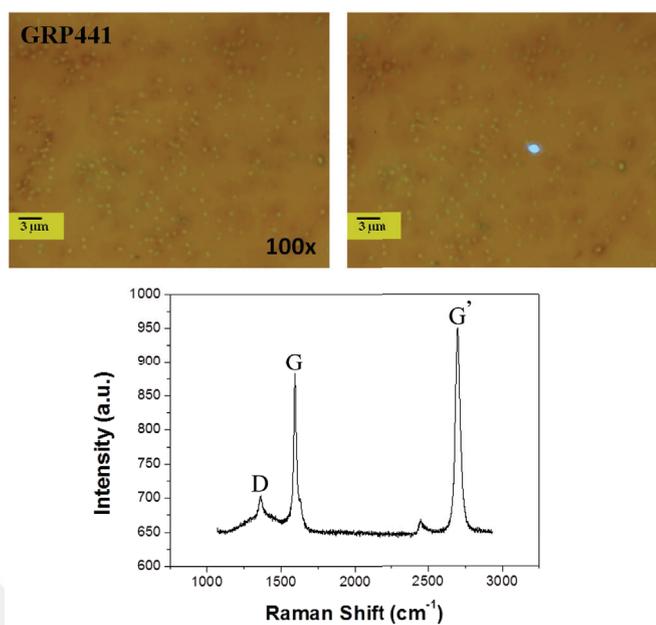


Figure 4.67. Optical Microscopy images with/without laser reflection and Raman Spectrum of GRP441 sample from etched area.

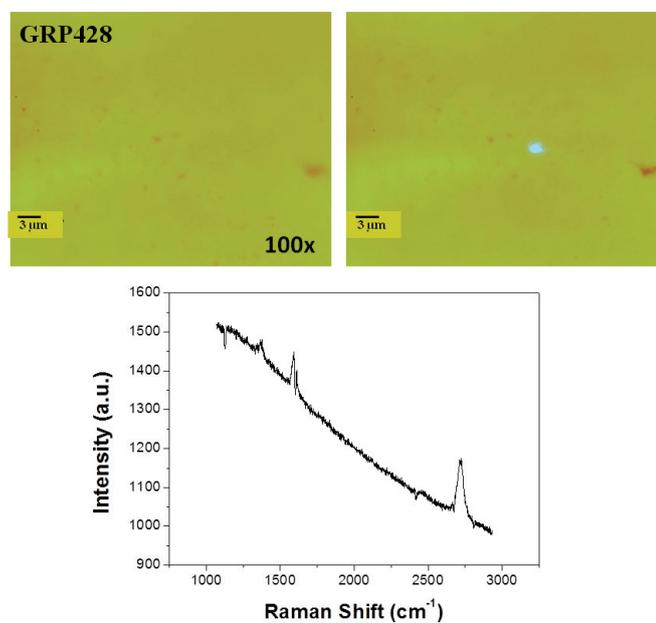


Figure 4.68. Optical Microscopy images with/without laser reflection and Raman Spectrum of GRP428 sample on quartz crystal.

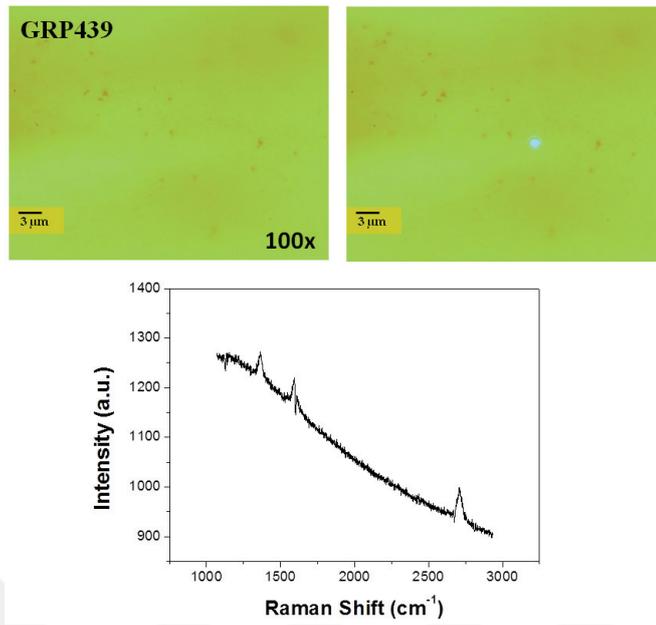


Figure 4.69. Optical Microscopy images with/without laser reflection and Raman Spectrum of GRP439 sample on quartz crystal.

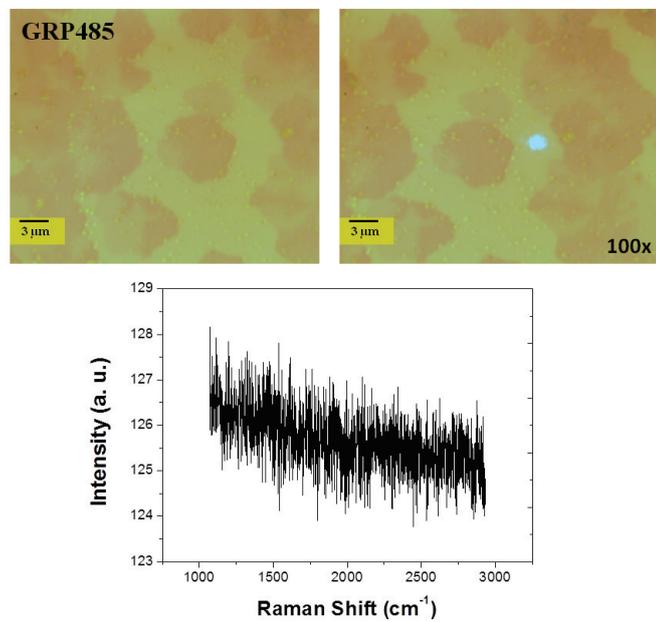


Figure 4.70. Optical Microscopy images with/without laser reflection and Raman Spectrum of GRP485 sample from etched region.

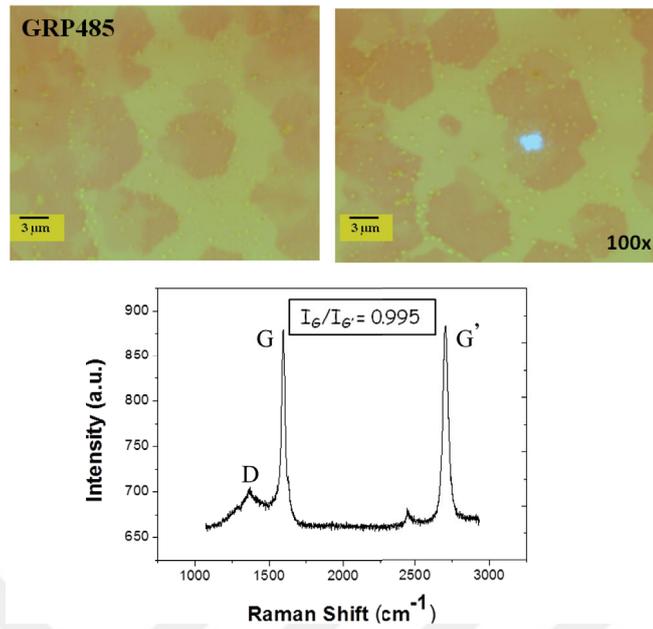


Figure 4.71. Optical Microscopy images with/without laser reflection and Raman Spectrum of GRP485 sample from non-etched region.

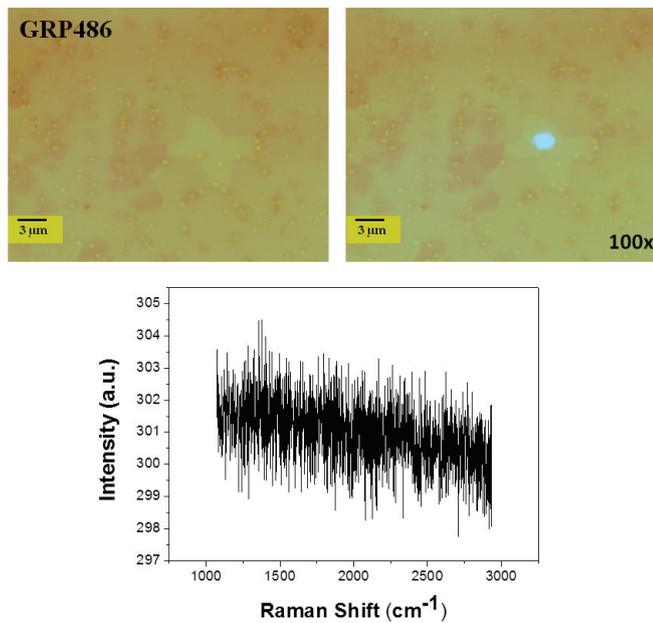


Figure 4.72. Optical Microscopy images with/without laser reflection and Raman Spectrum of GRP486 sample from etched region.

These regions are completely etched regions.

Raman spectrum taken from middle-lightened region is presented in Figure 4.73. These regions are mostly composed of mono-layer and bi-layer graphene structures.

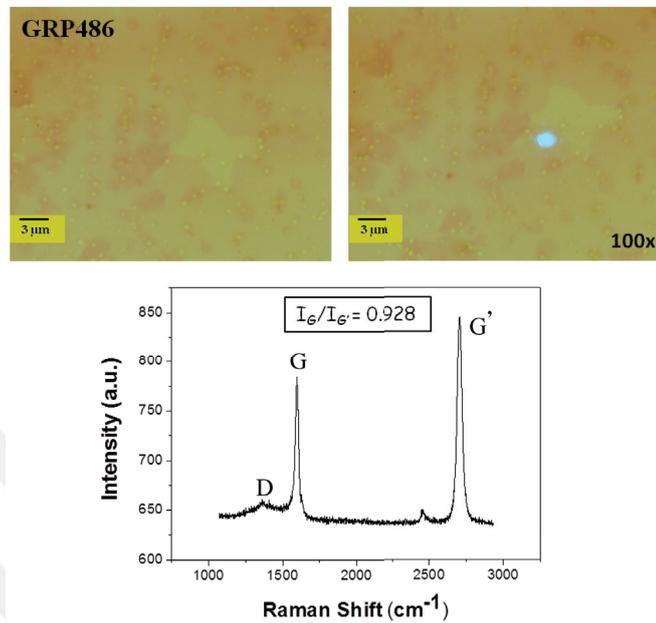


Figure 4.73. Optical Microscopy images with/without laser reflection and Raman Spectrum of GRP486 sample from middle-lightened region.

Raman spectrum obtained from the darker sides of the GRP486 is shown in Figure 4.74. And these regions are composed of few-layered graphene flakes.

Raman spectrum of GRP463 sample that was taken from the gap between two electrodes is shown in Figure 4.75.

Raman spectrum of GRP463 shows few layer graphene characteristics with some impurity effects.

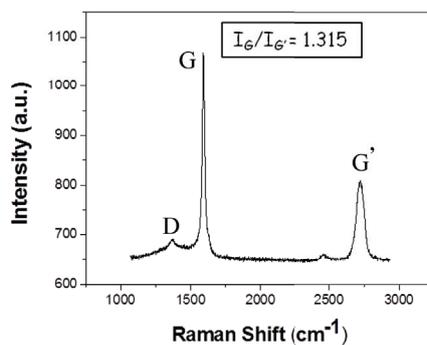
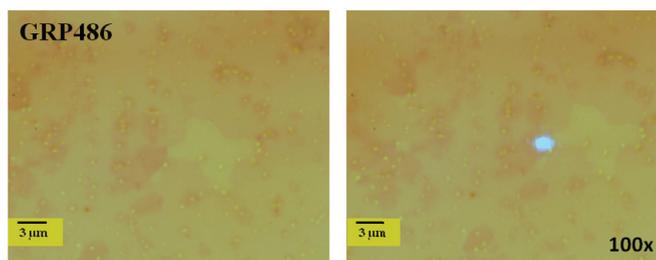


Figure 4.74. Optical Microscopy images with/without laser reflection and Raman Spectrum of GRP486 sample from darkest region.

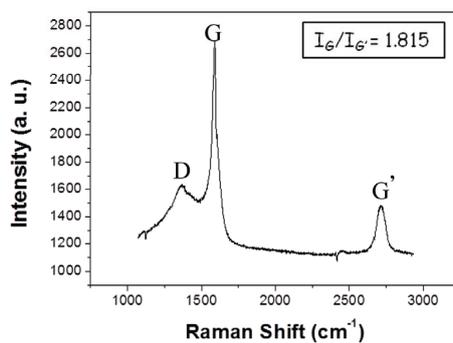
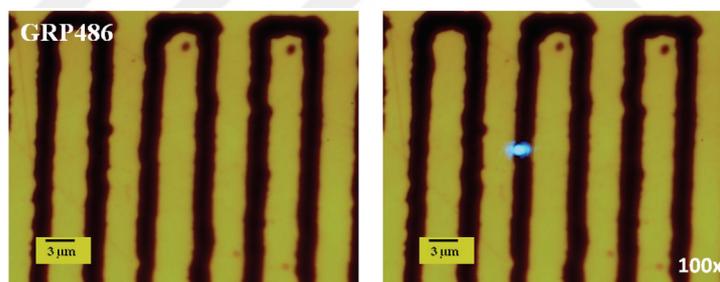


Figure 4.75. Optical Microscopy images with/without laser reflection and Raman Spectrum of GRP463 sample taken from the gap between two electrodes. Laser can be seen as bright spot in between the two electrodes.

4.2.2. Kelvin Probe Force Microscopy (KPFM) Results

In our study, we used KPFM technique to investigate the SAM modification on graphene film surface. We used conductive TiN AFM tip and with the surface potential difference is defined as the ratio of the work function difference of sample and the tip to electric charge e Kumar et al. (2016). Figure 4.76 indicates the contact potential difference curves of bare GRP, DPIFA modified GRP, MePIFA modified GRP and HOPG sample that is used as reference sample. The measured surface potential values of bare GRP, DPIFA modified GRP and MePIFA modified GRP samples are obtained as 0.103 V, 0.020 V and 0.149V, respectively. Work function, the minimum energy needed to remove an electron from the surface of a material, of the samples can be calculated by the relation Yu et al. (2016);

$$W = 4.475 + \Delta W_{sample} - \Delta W_{HOPG} \quad (4.1)$$

where ΔW_{HOPG} is the work function difference between HOPG and AFM tip. According to our measurements we found ΔW_{HOPG} as 0.244 V and calculate the work function's of the bare GRP, DPIFA modified GRP and MePIFA modified GRP as 4.13 eV, 4.25 eV and 4.38 eV, respectively.

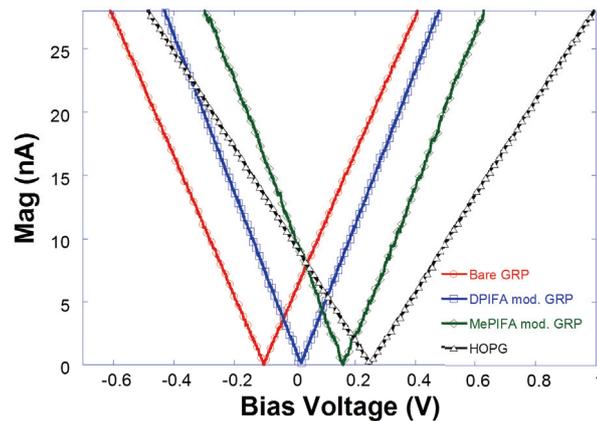


Figure 4.76. Contact potential differences of bare GRP, modified GRP with MePIFA - DPIFA SAMs and HOPG.

These results indicate the SAM modification where MePIFA modified sample has higher work function and surface potential. As the SAM modified samples have positive

contact potentials, we can say that these functionalizations led to p-type doping which also makes surface more attractive for gas molecule adsorption.

4.3. Sensorial Characterization

Sensorial characterizations are indicated with QCM and amperometric measurements in CO, CO₂, NH₃ and humid ambient.

4.3.1. Quartz Crystal Microbalance (QCM) Results

CO and CO₂ measurements are discussed together under same subsection and NH₃ and humidity measurements in the next subsection.

4.3.1.1. CO and CO₂ Sensing

As initial gas detection experiments; four graphene films with different properties were transferred on to gold quartz crystals and the frequency changes upon gas molecule absorption measured under carbon monoxide (CO) and carbon dioxide (CO₂) gas flows. Dry air (DA) flow was used as remover gas.

GRP353, CVD-reverse reaction etched sample, was transferred onto gold crystal and frequency changes were detected under periodic 500 sccm CO and 500 sccm DA gas flows during 200 sec for each step as seen in Figure 4.77. In the first periodic interval of CO exposure, CO molecules bound to graphene surface probably form etched parts and made chemical bounding. With the second DA flow, bounded CO molecules couldn't released completely and no significant change observed in frequency shift. At the second CO interval, molecules continued to bound surface.

The same GRP353 coated QCM sample was then exposed to periodic DA - CO₂ flows with 1000 sccm flow amounts during 200 sec intervals at each. Obtained frequency change plot is shown in Figure 4.78.

As the same sample was used in CO detection, there was still CO molecules on the surface thus with the DA flow, molecules released from the surface and positive frequency change observed. With the CO₂ exposure, CO₂ molecules absorbed and due to mass

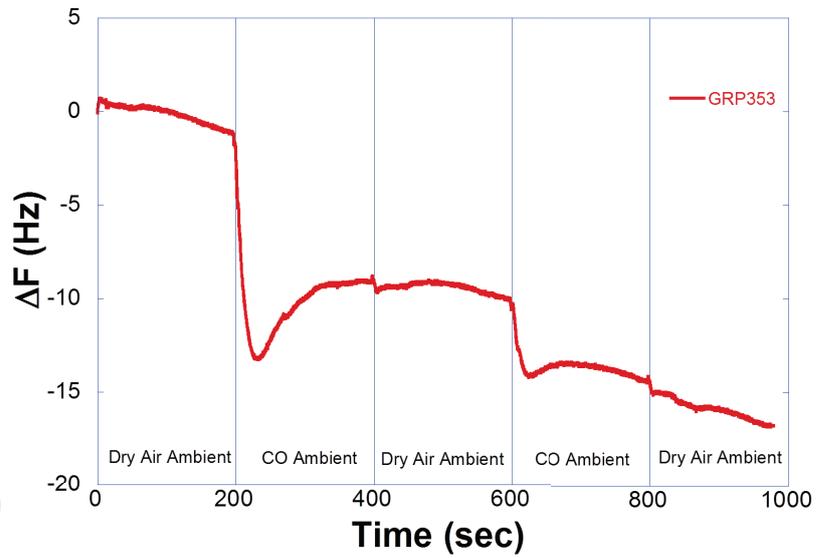


Figure 4.77. Frequency change vs. time plot of GRP353 under periodic DA - CO gas flows.

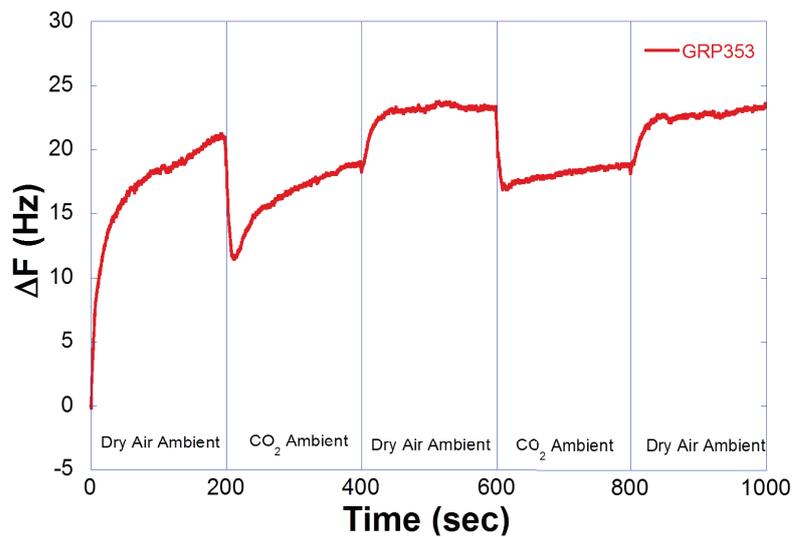


Figure 4.78. Frequency change vs. time plot of GRP353 under periodic DA - CO₂ gas flows.

increment, frequency decreased. Reversible process of the sample showed good response to CO₂ molecules as gas sensing device.

GRP403 sample that was grown with C₂H₄ flow was also transferred on to another QCM substrate and frequency change was recorded under DA - CO and DA - CO₂ exposures. However, as QCM crystal was heavily deformed due to over usage, interpretable data couldn't be achieved (Figure 4.79).

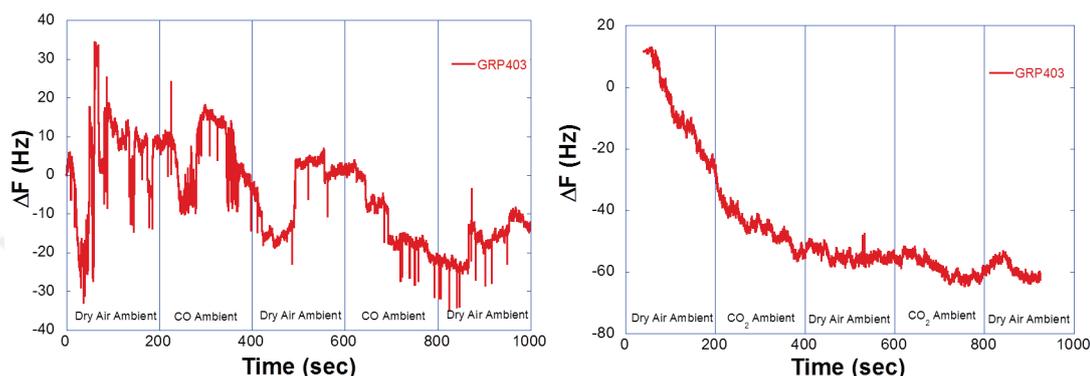


Figure 4.79. Frequency change vs. time plot of GRP403 under periodic DA - CO and DA - CO₂ gas flows.

Frequency change of GRP352 sample that was grown with CH₄ flow transferred on QCM crystal due to DA - CO gas exposures under 1000 sccm flow amount is presented in Figure 4.80. Sample showed little response to DA - CO gas exposures. Positive frequency shift based on gas molecule release is also observed for this sample.

GRP352 coated QCM was also tested under periodic DA - CO₂ exposures. When compared with its CO response, sensor gave more distinct response to CO₂ exposure with the CO₂ absorption (Figure 4.81).

The frequency change of the pristine graphene and Me-PIFA modified graphene under periodic 1000 sccm N₂ - CO gas flows for 200 sec. time intervals are shown in Figure 4.82. The pristine graphene had smooth changes due to gas flow periods and it showed decaying behavior. This trend may be explained with the chemical bonding formation of gas molecules on graphene surface; however, for sensor applications this situation couldn't be intended. A successful sensor should absorb target gas molecules physically and during the purifier gas flow, this absorbed molecules should be released back. For our measurements, reversible and repeatable trend couldn't be achieved with pristine graphene samples. Therefore, we used SAM molecules to modify graphene sensor and make them more available for sensor applications. As showed in Figure 4.82,

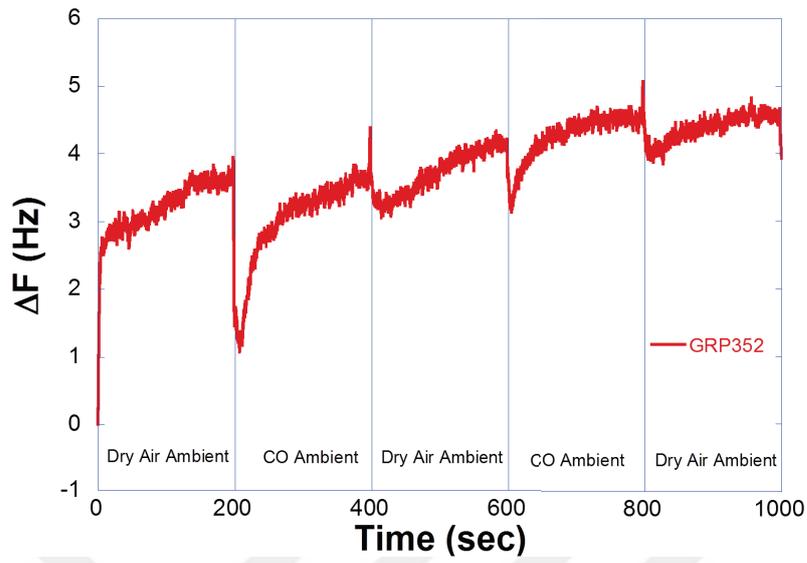


Figure 4.80. Frequency change vs. time plot of GRP352 under periodic DA - CO gas flows.

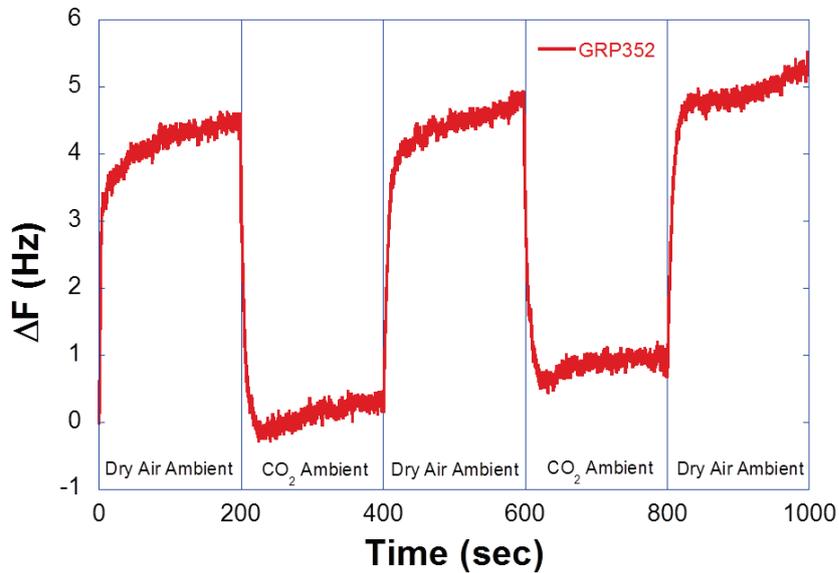


Figure 4.81. Frequency change vs. time plot of GRP352 under periodic DA - CO₂ gas flows.

Me-PIFA modified graphene sample gave more significant response under CO gas flows and with the N₂ gas flow, absorbed molecules were released back.

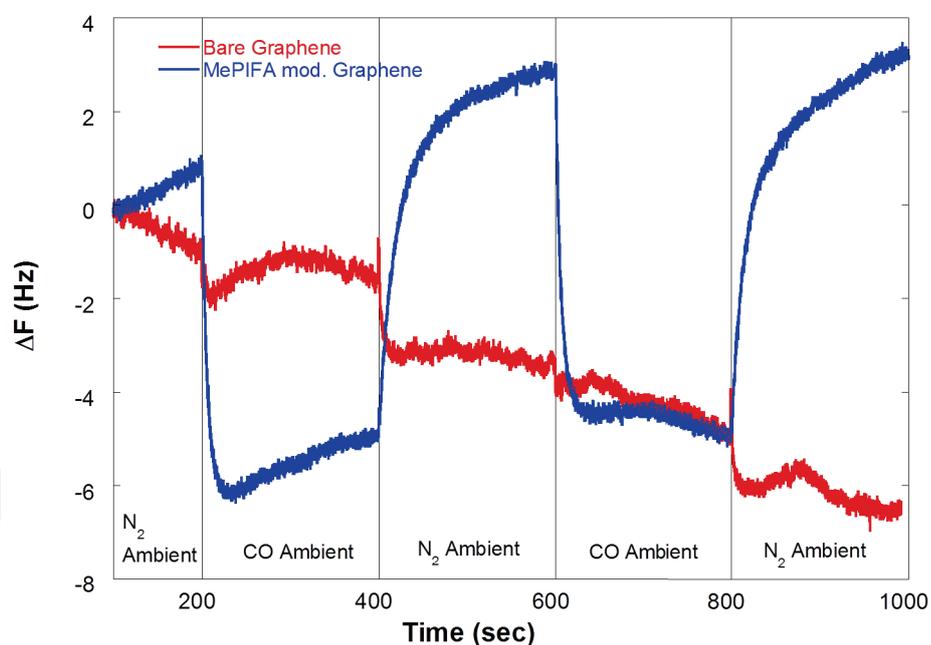


Figure 4.82. Frequency change of pristine and Me-PIFA modified graphene under periodic N₂ - CO gas flows.

The same measurement was also carried on with D-PIFA modified graphene samples. Again SAM modification of the graphene was improved the surface properties and device became more appropriate for sensor applications (Figure 4.83).

The frequency change of the pristine graphene, Me-PIFA and D-PIFA modified graphene samples under periodic N₂ - CO₂ gas flows are shown Figure 4.84. Again while the device with pristine graphene made chemically bonding with CO₂ molecules, Me-PIFA and D-PIFA SAMs modified ones gave nearly the same response.

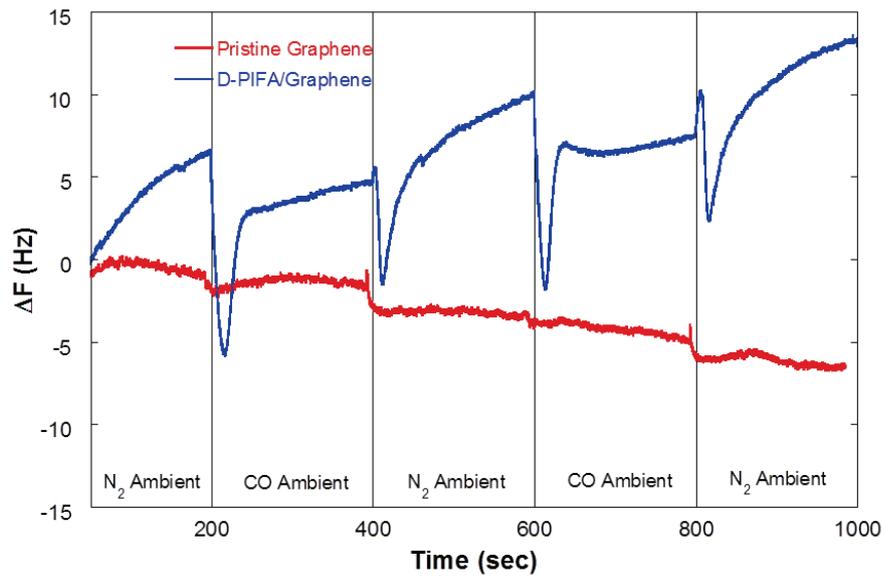


Figure 4.83. Frequency change of pristine and D-PIFA modified graphene under periodic N_2 - CO gas flows.

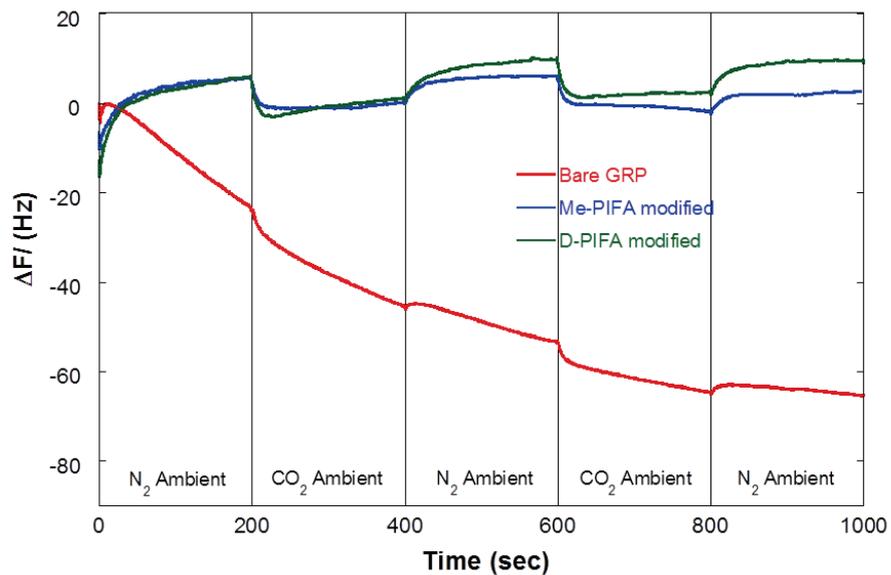


Figure 4.84. Frequency change of pristine, Me-PIFA and D-PIFA modified graphene under periodic N_2 - CO_2 gas flows.

Two CVD H₂ etched graphene samples; GRP429 and GRP438 were also transferred on to the QCM crystals for gas sensing measurements. Both of the graphene samples were grown with the same parameters but while the GRP429 was etched under 150 sccm H₂ for 20 min, GRP438 was etched for 40 min. Frequency change under N₂ - CO gas flows are shown in Figure 4.85. Here we see that, sample with longer etching time had more binding sites rather than the sample with shorter etching time. Reversible and repeatable responses were also achieved by CVD H₂ etching.

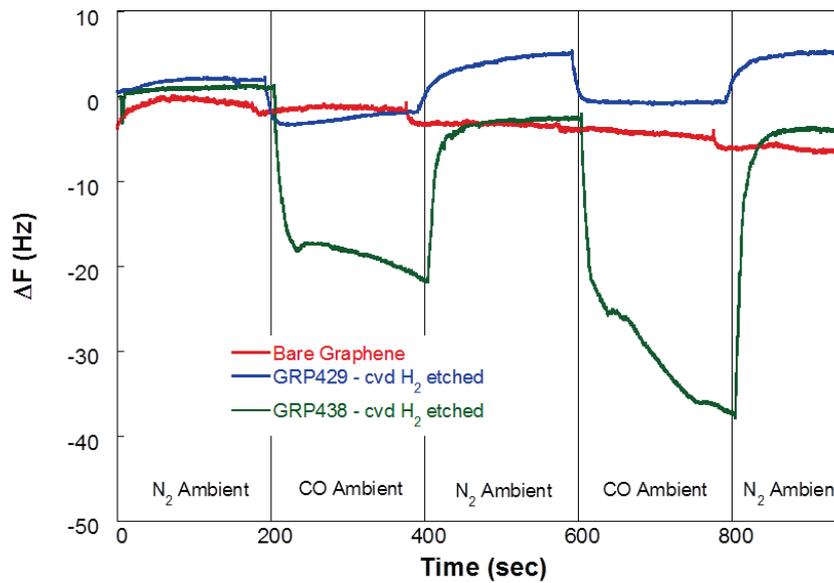


Figure 4.85. Frequency change of pristine, CVD etched GRP429 and GRP438 modified graphene under periodic N₂ - CO₂ gas flows.

4.3.1.2. NH₃ and Humidity Sensing

GRP456 sample was grown with standard growth parameters and transferred from Cu foil to quartz crystal for gas testing experiments. In QCM investigation, as a target gas Ammonia (NH₃) gas was used with 500 sccm amount and to compare device sensitivity at different environments, air and nitrogen (N₂) gases were used as cleaning gases. Humidity also an important parameter and has a significant role in degradation of the device performance. Measured frequency change under investigation is shown in Figure 4.86.

In the Figure 4.86, red circled plot indicates the frequency change during periodic

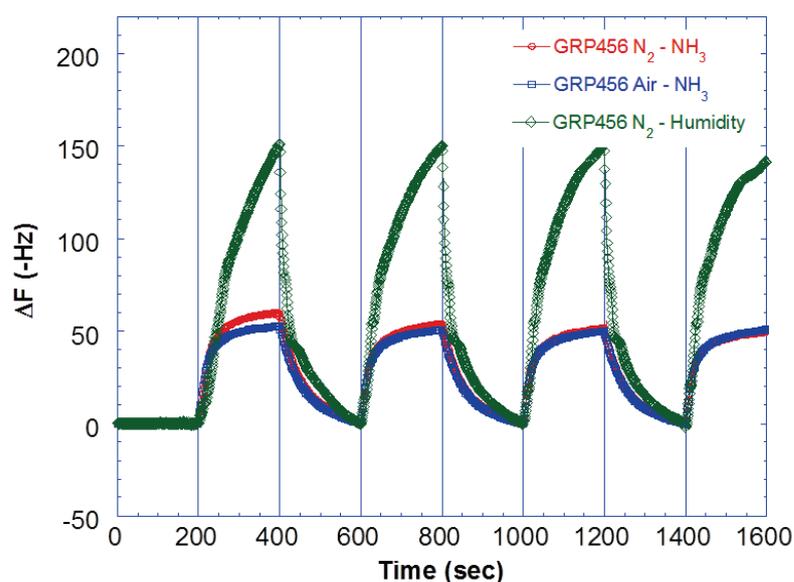


Figure 4.86. Frequency change of GRP456 sample under periodic N₂ - NH₃ (red circles), Air - NH₃ (blue squares) and N₂ - humidity (green quadrangles) gas flows.

N₂ - NH₃ gas flows. Both of the gas amounts were 500 sccm and measurement started with the cleaning gas N₂ flow for 200 sec. Periodicity was carried with 200 sccm NH₃ gas flows for 200 sec. Change intervals were fixed at 200 sec. Blue squares indicate the frequency change during Air - NH₃ gas flows with same periodic conditions with previous N₂ - NH₃ measurements. Green quadrangle indicates the frequency change during N₂ (cleaning gas) and Humidity (target gas) flows. Again the same periodicity and gas amounts were used during the investigation.

GRP456 sample gives nearly the same reaction to NH₃ gas under both of the N₂ and Air environments. But it is more sensitive to humidity rather than target molecule which can be adversely affected the sensing performance of the device at variable humidity environments. Therefore, we used MePIFA and DPIFA SAM molecules to increase the sensitivity of the graphene sensor and also decrease the humidity effect and thus to improve the sensing performance of the device.

GRP439 samples were also grown with standard graphene growth parameters. But after they were transferred on to quartz crystals, one of them was modified in 1 mM MePIFA solution and the other was modified in 1 mM DPIFA solution.

Comparison frequency changes of bare GRP456 sample, MePIFA modified GRP439 sample and DPIFA modified GRP439 samples in periodic N₂ - NH₃ gas flow intervals are shown in Figure 4.87.

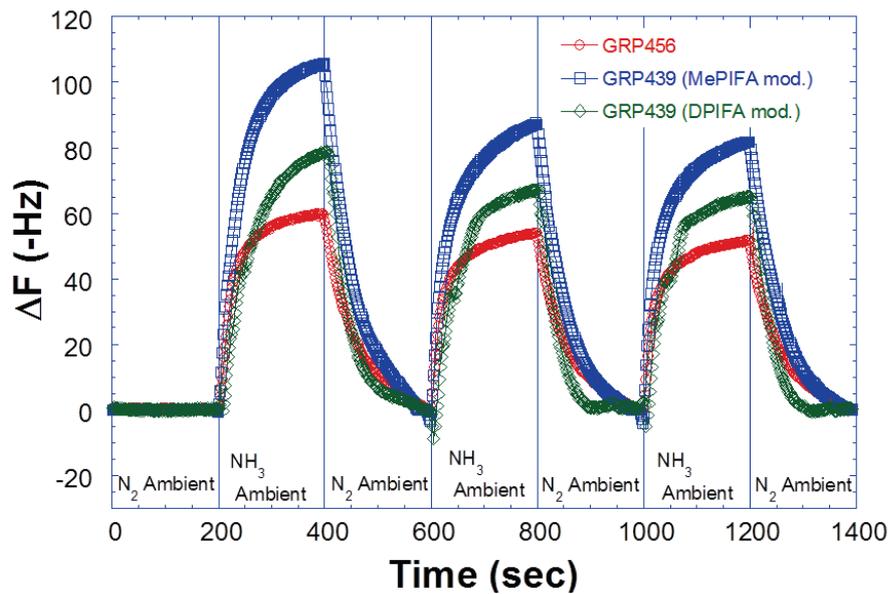


Figure 4.87. Frequency change of GRP456 sample (red circles), MePIFA modified GRP439 sample (blue squares) and DPIFA modified GRP439 sample (green quadrangles) under periodic N₂ - NH₃ gas flows.

From the plot it is obvious that SAM modified samples show better sensitivity with the gas molecule absorption. When compared to GRP456 sample, especially MePIFA modified sample's frequency response is increased nearly 60%. DPIFA modified samples also show nearly 30% enhancement.

Langmuir adsorption isotherm model was used to bring out adsorption kinetics of NH₃ on graphene surface. According to this model, gas molecules adsorbed on surface as monolayer. The surface reaction rate to create a monolayer on the surface can be calculated by using the following equations:

$$\frac{d\theta}{dt} = k_a(1 - \theta)C - k_d\theta \quad (4.2)$$

where θ is the fraction of surface coverage, C is the gas concentration in the air and k_a and k_d are the adsorption and desorption constants, respectively. Also in the QCM method, the fractional coverage as a function of time during the adsorption of NH_3 molecules can be measured while changing resonance frequency. The surface adsorption kinetics and frequency shift (ΔF) of QCM relationship can be given in following equation:

$$\Delta F(t) = \Delta F_{max} K' (1 - e^{(k_{ads}t)}) \quad (4.3)$$

Using the Sauerbrey relation $\Delta m = - (1.34 \text{ ng/Hz } \Delta F)$ the time dependent variation of mass of the adsorbed NH_3 molecules on the coating surface can be calculated. In the literature, the Langmuir method application to QCM results has reported in detail (Darwish and Okur, 2014).

Figure 4.88 presents the least squares fit (solid line) by applying the Langmuir adsorption isotherm model for the adsorption of the NH_3 concentration of bare and SAM modified graphene samples. And Table 4.1 includes calculated parameters from this fitted plot.

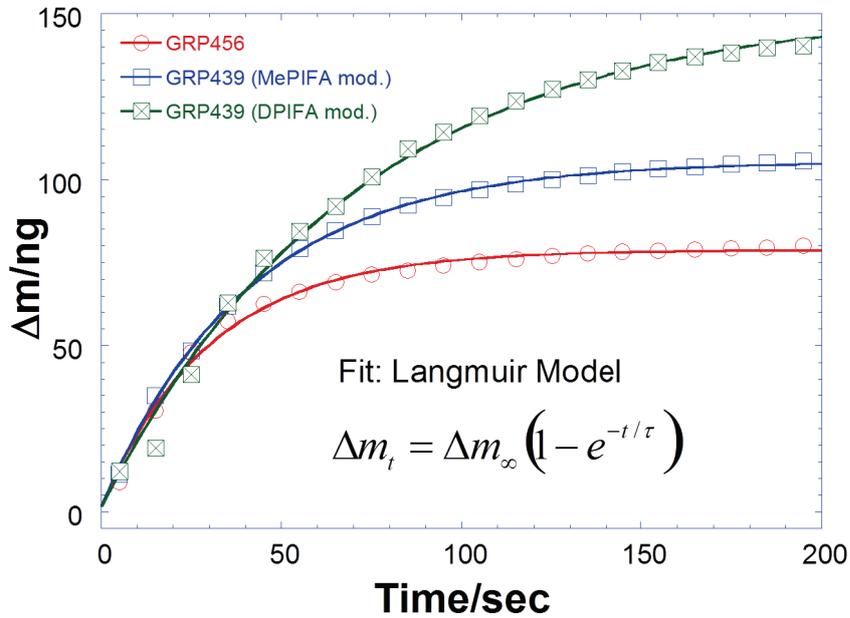


Figure 4.88. Least squares fit (dashed lines) using the Langmuir adsorption isotherm model for bare GRP456, MePIFA and DPIFA modified graphene samples against NH_3 .

Table 4.1. Langmuir adsorption isotherm constants have been derived for NH₃.

Parameters	GRP456	MePIFA mod.	DPIFA mod.
Δm_{∞} (ng)	86.541	115.951	166.881
τ (s)	331.495	447.5	772.418
k_a	15.083	11.173	6.473
k_d	$3.017 e^{-03}$	$2.235 e^{-03}$	$1.295 e^{-03}$
R_{time} at 90%	130	162	268
R	0.9926	0.9963	0.9904

Δm_{∞} represents maximum amount of adsorbed gas molecules while time goes to infinity. τ is relation time that found out taking the time required to drop to 10% of maximum adsorbed value.

As indicated in table, while the adsorbed gas molecule amount increases with SAM modification, response times of devices also increases. There are more available binding sites of modified films due to the SAM molecules' structures and at room temperature humidity molecules bind to these sides. When devices are exposed to ammonia, it takes some time to replace humid molecules with ammonia molecules. Therefore, increasing response time is expected.

Frequency - change comparisons of bare GRP456 sample, MePIFA modified GRP439 sample and DPIFA modified GRP439 samples in periodic Air - NH₃ gas flow intervals are shown in Figure 4.89.

When air is used as cleaning gas, all samples show smaller frequency changes. Again MePIFA modified has higher sensitivity with nearly 40% higher frequency shift when compared to bare GRP456 sample. At this measurement, DPIFA modified sample gives nearly the same response with bare GRP456 sample.

Frequency responses of bare and SAM modified graphene based QCM devices under periodic N₂ (cleaning gas) and Humidity (target gas) flows are shown in Figure 4.90.

Figure 4.91 presents the least squares fit (solid line) by applying the Langmuir adsorption isotherm model for the adsorption of the humidity concentration.

Table 4.2 presents calculated parameters from least square fit of humidity response. As we aimed to construct improved gas sensor devices, we should decrease its humidity sensitivity. When absorbed molecule amount and response time are considered, MePIFA modified device is more suitable.

CVD etched GRP485 and GRP486 samples were also transferred on to quartz crystals for gas sensing investigations.

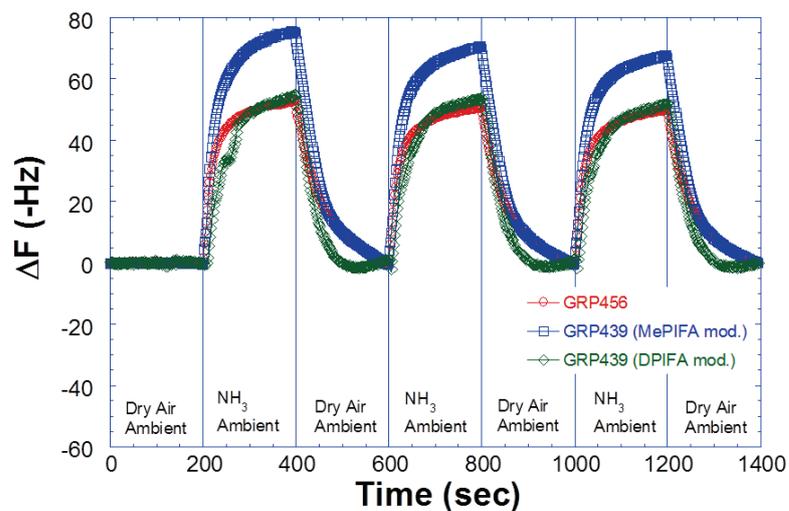


Figure 4.89. Frequency change of GRP456 sample (red circles), MePIFA modified GRP439 sample (blue squares) and DPIFA modified GRP439 sample (green quadrangles) under periodic Air - NH_3 gas flows.

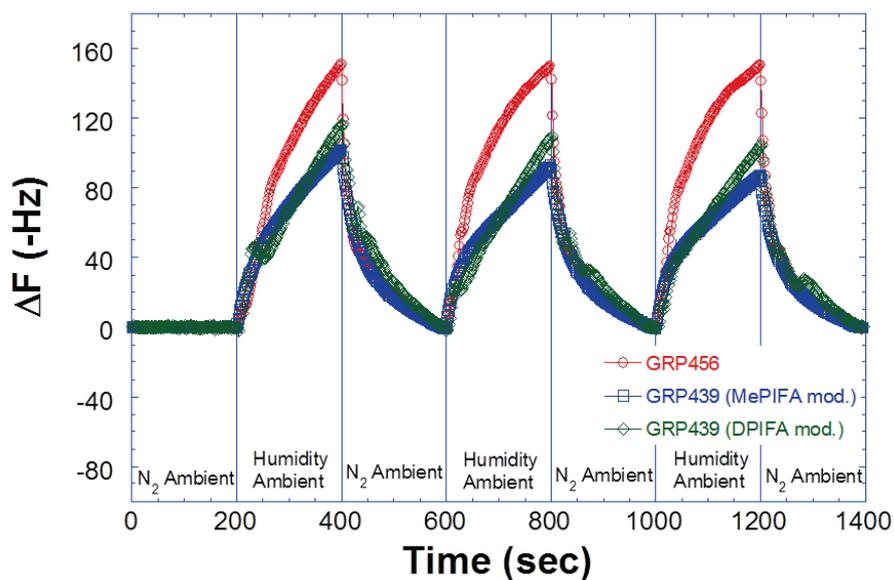


Figure 4.90. Frequency change of GRP456 sample (red circles), MePIFA modified GRP439 sample (blue squares) and DPIFA modified GRP439 sample (green quadrangles) under periodic N_2 - Humidity flows.

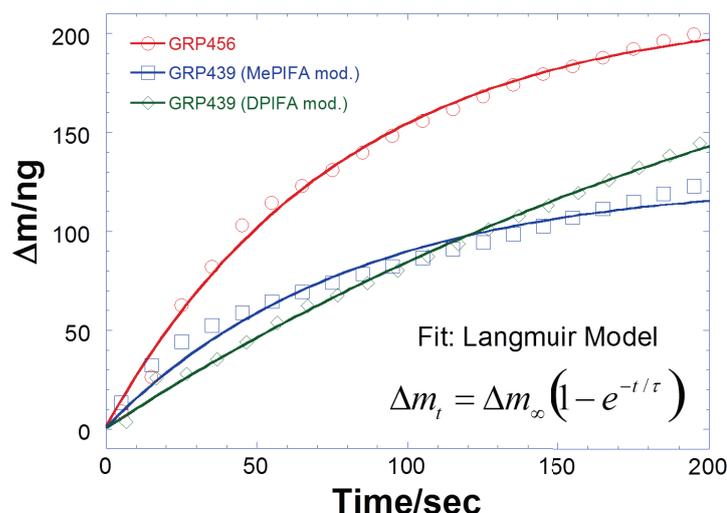


Figure 4.91. Least squares fit (dashed lines) using the Langmuir adsorption isotherm model for bare GRP456, MePIFA and DPIFA modified graphene samples against Humidity.

Table 4.2. Langmuir adsorption isotherm constants have been derived for humidity.

Parameters	GRP456	MePIFA mod.	DPIFA mod.
Δm_{∞} (ng)	234.542	138.358	304.909
τ (s)	857.566	882.896	3042.456
k_a	5.830	5.663	1.643
k_d	$1.166 e^{-03}$	$1.133 e^{-03}$	$3.287 e^{-03}$
R_{time} at 90%	354	450	1266
R	0.9941	0.9677	0.9930

Frequency change comparisons of bare GRP456 and etched GRP485 - GRP486 are also investigated with N_2 - NH_3 , Air - NH_3 and also N_2 - Humidity gas flows. Again both of the cleaning and target gas amounts were 500 sccm and gas species were changed in 200 sec time intervals.

Frequency changes of bare GRP456, etched GRP485 and etched GRP486 during periodic N_2 - NH_3 gas flows are plotted in Figure 4.92.

In the first response of the devices, the best reaction is given by etched GRP485; however, in the following steps its response is decreased gradually. When both of the sensitivity and reproducibility are considered, etched GRP486 has the ideal behavior. Both of the etched samples have higher response to NH_3 gas molecules than that of bare GRP456

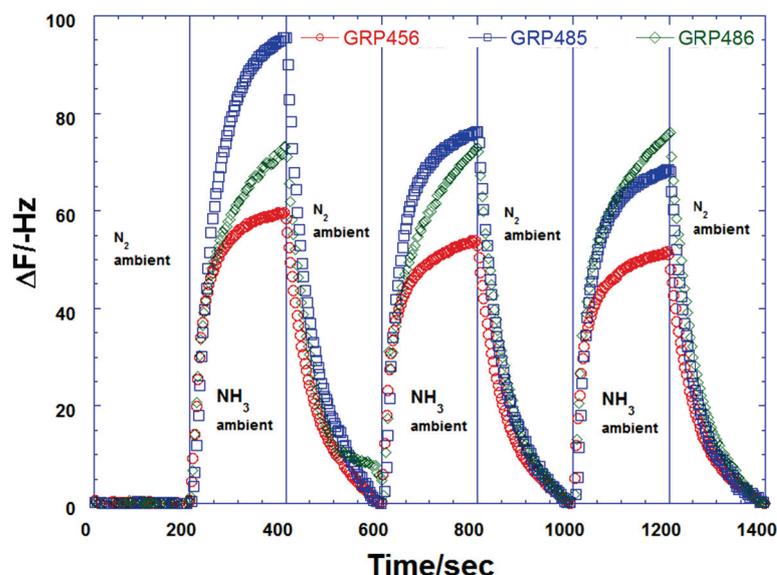


Figure 4.92. Frequency change of GRP456 sample (red circles), etched GRP485 sample (blue squares) and etched GRP486 sample (green quadrangles) under periodic N_2 - NH_3 flows.

sample.

The same measurement is also achieved by using air as a cleaning gas, instead of N_2 (Figure 4.93). Again etched samples are more sensitive to NH_3 gas molecules. In this setup, etched graphene samples are given nearly the same responses during the measurement.

Figure 4.94 presents the least squares fit (solid line) by applying the Langmuir adsorption isotherm model for the adsorption of the NH_3 concentration.

The obtained values for the Langmuir constants were listed in Table 4.3. ΔF_∞ represents maximum amount of adsorbed gas molecules while time goes to infinity. τ is relation time that found out taking the time required to drop to 10% of maximum adsorbed value.

The response times, defined as 'the time to rising up to 90% of maximum value of sensor signal', have been found to be 128, 171 and 165 sec. for bare GRP456, etched GRP485 and etched GRP486, respectively. While the absorbed gas amount etched GRP485 sample is higher, its response time is also shorter. Therefore, when we compare bare GRP56 and etched GRP485, we see the enhancement in absorbed molecule amount and response time.

Humidity effect on graphene based sensors were also investigated using humidity

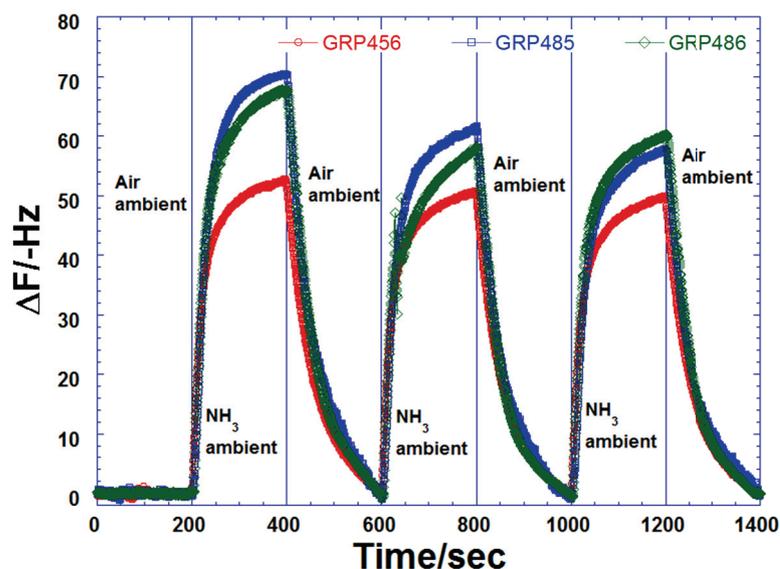


Figure 4.93. Frequency change of GRP456 sample (red circles), etched GRP485 sample (blue squares) and etched GRP486 sample (green quadrangles) under periodic Air - NH₃ flows.

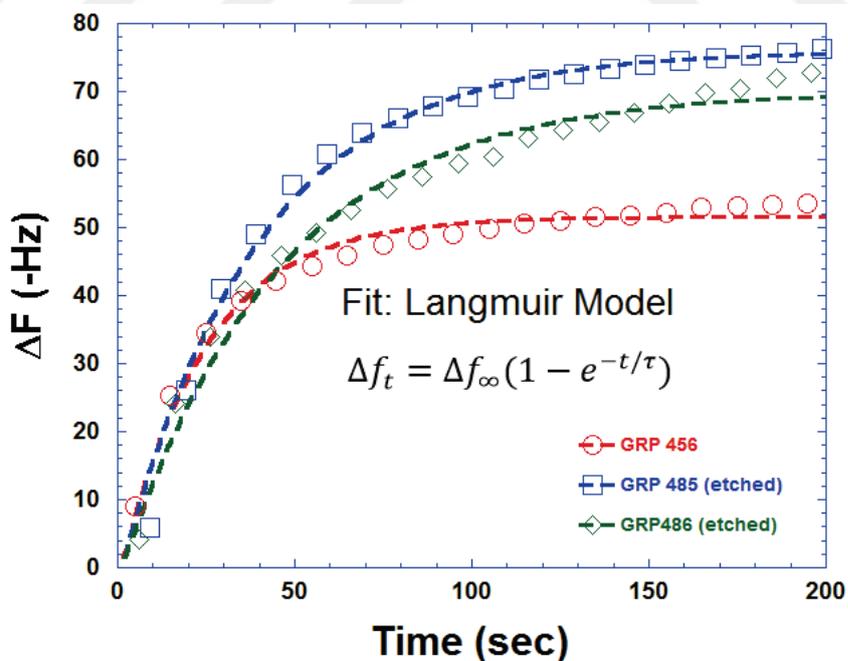


Figure 4.94. Least squares fit (dashed lines) using the Langmuir adsorption isotherm model for GRP456, EGRP485 and GRP486 against NH₃.

Table 4.3. Langmuir adsorption isotherm constants have been derived for NH₃.

Parameters	GRP456	GRP485	GRP486
Δf_{∞} (Hz)	56.73	83.57	77.03
τ (s)	122	108	131
k_a	19.08	11.73	10.15
k_d	$3.815 e^{-03}$	$2.347 e^{-03}$	$2.030 e^{-03}$
R_{time} at 90%	127.87	170.66	165.06
R	0.99	0.99	0.99

molecules as target gas and N₂ gas as cleaning gas. Frequency shifts of bare and etched graphene samples are plotted in Figure 4.95. While the bare GRP456 device is mostly affected by humidity molecules, GRP485 is affected less than that of GRP456. Mostly unaffected sensor is again obtained with the etched GRP486 sample.

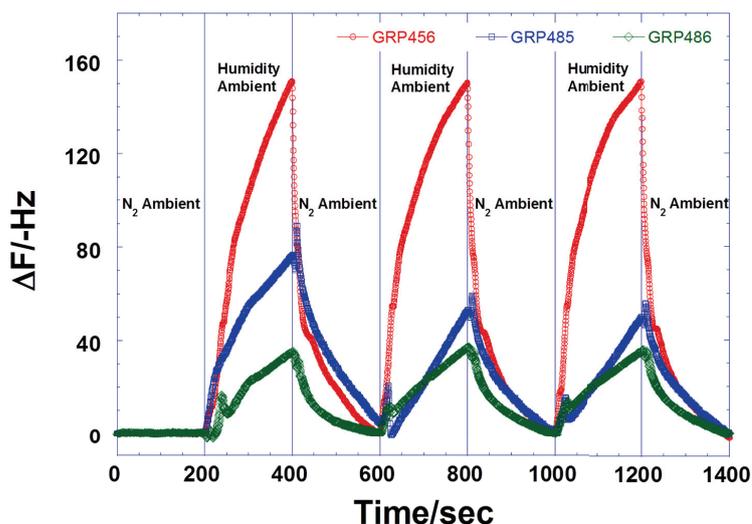


Figure 4.95. Frequency change of GRP456 sample (red circles), etched GRP485 sample (blue squares) and etched GRP486 sample (green quadrangles) under periodic N₂ - Humidity flows.

Langmuir adsorption isotherm model is also applied to humidity plots of bare and etched graphene samples. The least squares fit (solid line) for the adsorption of the humidity molecules is shown in Figure 4.96.

The obtained values for the Langmuir constants were listed in Table 4.4.

In humid environment adsorption of humidity molecule amount is decreased significantly for GRP485 sample when compared to bare GRP456 and etched GRP486. When

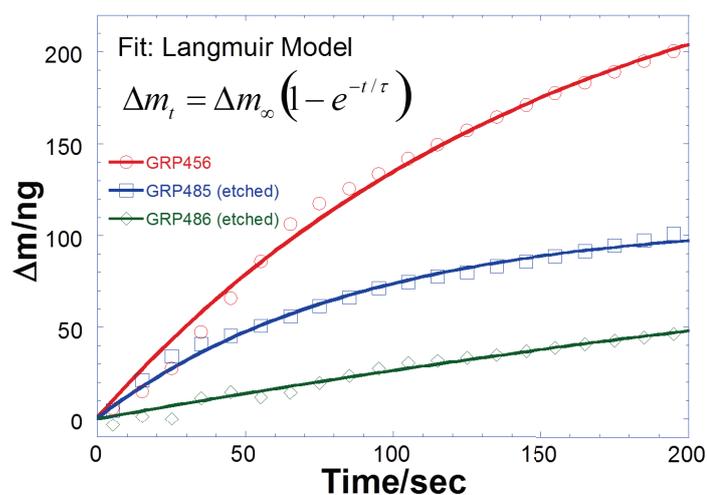


Figure 4.96. Least squares fit (dashed lines) using the Langmuir adsorption isotherm model for GRP456, EGRP485 and GRP486 against humidity.

Table 4.4. Langmuir adsorption isotherm constants have been derived for humidity.

Parameters	GRP456	GRP485	GRP486
Δm_{∞} (ng)	306.482	118.415	154.000
τ (s)	1673.564	952.793	5291.26
k_a	2.988	15.248	0.945
k_d	$5.975 e^{-04}$	$1.050 e^{-03}$	$1.890 e^{-04}$
R_{time} at 90%	783	514	1990
R	0.9891	0.9905	0.9586

we also consider ammonia adsorption kinetics of GRP485, this low sensitivity to humidity molecules enhances the sensor performance and achieve our aim.

4.3.2. Amperometric Characterization

GRP463 sample was grown by standard graphene growth parameters and it was transferred on to gold electrodes for gas sensing investigations.

Resistance change of GRP463 sample under periodic N_2 - NH_3 and Air - NH_3 gas flows with 200 sec time intervals is shown in Figure 4.97. With gas molecule absorption, conductivity of the electrons is obstructed by gas molecules and thus resistivity is increased. Very fast response of GRP463 to NH_3 gas molecules are obtained in both N_2 and air environments. Sensitivity and reproducibility of the shifts are nearly the same at three different time intervals.

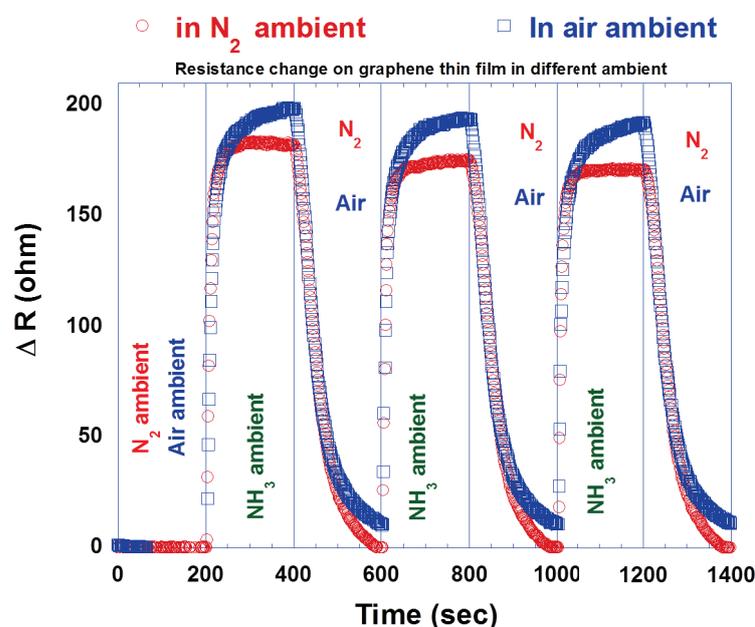


Figure 4.97. Resistance changes of GRP463 in periodic N_2 - NH_3 (red circles) and periodic Air - NH_3 (blue squares) ambient.

Resistance response of GRP463 in humidity environment was investigated in Figure 4.98.

Resistance of GRP463 is less affected by humidity and thus it can be ideally used in gas sensing applications.

Electrical response of SAM modified graphene samples were also investigated in periodic DA - NH_3 ambient. With the NH_3 flow, resistance of the all pristine graphene,

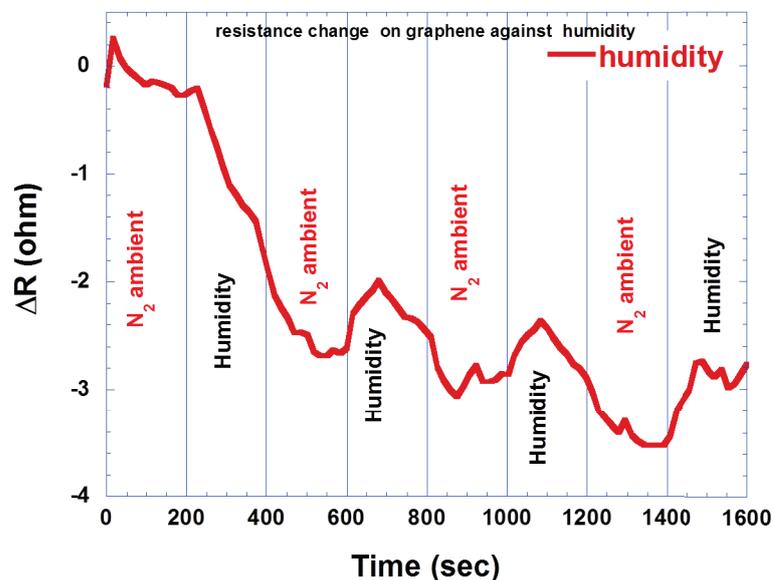


Figure 4.98. Resistance response of GRP463 in periodic N₂ - humidity ambient.

MePIFA modified graphene and DPIFA modified graphene based devices increased. The total resistivity change plot of GRP, MEPIFA modified GRP and DPIFA modified GRP samples are shown in Figure 4.99. This resistivity increase can be explained by the increased gas molecule adsorption on the film surface that prevents electron transmission. More adsorbed gas molecules lead to decrease of electrical conductivity. Therefore, from the plot it is obvious that most response change is observed in MePIFA modified sample and molecule adsorption is mostly occurred in MePIFA modified sample. This results are also consistent with QCM results.

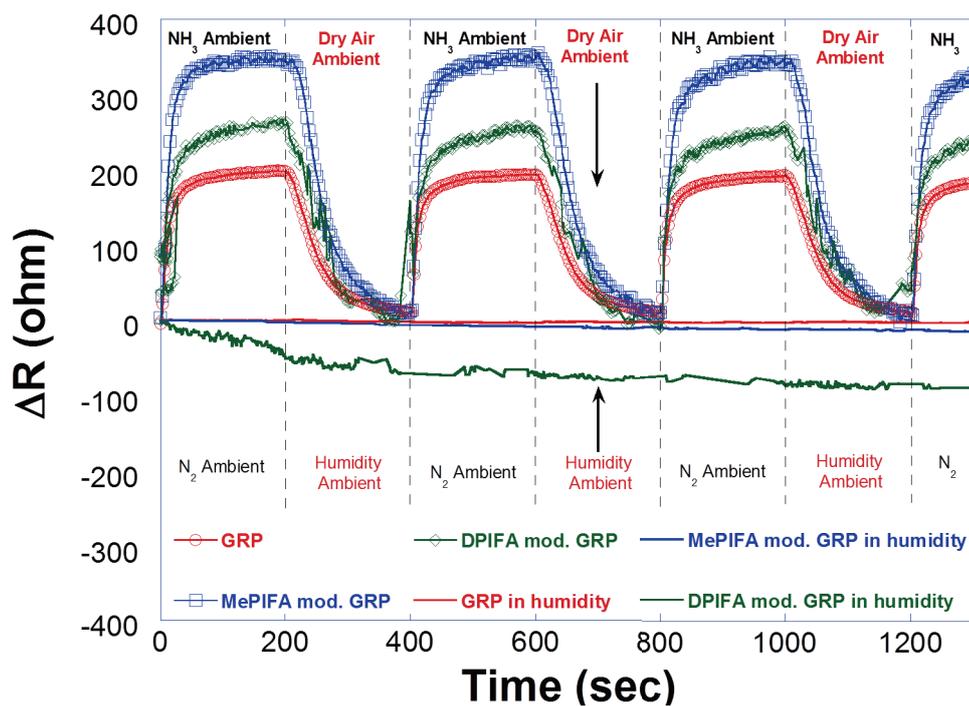


Figure 4.99. Resistance comparison of pristine graphene GRP (red circles), MePIFA modified GRP (blue squares) and DPIFA modified GRP (green quadrangles) in periodic DA - NH_3 and N_2 - Humidity ambient.

Additionally the same devices were also performed in periodic N_2 - Humidity ambient. These plots are also inserted in Figure 4.99. When compared to NH_3 response of the devices, response in humidity doesn't so significant to affect devices' performance.

CHAPTER 5

CONCLUSIONS

Nowadays with the development of technological and industrial initiatives, the need of functional high performance and accurate sensors have gained significant importance. An excellent material, graphene, is also attracted great attention as a gas sensor due to its unique electrical, optical and mechanical properties. Therefore, we produced, used and functionalized graphene films in the manner of microbalanced and electrical devices that might be used especially in toxic gas sensing applications.

In this thesis, CVD method was used to grow graphene on Cu foils with determined ideal growth parameters and transferred onto wet oxidized SiO₂/Si substrates and gold quartz crystals for gas sensing measurements.

Other CVD growth parameters such as growth temperature, gas mixture amount and growth time were also investigated to grow graphene layers that the processes were followed by the CVD reverse-reaction etching under H₂ and Ar gas flows on Cu foil. Samples were then transferred onto appropriate substrates for characterization.

Graphene samples were also functionalized by SAM molecules to improve the surface properties.

Gas sensing measurements were carried out by using QCM technique under periodic N₂/NH₃ and Air/NH₃ gas exposures. The effect of humidity on device performances is also investigated. Device responses were recorded as QCM frequency changes.

Electrical characterization was carried out by applied constant current-voltage values and by measuring resistance change due to the gas molecule adsorption.

Optical microscopy, AFM, SEM results were obtained to investigate the surface coverage and morphology characteristics of pristine graphene and etched graphene based films. SAM modification was explored by measuring surface potential difference using KPFM. For vibrational property investigations Raman spectroscopy results were analyzed.

When optical microscopy results are correlated with Raman spectrometry results, bi-layer pristine graphene layers are obtained by using our standard growth process.

Etching of graphene films under H₂ flow in CVD system and SAM functionalization improved the gas sensing performance of the graphene based devices.

In QCM measurements, maximum improvement is achieved by MEPIFA modified graphene films with nearly 60% frequency increment in N₂ - NH₃ ambient and DPIFA

modified graphene films have nearly 30% enhancement when compared to response of pristine graphene. Etched samples GRP485 and GRP486 samples demonstrate similar performances in $N_2 - NH_3$ and Air - NH_3 ambient with 35% and 20% improvements, respectively. But etched samples are less affected in humid environment when compared to pristine and SAM modified graphene devices.

In electrical characterization, again SAM modified samples show better performances when compared to bare graphene device. While the MePIFA modified device's resistance increase is nearly 75% higher than bare one, DPIFA modified device also showed nearly 25% enhancement.

Both of the QCM and electrical results show that modified and functionalized devices give reproducible and repeatable periodic responses that is the mostly important indicator in gas sensing investigations.

REFERENCES

- Allen, M. J., V. C. Tung, and R. B. Kaner (2009). Honeycomb carbon: a review of graphene. *Chemical reviews* 110(1), 132–145.
- Badami, D. (1965). X-ray studies of graphite formed by decomposing silicon carbide. *Carbon* 3(1), 53–57.
- Bae, S., H. Kim, Y. Lee, X. Xu, J.-S. Park, Y. Zheng, J. Balakrishnan, T. Lei, H. R. Kim, Y. I. Song, et al. (2010). Roll-to-roll production of 30-inch graphene films for transparent electrodes. *Nature nanotechnology* 5(8), 574–578.
- Balandin, A. A., S. Ghosh, W. Bao, I. Calizo, D. Teweldebrhan, F. Miao, and C. N. Lau (2008). Superior thermal conductivity of single-layer graphene. *Nano letters* 8(3), 902–907.
- Bao, W., F. Miao, Z. Chen, H. Zhang, W. Jang, C. Dames, and C. N. Lau (2009). Controlled ripple texturing of suspended graphene and ultrathin graphite membranes. *Nature nanotechnology* 4(9), 562–566.
- Berger, C., Z. Song, T. Li, X. Li, A. Y. Ogbazghi, R. Feng, Z. Dai, A. N. Marchenkov, E. H. Conrad, P. N. First, et al. (2004). Ultrathin epitaxial graphite: 2d electron gas properties and a route toward graphene-based nanoelectronics. *The Journal of Physical Chemistry B* 108(52), 19912–19916.
- Berger, C., Z. Song, X. Li, X. Wu, N. Brown, C. Naud, D. Mayou, T. Li, J. Hass, A. N. Marchenkov, et al. (2006). Electronic confinement and coherence in patterned epitaxial graphene. *Science* 312(5777), 1191–1196.
- Blake, P., P. D. Brimicombe, R. R. Nair, T. J. Booth, D. Jiang, F. Schedin, L. A. Ponomarenko, S. V. Morozov, H. F. Gleeson, E. W. Hill, et al. (2008). Graphene-based liquid crystal device. *Nano letters* 8(6), 1704–1708.
- Blake, P., E. Hill, A. C. Neto, K. Novoselov, D. Jiang, R. Yang, T. Booth, and A. Geim (2007). Making graphene visible. *Applied Physics Letters* 91(6), 063124.
- Boehm, H., R. Setton, and E. Stumpp (1986). Nomenclature and terminology of graphite intercalation compounds. *Carbon* 24(2), 241–245.
- Bolotin, K., K. Sikes, J. Hone, H. Stormer, and P. Kim (2008). Temperature-dependent transport in suspended graphene. *Physical review letters* 101(9), 096802.
- Bolotin, K. I., K. Sikes, Z. Jiang, M. Klima, G. Fudenberg, J. Hone, P. Kim, and H. Stormer (2008). Ultrahigh electron mobility in suspended graphene. *Solid State Communications* 146(9), 351–355.
- Bonaccorso, F., A. Lombardo, T. Hasan, Z. Sun, L. Colombo, and A. C. Ferrari (2012). Production and processing of graphene and 2d crystals. *Materials Today* 15(12), 564–589.

- Bonaccorso, F., Z. Sun, T. Hasan, and A. Ferrari (2010). Graphene photonics and optoelectronics. *Nature photonics* 4(9), 611–622.
- Butt, M. (1983). Effect of hydrogen attack on the strength of high purity copper. *Journal of Materials Science Letters* 2(1), 1–2.
- Cai, W., Y. Zhu, X. Li, R. D. Piner, and R. S. Ruoff (2009). Large area few-layer graphene/graphite films as transparent thin conducting electrodes. *Applied Physics Letters* 95(12), 123115.
- Can, M., A. K. Havare, H. Aydın, N. Yagmurcukardes, S. Demic, S. Icli, and S. Okur (2014). Electrical properties of sam-modified ito surface using aromatic small molecules with double bond carboxylic acid groups for oled applications. *Applied Surface Science* 314, 1082–1086.
- Chen, G., T. M. Paronyan, and A. R. Harutyunyan (2012). Sub-ppt gas detection with pristine graphene. *Applied Physics Letters* 101(5), 053119.
- Chen, H., W. Zhu, and Z. Zhang (2010). Contrasting behavior of carbon nucleation in the initial stages of graphene epitaxial growth on stepped metal surfaces. *Physical Review Letters* 104(18), 186101.
- Chen, J.-H., C. Jang, S. Xiao, M. Ishigami, and M. S. Fuhrer (2008). Intrinsic and extrinsic performance limits of graphene devices on sio₂. *Nature nanotechnology* 3(4), 206–209.
- Chung, M. G., D.-H. Kim, D. K. Seo, T. Kim, H. U. Im, H. M. Lee, J.-B. Yoo, S.-H. Hong, T. J. Kang, and Y. H. Kim (2012). Flexible hydrogen sensors using graphene with palladium nanoparticle decoration. *Sensors and Actuators B: Chemical* 169, 387–392.
- Constant, L., C. Speisser, and F. Le Normand (1997). Hfcvd diamond growth on cu (111). evidence for carbon phase transformations by in situ aes and xps. *Surface Science* 387(1), 28–43.
- Cui, S., Z. Wen, E. C. Mattson, S. Mao, J. Chang, M. Weinert, C. J. Hirschmugl, M. Gajdardziska-Josifovska, and J. Chen (2013). Indium-doped sno₂ nanoparticle–graphene nanohybrids: simple one-pot synthesis and their selective detection of no₂. *Journal of Materials Chemistry A* 1(14), 4462–4467.
- Darwish, H. M. B. and S. Okur (2014). Co adsorption kinetics of ferrocene-conjugated polypyrrole using quartz microbalance technique. *Sensors and Actuators B: Chemical* 200, 325–331.
- Dean, C. R., A. F. Young, I. Meric, C. Lee, L. Wang, S. Sorgenfrei, K. Watanabe, T. Taniguchi, P. Kim, K. Shepard, et al. (2010). Boron nitride substrates for high-quality graphene electronics. *Nature nanotechnology* 5(10), 722–726.
- Ding, L., A. Tselev, J. Wang, D. Yuan, H. Chu, T. P. McNicholas, Y. Li, and J. Liu

- (2009). Selective growth of well-aligned semiconducting single-walled carbon nanotubes. *Nano letters* 9(2), 800–805.
- Dresselhaus, M. S., G. Dresselhaus, and A. Jorio (2007). *Group theory: application to the physics of condensed matter*. Springer Science & Business Media.
- Dresselhaus, M. S., G. Dresselhaus, R. Saito, and A. Jorio (2005). Raman spectroscopy of carbon nanotubes. *Physics reports* 409(2), 47–99.
- Du, X., I. Skachko, A. Barker, and E. Y. Andrei (2008). Approaching ballistic transport in suspended graphene. *Nature nanotechnology* 3(8), 491–495.
- Emtsev, K. V., A. Bostwick, K. Horn, J. Jobst, G. L. Kellogg, L. Ley, J. L. McChesney, T. Ohta, S. A. Reshanov, J. Röhrl, et al. (2009). Towards wafer-size graphene layers by atmospheric pressure graphitization of silicon carbide. *Nature materials* 8(3), 203–207.
- Eom, D., D. Prezzi, K. T. Rim, H. Zhou, M. Lefenfeld, S. Xiao, C. Nuckolls, M. S. Hybertsen, T. F. Heinz, and G. W. Flynn (2009). Structure and electronic properties of graphene nanoislands on co (0001). *Nano letters* 9(8), 2844–2848.
- Esfandiari, A., S. Ghasemi, A. Irajizad, O. Akhavan, and M. Gholami (2012). The decoration of tio₂/reduced graphene oxide by pd and pt nanoparticles for hydrogen gas sensing. *international journal of hydrogen energy* 37(20), 15423–15432.
- Fattah, A. and S. Khatami (2014). Selective h₂ s gas sensing with a graphene/n-si schottky diode. *IEEE Sensors Journal* 14(11), 4104–4108.
- Ferrari, A., J. Meyer, V. Scardaci, C. Casiraghi, M. Lazzeri, F. Mauri, S. Piscanec, D. Jiang, K. Novoselov, S. Roth, et al. (2006). Raman spectrum of graphene and graphene layers. *Physical review letters* 97(18), 187401.
- Forbeaux, I., J.-M. Themlin, and J.-M. Debever (1998). Heteroepitaxial graphite on 6 h-sic (0001): Interface formation through conduction-band electronic structure. *Physical Review B* 58(24), 16396.
- Ganji, M. D., S. Hosseini-Khah, and Z. Amini-Tabar (2015). Theoretical insight into hydrogen adsorption onto graphene: a first-principles b3lyp-d3 study. *Physical Chemistry Chemical Physics* 17(4), 2504–2511.
- Gautam, M. and A. H. Jayatissa (2011). Gas sensing properties of graphene synthesized by chemical vapor deposition. *Materials Science and Engineering: C* 31(7), 1405–1411.
- Geim, A. K. and K. S. Novoselov (2007). The rise of graphene. *Nature materials* 6(3), 183–191.
- Geng, D., B. Wu, Y. Guo, B. Luo, Y. Xue, J. Chen, G. Yu, and Y. Liu (2013). Fractal etching of graphene. *Journal of the American Chemical Society* 135(17), 6431–6434.

- Gomez De Arco, L., Y. Zhang, C. W. Schlenker, K. Ryu, M. E. Thompson, and C. Zhou (2010). Continuous, highly flexible, and transparent graphene films by chemical vapor deposition for organic photovoltaics. *ACS nano* 4(5), 2865–2873.
- Graf, D., F. Molitor, K. Ensslin, C. Stampfer, A. Jungen, C. Hierold, and L. Wirtz (2007). Spatially resolved raman spectroscopy of single-and few-layer graphene. *Nano letters* 7(2), 238–242.
- Gupta, A., G. Chen, P. Joshi, S. Tadigadapa, and P. Eklund (2006). Raman scattering from high-frequency phonons in supported n-graphene layer films. *Nano letters* 6(12), 2667–2673.
- Gutés, A., B. Hsia, A. Sussman, W. Mickelson, A. Zettl, C. Carraro, and R. Maboudian (2012). Graphene decoration with metal nanoparticles: towards easy integration for sensing applications. *Nanoscale* 4(2), 438–440.
- Hong, J., S. Lee, J. Seo, S. Pyo, J. Kim, and T. Lee (2015). A highly sensitive hydrogen sensor with gas selectivity using a pmma membrane-coated pd nanoparticle/single-layer graphene hybrid. *ACS applied materials & interfaces* 7(6), 3554–3561.
- Huang, Q., D. Zeng, H. Li, and C. Xie (2012). Room temperature formaldehyde sensors with enhanced performance, fast response and recovery based on zinc oxide quantum dots/graphene nanocomposites. *Nanoscale* 4(18), 5651–5658.
- Huang, X., N. Hu, R. Gao, Y. Yu, Y. Wang, Z. Yang, E. S.-W. Kong, H. Wei, and Y. Zhang (2012). Reduced graphene oxide–polyaniline hybrid: preparation, characterization and its applications for ammonia gas sensing. *Journal of Materials Chemistry* 22(42), 22488–22495.
- Huang, X. L., N. T. Hu, Y. Y. Wang, and Y. F. Zhang (2013). Ammonia gas sensor based on aniline reduced graphene oxide. In *Advanced Materials Research*, Volume 669, pp. 79–84. Trans Tech Publ.
- Ismach, A., C. Druzgalski, S. Penwell, A. Schwartzberg, M. Zheng, A. Javey, J. Bokor, and Y. Zhang (2010). Direct chemical vapor deposition of graphene on dielectric surfaces. *Nano letters* 10(5), 1542–1548.
- James, F. A. (2010). *Michael Faraday: a very short introduction*, Volume 253. Oxford University Press.
- Jang, W.-K., J. Yun, H.-I. Kim, and Y.-S. Lee (2013). Improvement of ammonia sensing properties of polypyrrole by nanocomposite with graphitic materials. *Colloid and Polymer Science* 291(5), 1095–1103.
- Jeong, H. Y., D.-S. Lee, H. K. Choi, D. H. Lee, J.-E. Kim, J. Y. Lee, W. J. Lee, S. O. Kim, and S.-Y. Choi (2010). Flexible room-temperature no₂ gas sensors based on carbon nanotubes/reduced graphene hybrid films.
- Jiao, L., L. Zhang, X. Wang, G. Diankov, and H. Dai (2009). Narrow graphene nanorib-

- bons from carbon nanotubes. *Nature* 458(7240), 877–880.
- Jorio, A., M. Dresselhaus, R. Saito, and G. Dresselhaus. Raman spectroscopy in graphene related systems. 2011.
- Jorio, A., M. Dresselhaus, R. Saito, and G. Dresselhaus (2011). Raman spectroscopy in graphene related systems, swiley.
- Kaniyoor, A., R. I. Jafri, T. Arockiadoss, and S. Ramaprabhu (2009). Nanostructured pt decorated graphene and multi walled carbon nanotube based room temperature hydrogen gas sensor. *Nanoscale* 1(3), 382–386.
- Kim, K. S., Y. Zhao, H. Jang, S. Y. Lee, J. M. Kim, K. S. Kim, J.-H. Ahn, P. Kim, J.-Y. Choi, and B. H. Hong (2009). Large-scale pattern growth of graphene films for stretchable transparent electrodes. *Nature* 457(7230), 706–710.
- Ko, G., H.-Y. Kim, J. Ahn, Y.-M. Park, K.-Y. Lee, and J. Kim (2010). Graphene-based nitrogen dioxide gas sensors. *Current Applied Physics* 10(4), 1002–1004.
- Kong, X.-K., C.-L. Chen, and Q.-W. Chen (2014). Doped graphene for metal-free catalysis. *Chemical Society Reviews* 43(8), 2841–2857.
- Kosynkin, D. V., A. L. Higginbotham, A. Sinitskii, J. R. Lomeda, A. Dimiev, B. K. Price, and J. M. Tour (2009). Longitudinal unzipping of carbon nanotubes to form graphene nanoribbons. *Nature* 458(7240), 872–876.
- Kumar, R., D. Varandani, and B. Mehta (2016). Nanoscale interface formation and charge transfer in graphene/silicon schottky junctions; kpfm and cafm studies. *Carbon* 98, 41–49.
- Kumar, S., S. Kaushik, R. Pratap, and S. Raghavan (2015). Graphene on paper: A simple, low-cost chemical sensing platform. *ACS applied materials & interfaces* 7(4), 2189–2194.
- Kuzmenko, A., E. Van Heumen, F. Carbone, and D. Van Der Marel (2008). Universal optical conductance of graphite. *Physical review letters* 100(11), 117401.
- Lazzeri, M., C. Attaccalite, L. Wirtz, and F. Mauri (2008). Impact of the electron–electron correlation on phonon dispersion: Failure of lda and gga dft functionals in graphene and graphite. *Physical Review B* 78(8), 081406.
- Lee, B., Y. Chen, F. Duerr, D. Mastrogiovanni, E. Garfunkel, E. Andrei, and V. Podzorov (2010). Modification of electronic properties of graphene with self-assembled monolayers. *Nano letters* 10(7), 2427–2432.
- Lee, K.-J. and S.-J. Kim (2013). Theoretical investigation of co₂ adsorption on graphene. *Bull. Korean Chem. Soc* 34(10), 3022–3026.
- Lee, N., J. Yoo, Y. Choi, C. Kang, D. Jeon, D. Kim, S. Seo, and H. Chung (2009).

- The interlayer screening effect of graphene sheets investigated by kelvin probe force microscopy. *Applied Physics Letters* 95(22), 222107.
- Lee, Y., S. Bae, H. Jang, S. Jang, S.-E. Zhu, S. H. Sim, Y. I. Song, B. H. Hong, and J.-H. Ahn (2010). Wafer-scale synthesis and transfer of graphene films. *Nano letters* 10(2), 490–493.
- Lee, Y.-H. and J.-H. Lee (2010). Scalable growth of free-standing graphene wafers with copper (cu) catalyst on sio₂/si substrate: Thermal conductivity of the wafers. *Applied Physics Letters* 96(8), 083101.
- Leenaerts, O., B. Partoens, and F. Peeters (2008). Adsorption of h₂o, nh₃, co, no₂, and no on graphene: A first-principles study. *Physical Review B* 77(12), 125416.
- Lemme, M. C. (2010). Current status of graphene transistors. In *Solid State Phenomena*, Volume 156, pp. 499–509. Trans Tech Publ.
- Levendorf, M. P., C. S. Ruiz-Vargas, S. Garg, and J. Park (2009). Transfer-free batch fabrication of single layer graphene transistors. *Nano letters* 9(12), 4479–4483.
- Li, J.-R., R. J. Kuppler, and H.-C. Zhou (2009). Selective gas adsorption and separation in metal–organic frameworks. *Chemical Society Reviews* 38(5), 1477–1504.
- Li, X., W. Cai, J. An, S. Kim, J. Nah, D. Yang, R. Piner, A. Velamakanni, I. Jung, E. Tutuc, et al. (2009). Large-area synthesis of high-quality and uniform graphene films on copper foils. *Science* 324(5932), 1312–1314.
- Li, X., Y. Zhu, W. Cai, M. Borysiak, B. Han, D. Chen, R. D. Piner, L. Colombo, and R. S. Ruoff (2009). Transfer of large-area graphene films for high-performance transparent conductive electrodes. *Nano letters* 9(12), 4359–4363.
- Lin, W.-D., H.-M. Chang, and R.-J. Wu (2013). Applied novel sensing material graphene/polypyrrole for humidity sensor. *Sensors and Actuators B: Chemical* 181, 326–331.
- Liscio, A., G. P. Veronese, E. Treossi, F. Suriano, F. Rossella, V. Bellani, R. Rizoli, P. Samorì, and V. Palermo (2011). Charge transport in graphene–polythiophene blends as studied by kelvin probe force microscopy and transistor characterization. *Journal of Materials Chemistry* 21(9), 2924–2931.
- Liu, H., Y. Liu, and D. Zhu (2011). Chemical doping of graphene. *Journal of materials chemistry* 21(10), 3335–3345.
- Liu, S., B. Yu, H. Zhang, T. Fei, and T. Zhang (2014). Enhancing no₂ gas sensing performances at room temperature based on reduced graphene oxide-zno nanoparticles hybrids. *Sensors and Actuators B: Chemical* 202, 272–278.
- Mafra, D., G. Samsonidze, L. Malard, D. Elias, J. Brant, F. Plentz, E. Alves, and M. Pimenta (2007). Determination of la and to phonon dispersion relations of graphene

- near the dirac point by double resonance raman scattering. *Physical Review B* 76(23), 233407.
- Malard, L., J. Nilsson, D. Elias, J. Brant, F. Plentz, E. Alves, A. C. Neto, and M. Pimenta (2007). Probing the electronic structure of bilayer graphene by raman scattering. *Physical Review B* 76(20), 201401.
- Malard, L., M. Pimenta, G. Dresselhaus, and M. Dresselhaus (2009). Raman spectroscopy in graphene. *Physics Reports* 473(5), 51–87.
- Mangu, R., S. Rajaputra, and V. P. Singh (2011). Mwcnt–polymer composites as highly sensitive and selective room temperature gas sensors. *Nanotechnology* 22(21), 215502.
- Mao, S., S. Cui, G. Lu, K. Yu, Z. Wen, and J. Chen (2012). Tuning gas-sensing properties of reduced graphene oxide using tin oxide nanocrystals. *Journal of Materials Chemistry* 22(22), 11009–11013.
- Mattevi, C., H. Kim, and M. Chhowalla (2011). A review of chemical vapour deposition of graphene on copper. *Journal of Materials Chemistry* 21(10), 3324–3334.
- McClure, J. (1957). Band structure of graphite and de haas-van alphen effect. *Physical Review* 108(3), 612.
- Mishra, S. K., S. N. Tripathi, V. Choudhary, and B. D. Gupta (2014). Spr based fibre optic ammonia gas sensor utilizing nanocomposite film of pmma/reduced graphene oxide prepared by in situ polymerization. *Sensors and Actuators B: Chemical* 199, 190–200.
- Morozov, S., K. Novoselov, M. Katsnelson, F. Schedin, D. Elias, J. A. Jaszczak, and A. Geim (2008). Giant intrinsic carrier mobilities in graphene and its bilayer. *Physical review letters* 100(1), 016602.
- Nair, R. R., P. Blake, A. N. Grigorenko, K. S. Novoselov, T. J. Booth, T. Stauber, N. M. Peres, and A. K. Geim (2008). Fine structure constant defines visual transparency of graphene. *Science* 320(5881), 1308–1308.
- Narula, R. and S. Reich (2008). Double resonant raman spectra in graphene and graphite: A two-dimensional explanation of the raman amplitude. *Physical Review B* 78(16), 165422.
- Nelson, J. and D. Riley (1945). The thermal expansion of graphite from 15 c. to 800 c.: Part i. experimental. *Proceedings of the Physical Society* 57(6), 477.
- Nemade, K. and S. Waghuley (2013). Chemiresistive gas sensing by few-layered graphene. *Journal of electronic materials* 42(10), 2857–2866.
- Neto, A. C., F. Guinea, N. M. Peres, K. S. Novoselov, and A. K. Geim (2009). The electronic properties of graphene. *Reviews of modern physics* 81(1), 109.

- Niu, F., J.-M. Liu, L.-M. Tao, W. Wang, and W.-G. Song (2013). Nitrogen and silica co-doped graphene nanosheets for NO₂ gas sensing. *Journal of Materials Chemistry A* 1(20), 6130–6133.
- Niu, F., L.-M. Tao, Y.-C. Deng, Q.-H. Wang, and W.-G. Song (2014). Phosphorus doped graphene nanosheets for room temperature NH₃ sensing. *New Journal of Chemistry* 38(6), 2269–2272.
- Norimatsu, W. and M. Kusunoki (2014). Epitaxial graphene on SiC {0001}: advances and perspectives. *Physical Chemistry Chemical Physics* 16(8), 3501–3511.
- Novoselov, K., A. K. Geim, S. Morozov, D. Jiang, M. Katsnelson, I. Grigorieva, S. Dubonos, and A. Firsov (2005). Two-dimensional gas of massless Dirac fermions in graphene. *Nature* 438(7065), 197–200.
- Novoselov, K. S., A. K. Geim, S. V. Morozov, D. Jiang, Y. Zhang, S. V. Dubonos, I. V. Grigorieva, and A. A. Firsov (2004). Electric field effect in atomically thin carbon films. *Science* 306(5696), 666–669.
- Ohta, T., A. Bostwick, T. Seyller, K. Horn, and E. Rotenberg (2006). Controlling the electronic structure of bilayer graphene. *Science* 313(5789), 951–954.
- Ong, T., F. Xiong, R. P. Chang, and C. White (1992). Nucleation and growth of diamond on carbon-implanted single crystal copper surfaces. *Journal of Materials Research* 7(09), 2429–2439.
- Pak, Y., S.-M. Kim, H. Jeong, C. G. Kang, J. S. Park, H. Song, R. Lee, N. Myoung, B. H. Lee, S. Seo, et al. (2014). Palladium-decorated hydrogen-gas sensors using periodically aligned graphene nanoribbons. *ACS Applied Materials & Interfaces* 6(15), 13293–13298.
- Parmar, M., C. Balamurugan, and D.-W. Lee (2013). PANI and graphene/PANI nanocomposite films—comparative toluene gas sensing behavior. *Sensors* 13(12), 16611–16624.
- Partoens, B. and F. Peeters (2006). From graphene to graphite: Electronic structure around the K point. *Physical Review B* 74(7), 075404.
- Rañola, R. A. G., J. M. Kalaw, and F. B. Sevilla (2015). Graphene/nylon-6 chemiresistor sensor for trimethylamine gas sensing. In *Specialized Collections*, Volume 3, pp. 2440–2444. Trans Tech Publ.
- Reina, A., X. Jia, J. Ho, D. Nezich, H. Son, V. Bulovic, M. S. Dresselhaus, and J. Kong (2008). Large area, few-layer graphene films on arbitrary substrates by chemical vapor deposition. *Nano Letters* 9(1), 30–35.
- Robertson, W. (1964). Faceting of copper surfaces at 1000 Å° C. *Acta Metallurgica* 12(2), 241–253.
- Rumyantsev, S., G. Liu, M. S. Shur, R. A. Potyrailo, and A. A. Balandin (2012). Selective

- gas sensing with a single pristine graphene transistor. *Nano letters* 12(5), 2294–2298.
- Saito, R., A. Jorio, A. G. Souza Filho, G. Dresselhaus, M. S. Dresselhaus, and M. A. Pimenta (2001, Dec). Probing phonon dispersion relations of graphite by double resonance raman scattering. *Phys. Rev. Lett.* 88, 027401.
- Schedin, F., A. Geim, S. Morozov, E. Hill, P. Blake, M. Katsnelson, and K. Novoselov (2007). Detection of individual gas molecules adsorbed on graphene. *Nature materials* 6(9), 652–655.
- Seekaew, Y., S. Lokavee, D. Phokharatkul, A. Wisitsoraat, T. Kerdcharoen, and C. Wongchoosuk (2014). Low-cost and flexible printed graphene–pedot: Pss gas sensor for ammonia detection. *Organic Electronics* 15(11), 2971–2981.
- Semenoff, G. W. (1984). Condensed-matter simulation of a three-dimensional anomaly. *Physical Review Letters* 53(26), 2449.
- Singh, G., A. Choudhary, D. Haranath, A. G. Joshi, N. Singh, S. Singh, and R. Pasricha (2012). ZnO decorated luminescent graphene as a potential gas sensor at room temperature. *Carbon* 50(2), 385–394.
- Slonczewski, J. and P. Weiss (1958). Band structure of graphite. *Physical Review* 109(2), 272.
- Srivastava, A., C. Galande, L. Ci, L. Song, C. Rai, D. Jariwala, K. F. Kelly, and P. M. Ajayan (2010). Novel liquid precursor-based facile synthesis of large-area continuous, single, and few-layer graphene films. *Chemistry of Materials* 22(11), 3457–3461.
- Srivastava, S., S. Sharma, S. Agrawal, S. Kumar, M. Singh, and Y. Vijay (2010). Study of chemiresistor type cnt doped polyaniline gas sensor. *Synthetic Metals* 160(5), 529–534.
- Stankovich, S., D. A. Dikin, G. H. Dommett, K. M. Kohlhaas, E. J. Zimney, E. A. Stach, R. D. Piner, S. T. Nguyen, and R. S. Ruoff (2006). Graphene-based composite materials. *nature* 442(7100), 282–286.
- Su, P.-G. and H.-C. Shieh (2014). Flexible no 2 sensors fabricated by layer-by-layer covalent anchoring and in situ reduction of graphene oxide. *Sensors and Actuators B: Chemical* 190, 865–872.
- Sze, S. M. and K. K. Ng (2006). *Physics of semiconductor devices*. John wiley & sons.
- Teo, G., H. Wang, Y. Wu, Z. Guo, J. Zhang, Z. Ni, and Z. Shen (2008). Visibility study of graphene multilayer structures. *Journal of applied physics* 103(12), 124302.
- Terrones, H., R. Lv, M. Terrones, and M. S. Dresselhaus (2012). The role of defects and doping in 2d graphene sheets and 1d nanoribbons. *Reports on Progress in Physics* 75(6), 062501.

- Tománek, D., A. Jorio, M. S. Dresselhaus, and G. Dresselhaus (2007). Introduction to the important and exciting aspects of carbon-nanotube science and technology. In *Carbon Nanotubes*, pp. 1–12. Springer.
- Usachov, D., O. Vilkov, A. Gruneis, D. Haberer, A. Fedorov, V. Adamchuk, A. Proobrajanski, P. Dudin, A. Barinov, M. Oehzelt, et al. (2011). Nitrogen-doped graphene: efficient growth, structure, and electronic properties. *Nano letters* 11(12), 5401–5407.
- Van Bommel, A., J. Crombeen, and A. Van Tooren (1975). Leed and auger electron observations of the sic (0001) surface. *Surface Science* 48(2), 463–472.
- Varghese, S. S., S. Lonkar, K. Singh, S. Swaminathan, and A. Abdala (2015). Recent advances in graphene based gas sensors. *Sensors and Actuators B: Chemical* 218, 160–183.
- Vaziri, S. (2011). Fabrication and characterization of graphene field effect transistors.
- Virojanadara, C., M. Syväjarvi, R. Yakimova, L. Johansson, A. Zakharov, and T. Balasubramanian (2008). Homogeneous large-area graphene layer growth on 6 h-sic (0001). *Physical Review B* 78(24), 245403.
- Wallace, P. R. (1947). The band theory of graphite. *Physical Review* 71(9), 622.
- Wang, F., Y. Zhang, C. Tian, C. Girit, A. Zettl, M. Crommie, and Y. R. Shen (2008). Gate-variable optical transitions in graphene. *science* 320(5873), 206–209.
- Wehling, T., K. Novoselov, S. Morozov, E. Vdovin, M. Katsnelson, A. Geim, and A. Lichtenstein (2008). Molecular doping of graphene. *Nano letters* 8(1), 173–177.
- Wei, D., Y. Liu, Y. Wang, H. Zhang, L. Huang, and G. Yu (2009). Synthesis of n-doped graphene by chemical vapor deposition and its electrical properties. *Nano letters* 9(5), 1752–1758.
- Wu, Z.-S., W. Ren, L. Gao, B. Liu, C. Jiang, and H.-M. Cheng (2009). Synthesis of high-quality graphene with a pre-determined number of layers. *Carbon* 47(2), 493–499.
- Yan, L., C. Punckt, I. A. Aksay, W. Mertin, and G. Bacher (2011). Local voltage drop in a single functionalized graphene sheet characterized by kelvin probe force microscopy. *Nano letters* 11(9), 3543–3549.
- Yang, R. T. (2003). *Adsorbents: fundamentals and applications*. John Wiley & Sons.
- Ye, Z., Y. Jiang, H. Tai, and Z. Yuan (2014). The investigation of reduced graphene oxide/p3ht composite films for ammonia detection. *Integrated Ferroelectrics* 154(1), 73–81.
- Yi, C. (2013). *Graphene Based Flexible Gas Sensors*. Ph. D. thesis, Duke University.

- Yoo, S., X. Li, Y. Wu, W. Liu, X. Wang, and W. Yi (2014). Ammonia gas detection by tannic acid functionalized and reduced graphene oxide at room temperature. *Journal of Nanomaterials* 2014.
- Yoon, H. J., J. H. Yang, Z. Zhou, S. S. Yang, M. M.-C. Cheng, et al. (2011). Carbon dioxide gas sensor using a graphene sheet. *Sensors and Actuators B: Chemical* 157(1), 310–313.
- Yu, T., F. Wang, Y. Xu, L. Ma, X. Pi, and D. Yang (2016). Graphene coupled with silicon quantum dots for high-performance bulk-silicon-based schottky-junction photodetectors. *Advanced Materials* 28(24), 4912–4919.
- Yu, Y.-J., Y. Zhao, S. Ryu, L. E. Brus, K. S. Kim, and P. Kim (2009). Tuning the graphene work function by electric field effect. *Nano letters* 9(10), 3430–3434.
- Zhang, H., J. Feng, T. Fei, S. Liu, and T. Zhang (2014). SnO₂ nanoparticles-reduced graphene oxide nanocomposites for NO₂ sensing at low operating temperature. *Sensors and Actuators B: Chemical* 190, 472–478.
- Zhang, X., L. Wang, J. Xin, B. I. Yakobson, and F. Ding (2014). Role of hydrogen in graphene chemical vapor deposition growth on a copper surface. *Journal of the American Chemical Society* 136(8), 3040–3047.
- Zhang, Y., L. Gomez, F. N. Ishikawa, A. Madaria, K. Ryu, C. Wang, A. Badmaev, and C. Zhou (2010). Comparison of graphene growth on single-crystalline and polycrystalline Ni by chemical vapor deposition. *The Journal of Physical Chemistry Letters* 1(20), 3101–3107.
- Zhang, Y., Z. Li, P. Kim, L. Zhang, and C. Zhou (2011). Anisotropic hydrogen etching of chemical vapor deposited graphene. *ACS nano* 6(1), 126–132.
- Zhang, Y., Y.-W. Tan, H. L. Stormer, and P. Kim (2005). Experimental observation of the quantum hall effect and berry's phase in graphene. *Nature* 438(7065), 201–204.
- Zhang, Y., T.-T. Tang, C. Girit, Z. Hao, M. C. Martin, A. Zettl, M. F. Crommie, Y. R. Shen, and F. Wang (2009). Direct observation of a widely tunable bandgap in bilayer graphene. *Nature* 459(7248), 820–823.
- Zhou, L., F. Shen, X. Tian, D. Wang, T. Zhang, and W. Chen (2013). Stable Cu₂O nanocrystals grown on functionalized graphene sheets and room temperature H₂S gas sensing with ultrahigh sensitivity. *Nanoscale* 5(4), 1564–1569.
- Zhou, W., Z. Han, J. Wang, Y. Zhang, Z. Jin, X. Sun, Y. Zhang, C. Yan, and Y. Li (2006). Copper catalyzing growth of single-walled carbon nanotubes on substrates. *Nano letters* 6(12), 2987–2990.
- Zhou, Y., Y. Jiang, G. Xie, M. Wu, and H. Tai (2014). Gas sensors for CO₂ detection based on rGO-PEI films at room temperature. *Chinese Science Bulletin* 59(17), 1999–2005.

VITA

Date and Place of Birth: 13.01.1986, İzmir-TURKEY

EDUCATION

2011 - 2017 Doctor of Philosophy in Material Science and Engineering

Graduate School of Engineering and Sciences, İzmir Institute of Technology,
İzmir -Turkey

Thesis Title: FUNCTIONALIZED CVD GROWN GRAPHENE
FOR GAS SENSING APPLICATIONS

Supervisor: Assoc. Prof. Dr. Cem Çelebi

2008 - 2011 Master of Science in Physics

Graduate School of Engineering and Sciences, İzmir Institute of Technology
İzmir -Turkey

Thesis Title: CHARACTERIZATION OF MODIFIED ITO ANODE SURFACES
WITH 4-[(3-METHYLPHENYL)(PHENYL)AMINO]BENZOIC ACID FOR
OLED APPLICATIONS

Supervisor: Assoc. Prof. Dr. Salih Okur

2003 - 2008 Bachelor of Physics

Department of Physics, Faculty of Science, İzmir Institute of Technology
İzmir - Turkey

PUBLICATIONS

Yağmircukardeş N., Aydın H., Can M., Yanılmaz A., Mermer Ö., Okur S. and Selamet Y. 2016: "Effect of Aromatic SAMs Molecules on Graphene/Silicon Schottky junction "ECS Journal of Solid State Science and Technology Volume: 5 Issue 7, 2016, Pp. 69-73.

DOI: <http://doi.org/10.1149/2.0141607jss>

Yağmircukardeş N., Bayram A., Aydın H. and Çelebi C.: "Effect of Anisotropic Etching of CVD Grown Graphene on Ammonia Sensing" Sensors and Actuators B (submitted).